Università degli Studi di Ferrara

ISTITUTO ITALIANO DI TECNOLOGIA

DOCTORAL COURSE IN

TRANSLATIONAL NEUROSCIENCE AND

NEUROTECHNOLOGIES

CYCLE XXXII

COORDINATOR Prof. Luciano Fadiga

Improving the Quality of ECoG Recordings: A Translational Study from Rats to Humans

Scientific/Disciplinary Sector (SDS) BIO/09

Candidate

Dott. Zucchini Elena

Supervisor

Prof. Fadiga Luciano

Year 2016/2019

Table of Content

Abstract

Neural interfaces represent a technological bridge enabling bidirectional communication between the brain and the outside world. To untangle the complexity of neural networks and eventually restore them, near fool-proof devices are required. In the past decades, close collaboration between biomedical engineers and neuroscientists has led to essential advances in both the basic and clinical neurosciences. Nevertheless, due to the multiple natures of recording failures, neural probes have not reached their full potential as reading and rewriting neural tools.

Following the latest trends in neurotechnology, this study tested a novel class of ultra-conformable micro-electrocorticographic (μECoG) arrays on a rat model to find the key factors for obtaining high-quality neural interfaces. Long-term neural recordings (up to 12 weeks) were obtained, taking advantage of ultra-thin substrates (8-μm thick polyimide, PI) and highly stable electrode materials (platinum, iridium oxide, PEDOT/PSS [poly(3,4-ethylenedioxythiophene) polystyrene sulfonate], and glassy carbon). The conformability of PI reduced the invasiveness of the implants, and miniaturization of the recording sites enabled the investigation of spatially resolved high-frequency signals (multi-unit activity). Moreover, as a possible strategy for avoiding redundancy of spikes detected with closely spaced electrodes, a reference electrode intermingled with the recording sites was successfully used in differential recording mode, ultimately improving the spatial resolution of the signal. By combining ultra-thin device miniaturization with a recording frequency band of 1 kHz and beyond, crosstalk emerged as a setback to the desired spatial selectivity. Therefore, the degree of this undesired effect was investigated *in vivo* and *in vitro* to facilitate the future design of microelectrodes with minimal crosstalk levels.

Finally, the ultra-conformable μECoG array was tested on one human subject undergoing awake neurosurgery to investigate the neural correlates of speech processing recorded from the frontal cortical region for speech production.

Introduction

Understanding the human brain is one of the most compelling and at the same time complex challenges of research. More than two centuries ago, Luigi Galvani's experiments revealed the electrical nature of signaling in the nervous system [1]; since then, several generations of neurophysiologists have devoted their scientific research to this goal. The support of neurotechnology development has enabled outstanding breakthroughs in both basic and clinical neuroscience (Figure 1) [2]. Taking advantage of neural interfaces as therapeutic tools has allowed great feedback in the treatment of several neurological disorders (e.g., epilepsy, Parkinson's disease, or essential tremor) [3–7]. Likewise, their implementation in brain–computer interface (BCI) applications renders the rehabilitation of severely motor-impaired patients possible [8–11]. Even so, the sophistication of brain functions leaves room for further investigations required to shed light on still-unsolved questions about neural processes as well as to continue improving the efficiency of neural devices.

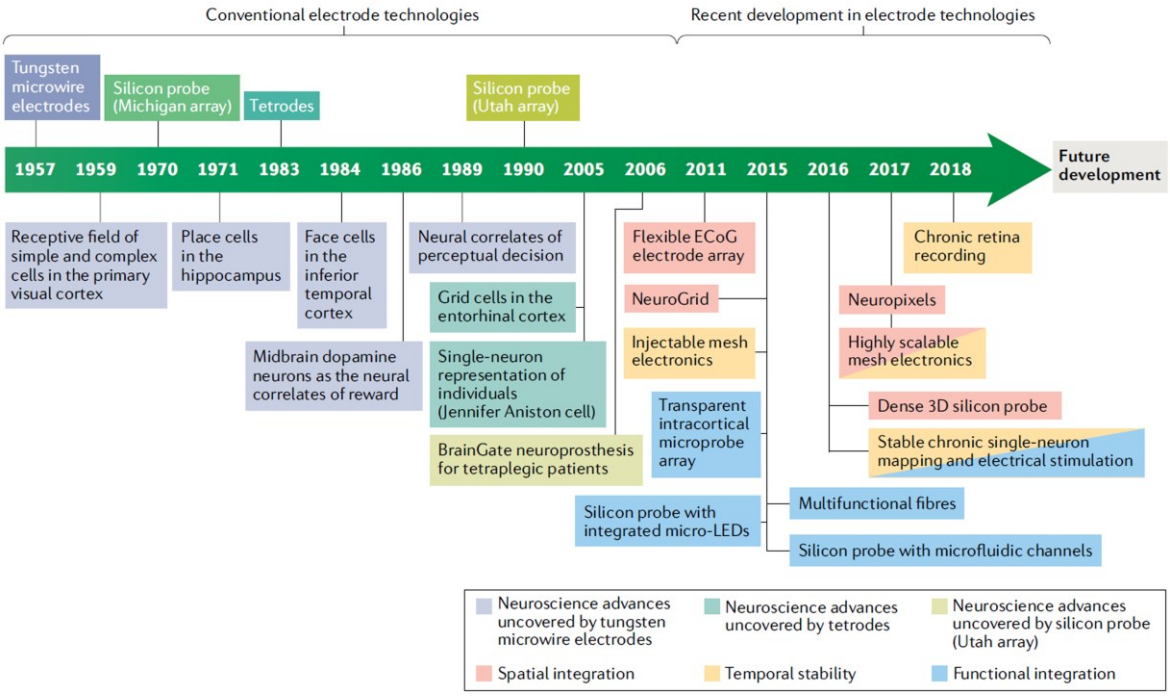

Figure 1 On the left, conventional electrode technologies for *in vivo* neural recordings are shown above the timeline; key neuroscience discoveries enabled by these technologies are shown below the timeline with the same color coding as each corresponding electrode technology. On the right, recent development of neural recording electrode technologies is summarized in three categories for neural probes with high spatial integration, long-term temporal stability and multifunctional integration in corresponding colors. (From Hong G. and Lieber C. M., 2019)

According to a simplified version of how the brain works, the central nervous system is in charge of collecting and processing, in the context of past experience, the sensory inputs from the outside world, and closing the loop through the definition of appropriate motor outputs. This circuitry relies on the cooperation of billions of neurons connected by quadrillions of synapses, reaching a number that exceeds the amount of stars in the Milky Way galaxy [12]. Moreover, neurons represent just the ~50% of the brain cell population. Glial cells, which include astrocytes, oligodendrocytes, and microglia, constitute the remaining part sustaining the nervous tissue; their specific role at synaptic level, and more generally in brain functions, remains an open field of investigation [13, 14].

Electrical and chemical signals represent the main forms of communication among nervous cells. The propagation of action potentials (i.e., spikes) along neuronal membranes is sustained by voltage-gated ion channels (e.g., sodium, potassium, and calcium channels). Such electrical signals are transmitted from the pre-synaptic neuron, down the length of the axon, to the synapse. Subsequently, neurotransmitters are released in the synaptic cleft to diffuse towards the downstream neuron and bind receptors (i.e., ligand-gated ion channels) on its membrane. Depending on the specific neurotransmitter–receptor combination, the translation of the electrical signal into a chemical signal (i.e., signal transduction) can exert either excitatory or inhibitory functions on the post-synaptic neuron. Finally, this targeted neuron will then repeat the process, propagating or modifying the initial input.

Zooming out and thus looking at a larger portion of neural tissue, ensembles of firing neurons give rise, in the extracellular medium, to the so-called local field potentials (LFPs). According to the distribution of current flow in a volume conductor, transmembrane currents arising from excitable cells within a volume of brain tissue superimpose at a given point of the medium and generate a potential with respect to a reference location. Multiple sources contribute to the extracellular field, and thus, waveform components of the LFPs (e.g., amplitude and frequency) depend on their proportional contributions and on tissue properties. Specifically, the magnitude and sign of the individual current sources, their temporal coordination (synchrony), and the architectural organization of the network (e.g., the shape and dimensions of the implicated cells) play pivotal roles in shaping the LFP. Moreover, considering that the voltage amplitude decreases with the distance between the source and the

recording site, the recording electrode location has also an influence on the measured electrical potential [15].

The most common means of recording brain activity involves the use of electrodes, which also allow stimulation of the nervous cells. Therefore, bidirectional electrical communication between neurons and neural devices (and thus with the external environment) is enabled. The impedance—simplified as the electrical resistance to alternating current flow—of the electrode–tissue interface determines the ability to record neurophysiological signals, and can be represented by equivalent circuit models (Figure 2).

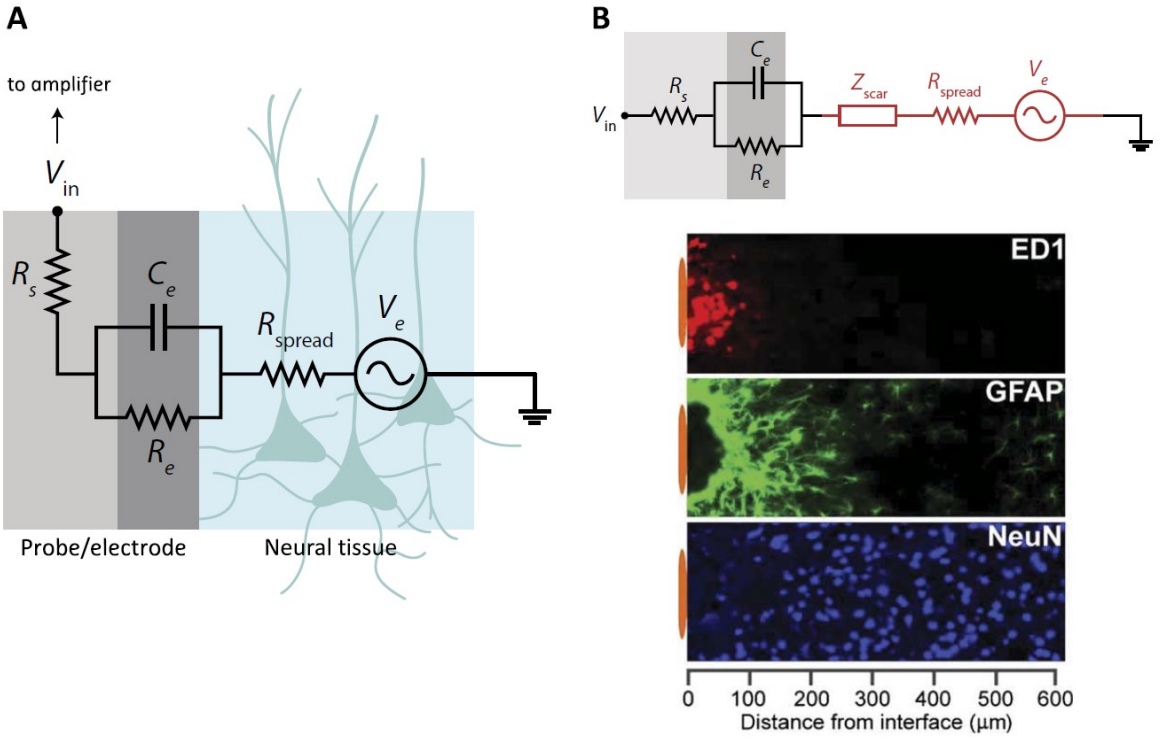

Figure 2 (A) Equivalent circuit of electrode–tissue interface in neural recordings: neurons act as a voltage source (V_e) and the use of an amplifier is considered. R_{spread} is the resistance of the electrolyte; C_e is the capacitance of the electrode–electrolyte interface; R_e is the leakage resistance that models the flow of the charge carriers crossing the electrical double layer; R_s is the resistance of the electrode. (B) Influence of neuroinflammatory reaction (astroglial scar) on local electrical impedance. The neuroinflammatory response adversely affects the signal from the neurons and introduces a scar impedance (Z_{scar}) due to the formation of a dense layer of inflammatory cells (ED1), astrocytes (GFAP), and a distancing of neurons (NeuN) from the recording site. (Adapted from Rivnay J. *et al.*, 2017; fluorescence image is reproduced, in part, from Biran R. *et al.*, 2005)

Currents generated by firing neurons embedded in the neural tissue can be understood as a low-impedance voltage source (V_e), and depending on the geometry of the recording site, the model should include a given resistance of the extracellular medium (R_{spread}). Common representations of electrodes involve the

presence of the resistance (R_e) and the capacitance (C_e) of the double layer interface (i.e., electrode–tissue interface), and finally, of the resistance of the electrode (R_s). Such resistance of the interconnections that lead to the recording system (R_s) should not be underestimated when dealing with organic conductors, but on the contrary, can be considered negligible when using metallic components [16]. Therefore, the effective impedance of the electrode consists of the resistance of the electrolyte (R_{spread}), the resistance and capacitance of the electrode–electrolyte interface (R_e and C_e, respectively), and the resistance of the electrode per se (R_s). When all the other variables are kept constant, a lower electrode impedance translates into an easier readout of the voltage source (i.e., neural activity).

Two important aspects of electrical interfaces need to be taken into account when aiming to perform long-term neural recordings. First, the effects of foreign body reaction such as astroglial scar and neural cell death/migration determine: i) the introduction of additional impedance (Z_{scar} in Figure 2B) due to the scar formation, and ii) the reduction in magnitude of the measured voltage potential [17]. Second, the frequency-dependent behavior of electrode impedance provides that, at low frequencies, the impedance is dominated by the R_{spread} and R_e components, while at high frequencies, C_e bypasses the effect of R_e, making R_{spread} the prevailing component of the impedance [18, 19].

Accordingly, electrical recordings enable the detection of neural oscillations in a broad range of frequencies, which can be mainly categorized in two types of voltage signals: i) slow varying potentials (i.e., LFPs, <300 Hz) and ii) fast varying potentials (i.e., spikes, >250 Hz). To selectively separate signals in lower- and higher-frequency bands, analogue and digital filters can be applied to the raw data (Figure 3). Moreover, for fast-varying potentials, each putative neuron can be discriminated as a single-unit activity based on specific components such as waveform shape and amplitude of the recorded action potentials. LFPs play a critical role in coordinating the activity of different regions of the brain and synchronizing the activity of individual neurons with that of a neural network. Individual neurons, on the other hand, represent the structural and functional units of the nervous system, with their spatiotemporally resolved activities holding the key to understanding the inner workings of the brain [15, 20]. An ideal neural interface would be one providing as much valuable information as possible, spanning single neuron activity to its complex network of connections, while remaining non-invasive. Unfortunately, if low

invasiveness is sought by placing the recording site farther away from the signal source, as already mentioned, the measured signal becomes less informative about the events occurring in the brain tissue. Consequently, the application of interest should guide the choice between different neural interfacing modalities.

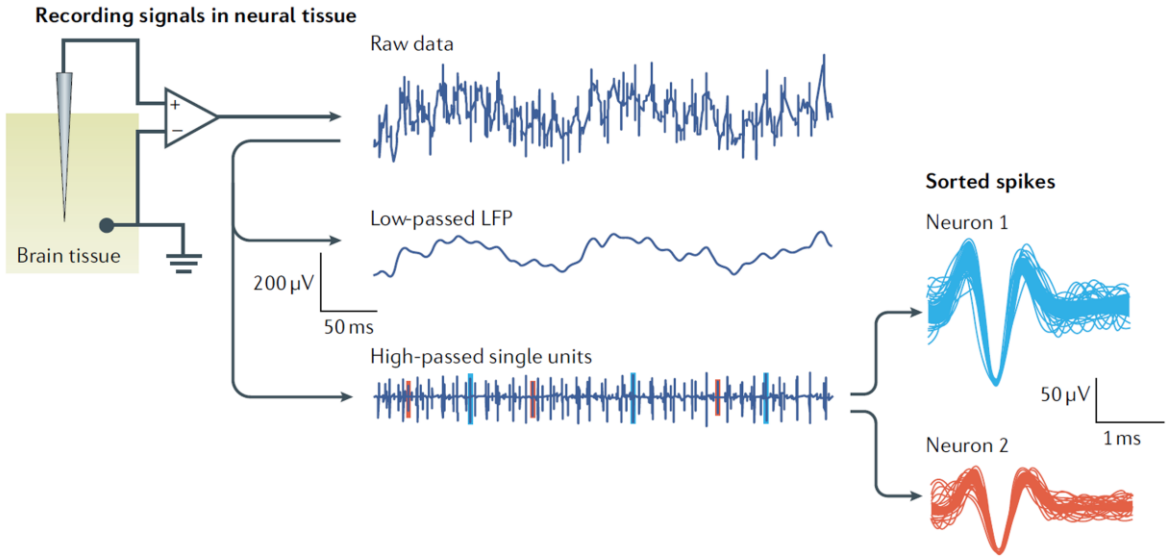

Figure 3 Schematic picture illustrating the basic principles of measuring bioelectrical signals by recording electrodes in neural tissue (left), with representative raw, low-pass and high-pass filtered neural recording traces (middle) and sorted spikes (right) measured by an electrode. (Adapted from Hong G. and Lieber C. M., 2019)

1. Neural Interfacing Modalities

Currently, brain activity readouts can rely on several different methodologies, which essentially differ in their degree of invasiveness and spatial resolution (Figure 4). Most invasive devices will require implanting either above or into the brain cortex, enabling progressive gains in resolution but concurrently causing various setbacks in terms of tissue reaction [2, 16, 21, 22].

Starting from the least invasive implementation of electrodes, electroencephalography (EEG) probes electrical potential variations by using large electrodes placed over the scalp. Neural oscillations are collected from large regions of the brain, making it an appropriate method for investigating communication within the brain and rhythmic signals arising from specific stimuli or states of consciousness. Unfortunately, EEG signals are affected by many drawbacks: the frequency bandwidth of the recorded signal is limited due to skin/skull attenuation and filtering (high-frequency oscillations are lost), and it is difficult to avoid high sensitivity to motion and environmental artefacts. One key challenge for this technique is the need to lower, as much as possible, the electrical impedance between the skin and the recording electrode. Nevertheless, being easy to set-up and completely non-invasive, EEG is a tool routinely used in clinical settings (e.g., diagnosis of epileptic syndromes) and in BCI systems for rehabilitation [23, 24].

When aiming to investigate higher levels of cortical processing, it is necessary to resort to more invasive approaches. As already mentioned, one great advantage of neural interfaces placed directly in contact with the brain, such as electrocorticographic (ECoG) arrays and intracortical devices, is the improved temporal resolution (skin/skull filtering is avoided). When using these techniques, aside from recording the EEG canonical frequency bands (delta, 1–4 Hz; theta, 4–8 Hz; alpha, 8–12 Hz; beta, 12–30 Hz; gamma, 30–60 Hz), the detection of high gamma activity (70–150 Hz) becomes possible. Such oscillations have been linked to high-level cognitive functions such as memory, attention, volitional movement, and conscious perception, leading researchers to correlate high gamma activity to higher levels of cortical processing [25, 26]. Therefore, the invasiveness of the required implanting procedure is balanced by an evident gain in the quality of the recorded information.

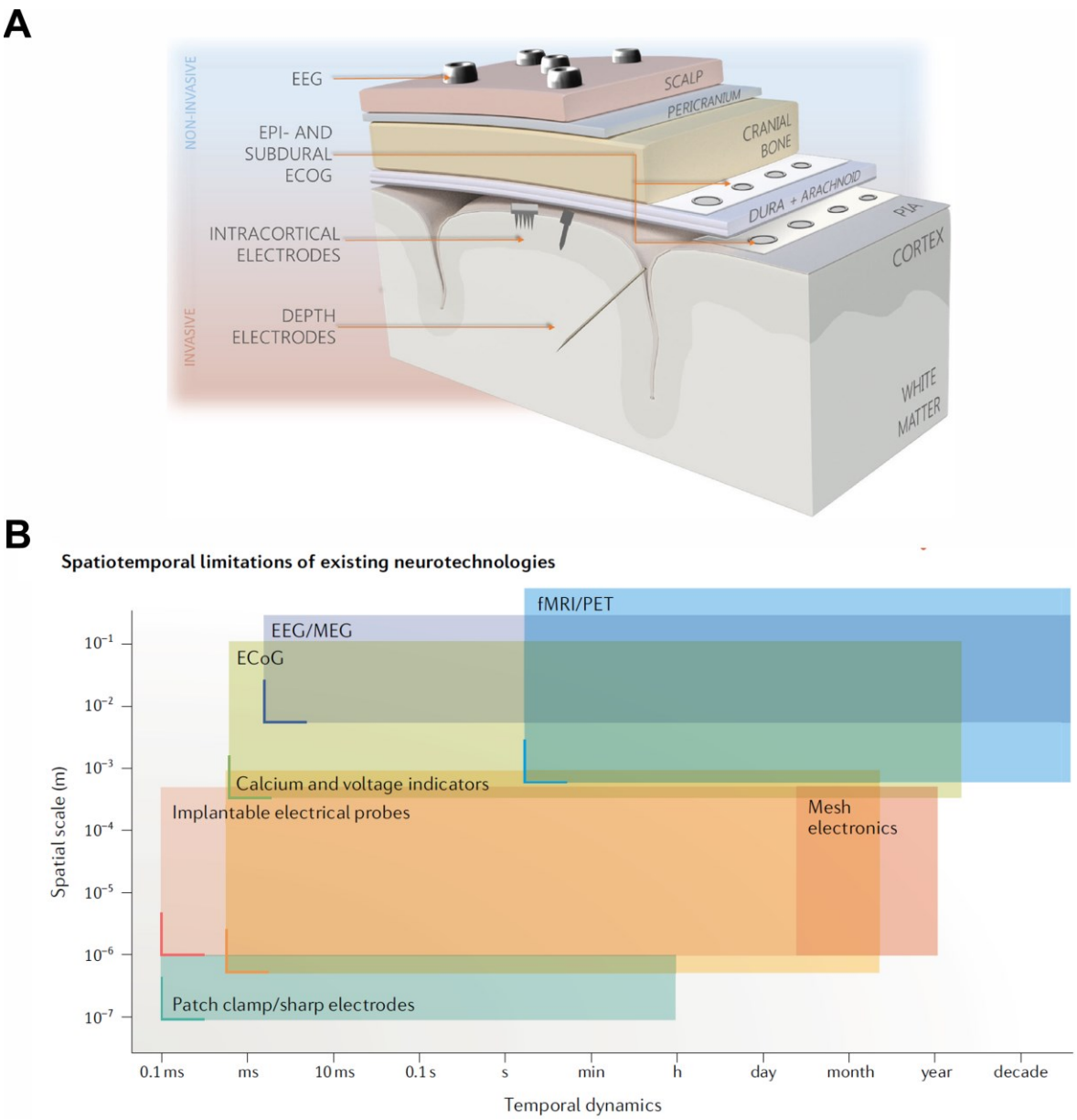

Figure 4 (A) Types of brain interfacing modalities and the respective electrode location in the reference to the brain. Less invasive systems (from red to blue background) provide recordings of increasingly lower resolution in comparison to their invasive counterparts. (Adapted from Szostak K. et al., 2017). (B) The essential physical constraints (in particular, the spatiotemporal dilemma) of various existing neurotechnologies. ECoG, electrocorticography; EEG, electroencephalography; fMRI, functional MRI; LFP, local field potential; MEG, magnetoencephalography ; PET, positron emission tomography. (Adapted from Hong G. and Lieber C. M., 2019)

Further, to achieve the resolution required for detecting single neuron activity, close interaction with the neural tissue is also necessary. Enabling such a level of recording resolution can lead to even better understanding of the brain wiring and its link to perception, motion, and memory. In recent years, advances in neurotechnology have extended the possibility of recording single- and multi-unit activity (defined in the kHz frequency range) to ECoG, which can be considered a

semi-invasive technique [27, 28]. ECoG recordings are performed by placing the electrode array over the cerebral cortex (either epidurally or subdurally), avoiding the breaching of the blood–brain barrier. Using ultra-conformable arrays with submillimeter-spaced electrodes (i.e., μECoG) improves not only the signal quality (recordings in the kHz range are enabled) but also the biocompatibility of the implant [27, 29]. Before such technological achievements, electrical measurements of spiking activity were thought to be a prerogative of intracortical recordings, which imply the insertion of electrodes into the neural tissue and thus their nearby placement to neurons. Intuitively, this latter approach produces the most efficient results in terms of spatiotemporal resolution, but is also the most invasive approach. Intracortical devices, especially when aiming to perform long-term recordings, encounter all the complications due to the foreign body response (FBR) triggered by insertion of the probe into the brain tissue. Moreover, contrary to ECoG, intracortical arrays are not appropriate for large-scale mapping of brain activity. In such a scenario, ultra-conformable μECoG arrays can be considered the best compromise between invasiveness and spatiotemporal resolution.

2. Main Causes of Recording Failure

The stability and quality of invasive chronic recordings are undermined by several causes due to the close interaction between neural interfaces and neural tissue. Recording failure of epicortical and intracortical arrays can be broadly classified into those of technological origin and those of biological origin (Figure 5). The first category includes: i) direct mechanical damage of the device and interconnections, ii) corrosion/delamination of electrical contacts, and iii) degradation of passivation layers and insulating coatings. Differently, biological failure can be ascribed to the neuroinflammatory response the brain mounts against chronically implanted devices [21, 30]. As a consequence of both types of failure, the tissue–electrode interface encounters an increase in electrical impedance that undermines recording quality and the operative lifetime of the device [16]. While the engineering-related setbacks affect epicortical and intracortical arrays in the same manner, the biological failure mechanisms have greater impact on the intracortical probes.

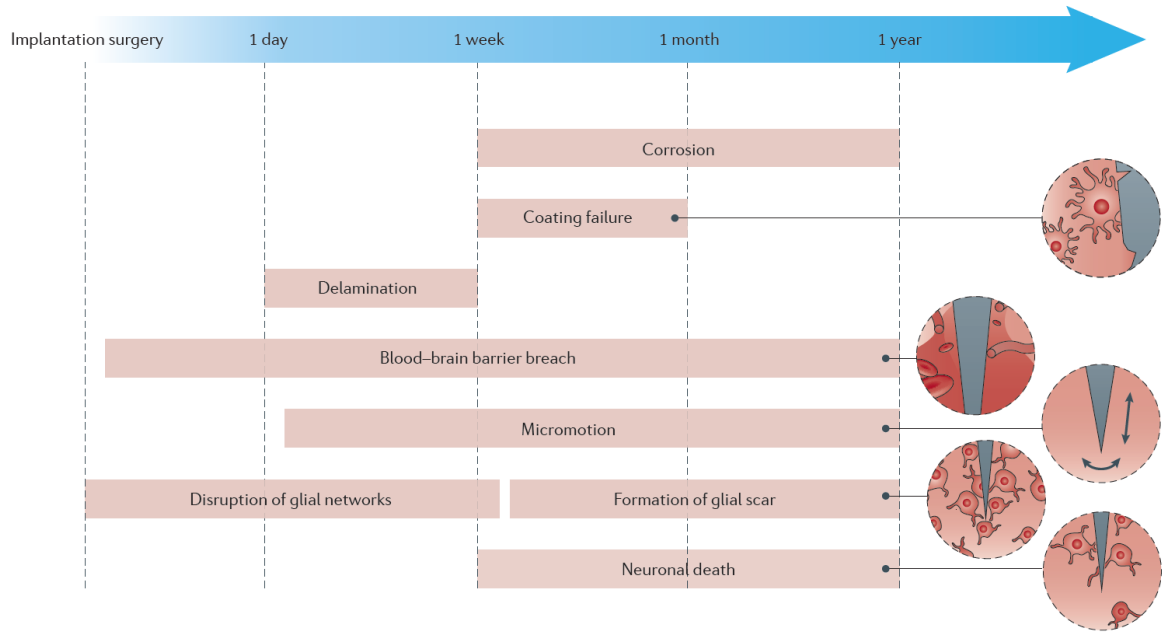

Figure 5 Recording failure modalities classified into those related to device design and those related to FBR. Design failure mechanisms include: mechanical failure of interconnects, degradation and cracking of the insulation, electrode corrosion, and delamination of probe layers. Biological failure mechanisms include: initial tissue damage during insertion, breach of the blood–brain barrier, elastic mismatch and tissue micromotion, disruption of glial networks, formation of a glial scar, and neuronal death. (From Chen R. *et al.*, 2017)

2.1 Technological Failures

Performance decline of neural recordings can frequently be attributed to deterioration of the physical device due to operation in the biological environment. Concerning the use of intracortical arrays, several studies have reported mechanical damage of the device during or following insertion [31–34]. Thus, as a first step to obtaining reliable recordings, enhancement of the mechanical stability of the entire interfacing systems (from the electrode per se to the interconnects) should be pursued.

Focusing on the electrical contacts directly interfacing the brain, both epicortical and intracortical devices commonly experience electrode cracking and delamination. These side effects are mainly caused by poor adhesion, mechanical defects, or unintended mechanical stresses [30]. Additionally, as another primary cause of recording impairment, corrosion of the electrode material frequently occurs. Consequently, two major negative effects are determined: i) the conductive properties of the electrode are corrupted by increased resistance (R_s in Figure 2) and/or decreased capacitance of the electrode–tissue interface (C_e in Figure 2), and ii) toxic species are generated and released in the neural tissue. The latter effect, in turn, can be linked to cell death and increased immune response. The rate of corrosion likely depends on the specific environment and electrode material. Some metals (e.g., tungsten and stainless steel) readily corrode in ionic media. Therefore, the use of other metals, alloys, and organic conductors is preferable [30, 35, 36].

Insulating layers incorporated into probes, in a similar manner to electrode sites, may degrade over time and lead to the exposure of metallic interconnections. Chemical and electrochemical reactions, film degradation, and mechanical stress play a role in this degradation process, which has the unintended consequence of introducing parasitic current pathways between the tissue and the recording system, as well as crosstalk between recording sites. Significant degradation of an electrode insulating layer could thus reduce the capability for detecting local signals [30, 37].

2.2 Biological Failures

With the term neuroinflammatory response, one refers to the combination of chemical and cellular pathways the immune system of the nervous system triggers to metabolize or isolate a foreign body (i.e., the implanted device). When compared to technological failures, biological reactions to implanted devices can be considered the primary barrier preventing neural interfaces from reaching their full potential [30]. Therefore, together with technological improvements towards more robust probes, better understanding of the foreign body reaction as well as the development of smart strategies to reduce its impact are of critical importance.

Several attempts to correlate individual components of the neuroinflammatory response with specific effects on recording quality have been made, but a satisfactory explanation has not been reached. The most likely circumstances are represented by a simultaneous interplay of multiple factors (Figure 6).

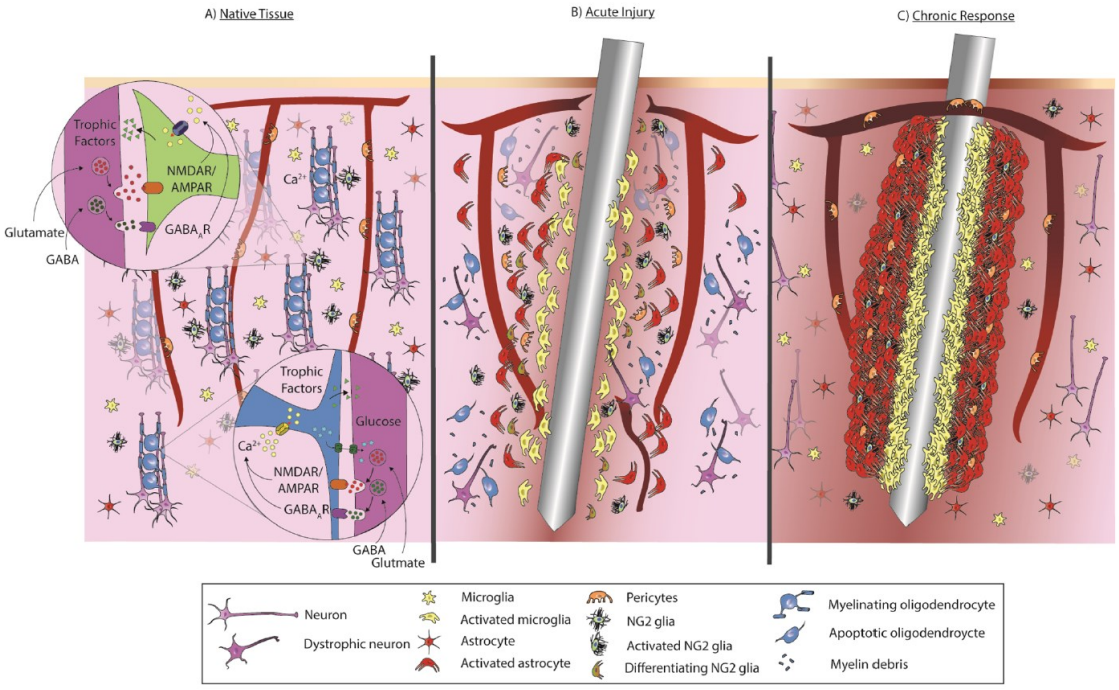

Figure 6 Visualization of FBR to implantable devices in the brain. (A) Cellular components in healthy brain tissue. (B) Acute injury after device insertion. Disrupted blood vessels leak inflammatory factors into the parenchyma. Microglia, astrocytes, and NG2 glia become activated and migrate toward the surface of the device. NG2 glia differentiate into scar-forming astrocytes around the implant. (C) Chronic immune response to implanted devices. Glial cells form a chemical and mechanical barrier around the device, preventing the transmission of ions, charged solutes, and neurochemical signals. (From Wellman S. M. and Kozai T. D. Y., 2017)

When using intracortical electrodes, the highly vascularized nature of the nervous tissue makes the breaching of the blood–brain barrier nearly unavoidable. Indeed, the first immediate consequence of implant—also referred to as acute response—are vascular and cellular injury. Several cascades and processes promoting wound closure and healing are initiated, including the recruitment of inflammatory cells to the injury site [38, 39]. Due to brain pulsation with respect to the probe, motion-induced damage at the tissue–electrode interface are perpetuated, meaning that the aforementioned events may occur repeatedly after the initial insertion trauma [40–42]. Consequently, persistent inflammation at the biotic–abiotic interface is established, involving the activation of resident microglia and the recruitment of blood-borne macrophages [17, 43–45]. Such actors are responsible for many processes related to the tissue reaction (e.g., interaction with pathogens, phagocytosis of damaged/dead cells, and clearing of residual cell debris) [46, 47]. Specifically, after attaching to the device surface, they play a critical role in producing proinflammatory and cytotoxic soluble factors [48–51]. As already mentioned, this effect is one of the main causes of electrode material corrosion.

Further key players of the neuroinflammatory response are astrocytes, the principal microenvironment regulators of healthy brain tissue. However, following injury, astrocytes assume a hypertrophic state (the number and size of their cellular processes increase) and surround the inflammatory core. Subsequently, dense astrocyte encapsulation envelops the probe, forming a so-called glial scar (i.e., astrogliosis) [21, 30, 44]. On one hand, some studies state that such a scar-like layer may have beneficial effects by acting as a mechanical shield against micromotions and limiting the amount of macrophage-secreted factors [52–55]. On the other hand, astrogliosis likely increases the impedance of the tissue–electrode interface, limiting the electrode recording capability [56, 57].

Lastly, several studies have reported neuronal loss and overall decrease in neuronal density during chronic response scenarios [17, 45, 58, 59]. Reactions occurring in the tissue surrounding the probe may indeed compromise the environment, limiting the promotion of neuronal health and function.

Generally, epicortical implants do not disrupt the blood–brain barrier and cause minimal damage to the cortex when compared to intracortical recordings. Nevertheless, the stereotypical FBR can also be observed when using ECoG. Macrophages and glial cells are activated at the electrode–tissue interface, electrodes are encapsulated in collagenous tissue, and cortex depression is induced

by the presence of stiff arrays [60]. The primary causes of these reactions are still unclear, but it has been shown that the mechanical mismatch between nervous tissue and electrodes plays a critical role in triggering the foreign body reaction to implanted epicortical arrays [61].

To date, the extremely complex picture behind recording failures has prevented the possibility of finding univocal correlations between recording quality and the phases of neuroinflammatory response [30]. Thus, the challenging goal of obtaining consistent, high-quality, long-term neural recordings should involve multiple approaches.

3. How to Improve Neural Interfaces

Electrical recordings, as well as other modalities for detecting brain activity (e.g., optical recordings), can be improved through the combination of multiple materials and device engineering. With the ultimate goal of human recordings, presented here is a focus on promising approaches that could be directly implemented in neural interfaces for human applications.

The most efficient strategies for achieving high-quality recordings appear to be those addressing the mechanical aspects of the neural interfaces. Indeed, when the stiffness of the implanted material is highly different from that of the neural tissue, chronic implants exert constant forces on the surrounding brain tissue, leading to several unfavorable consequences. For example, relative shear motion at the interface changes the relative position between the recording electrodes and recorded neurons. Moreover, the repeated chronic damage to the much softer surrounding brain tissue triggers the responses of the foreign body reaction, including neural death, glial scar formation, and perturbation of the natural distribution of cells within the central nervous system. Such a scenario clearly prevents the study of individual neuron activity and their role within neural circuits. Therefore, better matching of the mechanical properties of both intracortical and epicortical arrays with that of the neural tissue would prevent disturbing of the natural brain environment, enabling consistent recordings even in the long-term [2, 16, 30].

Two physical quantities, Young's modulus and bending stiffness, are typically used to describe the rigidity, or resistance to bending or deformation, characterizing the implant. Young's modulus is defined as the intrinsic material property that determines the ability of a material to resist change in length under tensile or compressive forces. Although Young's modulus defines the intrinsic mechanical properties of a material, the bending stiffness—defined as the capacity of structural members to resist bending—of a specific neural probe plays a more direct role in determining the degree of mechanical mismatch and thereby the evoked chronic immune response in the neural tissue [2, 21, 62].

Progress in probe mechanical properties has been made by taking advantage of polymers such as parylene-C, polyimide (PI), or SU-8, with even greater results being achieved with elastomers or hydrogel coatings. However, despite these technological improvements, the widely used electrode materials for neural

interfaces (e.g., silicon, carbon, and metals) are on average 8–9 orders of magnitude more rigid than brain tissue. Accordingly, conventional and more recent neural probes (e.g., Michigan and “e-dura” probes) remain several orders of magnitude stiffer than brain tissue. To date, only mesh electronic devices, which take advantage of the dependence of bending stiffness on probe thickness, have managed to reach values comparable to those of neural tissue (Figure 7).

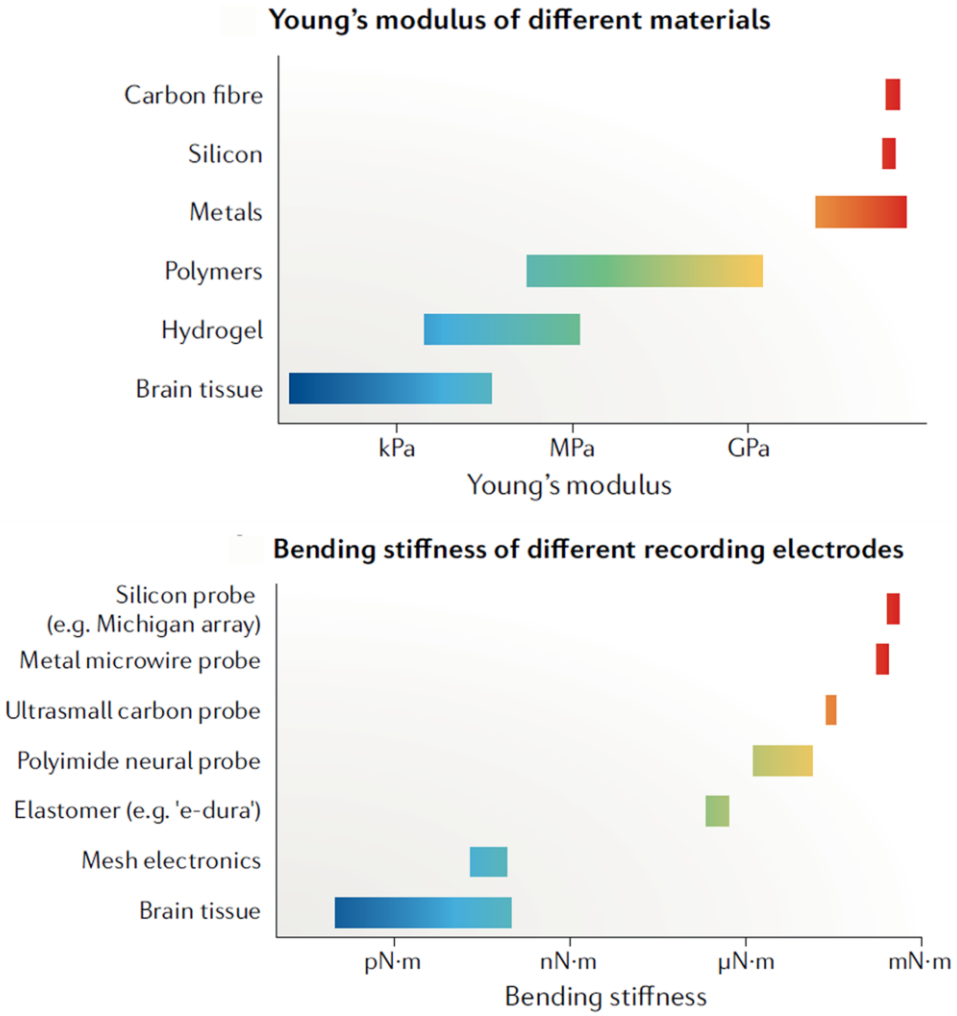

Figure 7 (A) Young’s moduli of different conventional and recent materials are compared to the neural tissue value. (B) Effective bending stiffness values of conventional and emergent probes are reported along with that of 20–100-μm thick slices of brain tissue. (Adapted from Hong G. and Lieber C. M., 2019)

A second approach to addressing the mechanical mismatch problem, and in turn, to “trick” the immune system, relies on probe miniaturization. This strategy suggests that stiffer materials can be used as long as the dimensions of the array are small enough to match the subcellular scale (1–10 μm) [63]. The idea behind reducing electrode size is to make intracortical devices invisible to the brain, avoiding the foreign body reaction. Moreover, reducing the surface area results in reduced

inflammatory cells and proinflammatory soluble factors at the biotic–abiotic interface [64]. Concerning epicortical arrays, electrode miniaturization leads to two main positive effects: i) enables the detection of single-unit activity from the surface of the cortex [27, 28], and (ii) the reduced dimensions of electrode grids allow less invasive implant procedures. In this manner, high-density μECoG arrays can be seen as the most appealing recording modality able to provide excellent spatiotemporal resolution at the lowest cost in terms of invasiveness.

A direct consequence of electrode size reduction that should not be underestimated is the increase in electrode impedance [19]. Large electrodes are characterized by low electrolyte resistance (R_{spread} in Figure 2 and 8) and high capacitance of the double layer interface (C_e in Figure 2 and 8). The inverse behavior of small electrodes, together with the desired miniaturization, determine the need to find smart ways of maximizing the C_e while maintaining the small electrode geometries. This improvement aims to be the key enabler of the detection of action potentials of individual neurons with high signal-to-noise (SNR) ratios. Equivalently, to electrically stimulate small portions of neural tissue, microelectrodes with high charge injection limits and low electrode impedance are required. For these purposes, several strategies for increasing the effective surface area and thus decrease the impedance of microelectrodes have been proposed (Figure 8).

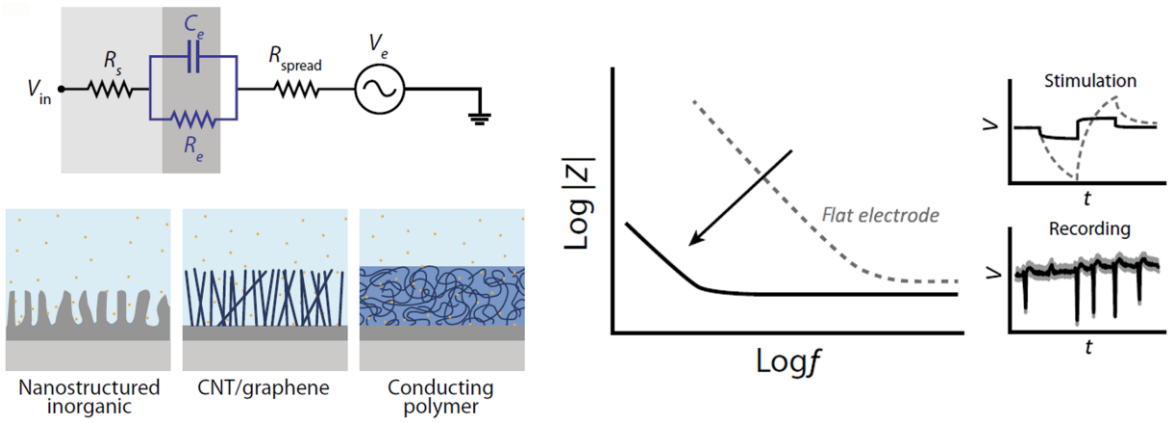

Figure 8 Influence of enhanced electrode coatings on improving the impedance of the electrode itself. Nanostructuring of traditional electrode materials, use of carbon nanotubes [CNTs]/graphene, or conducting polymers (CPs) allow for increased ion interaction with the electrode and a marked drop in impedance. On the right, impedance comparison and resulting stimulation profile for a given biphasic current pulse and recording quality are shown for a flat electrode (grey, dotted) and for an electrode with an enhancing coating (black line; e.g., CPs). (Adapted from Rivnay J. et al., 2017)

Flat electrodes, such as those based on platinum (Pt), iridium, stainless steel, and iridium oxide (IrOx), have been engineered to obtain porous and nanostructured

variants by modifying the deposition processes or performing post-processing steps such as electrodeposition or etching. A similar method has been adopted for carbon nanostructures (e.g., carbon nanotubes [CNTs] and graphene [65–69]), as well as their composites, with similar results [70]. With the same aim, extremely good results have been obtained with conductive polymers (CPs), such as poly(3,4-ethylenedioxythiophene) (PEDOT). These materials are widely used because of their versatility in deposition/patterning, hygroscopic nature, and excellent mixed conduction properties (e.g., ionic and electronic). When compared to uncoated microelectrodes, CP deposition exhibits lower impedance and higher charge capacity. Their electrical conductivity can be additionally boosted through combination with nanocomposites (e.g., CNTs [71, 72]), and they can be easily functionalized via physical entrapment and covalent crosslinking with biomolecules and cells [30, 73–75]. Among the improvements stemming from the implementation of CPs, the main reason for their popularity can be ascribed to their biocompatibility and capacity for providing long-term recordings with greater SNR ratio.

To summarize, several approaches can be undertaken to improve neural probes and in turn neural recordings. Clearly, the way for developing a superior neural interface does not come follow just one route, but the greatest gains arise from the combination of multiple approaches.

Aim and Approach

Traditional ECoG grids have poor spatial resolution (from 1 cm to 4 mm), and their long-term recording stability is mainly limited by two factors. The FBR triggered by device implantation leads to electrode encapsulation and eventually to insulation from the neurons [43, 76]. In addition, delamination and corrosion of the electrode material can lower the quality of the acquired signal or even cause recording failure [77, 78].

With the aim of improving the quality of the neural signal recorded in humans for speech decoding and tumor mapping purposes, and to achieve better long-term stability and higher spatial resolution, I tested a novel class of ultra-conformable µECoG arrays with diverse electrode materials and geometries [29, 79].

First, to assess the array features, I validated *in vivo* the device performances in rat models. The conformability of the µECoG arrays was evaluated via histology, and recording capabilities were explored using electrophysiological techniques in acute and chronic scenarios. Specifically, to connect multi-unit neuron activity and large-scale cortical mapping, high-frequency signals (>200 Hz) recorded from the surface of the cortex were investigated in terms of quality and spatial selectivity. Moreover, to monitor the reactions occurring at the electrode–tissue interface, I collected *in vivo* impedances of chronically implanted electrodes for up to 12 weeks.

When combining ultra-thin device miniaturization with widening of the recording frequency band up to 1 kHz and beyond (to record spikes), crosstalk represents a possible setback to the desired spatial selectivity. Thus, I performed *in vivo* and *in vitro* evaluation of the degree of crosstalk between the closely routed tracks of the µECoG.

Ultimately, with focus on speech-related neural responses, I tested the ultra-conformable MuSA (multi-species array [29]) on one human subject undergoing awake neurosurgery for tumor resection.

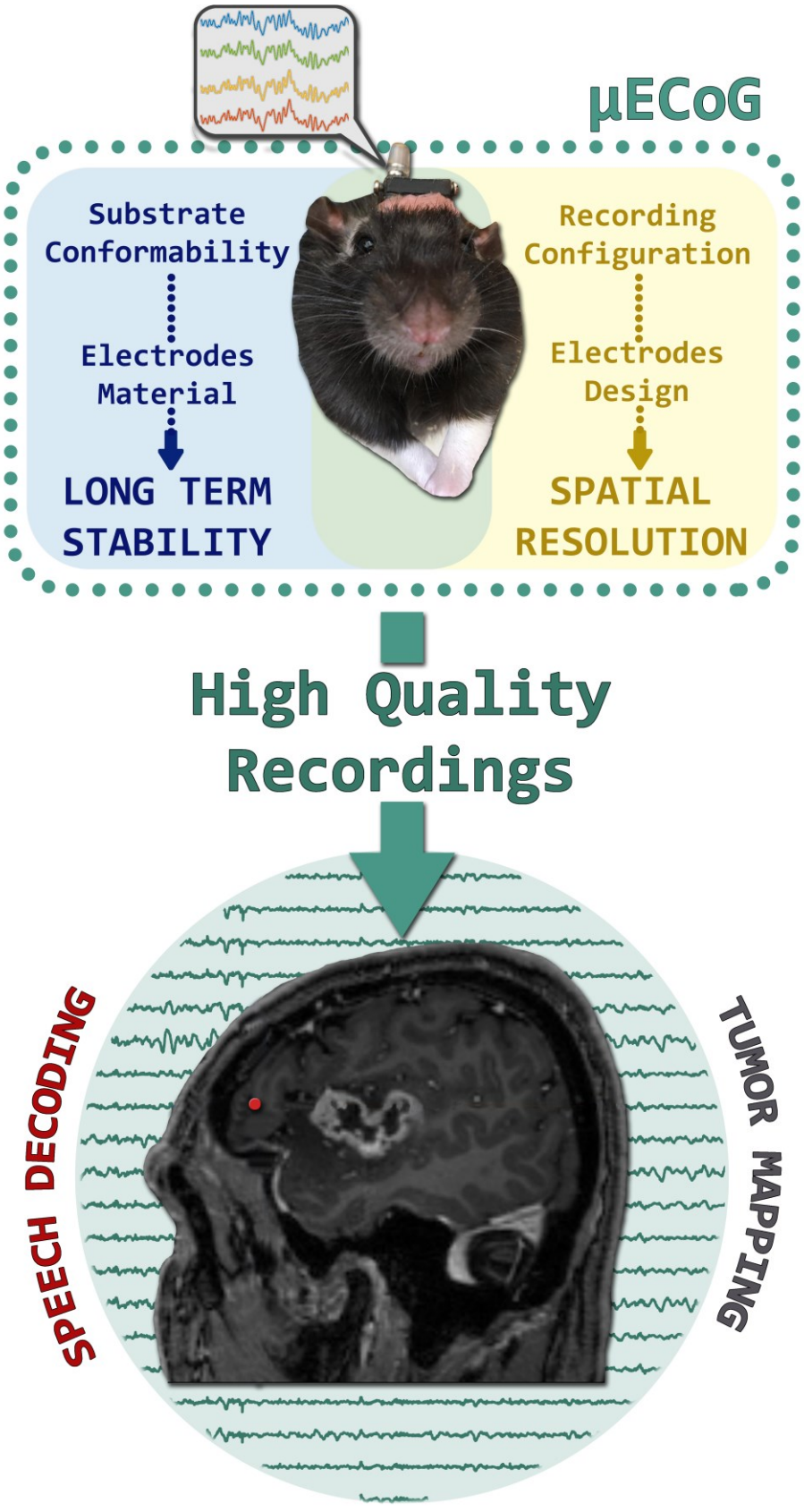
µECoG
Substrate Conformability
Electrodes Material
LONG TERM STABILITY
Recording Configuration
Electrodes Design
SPATIAL RESOLUTION
High Quality Recordings
SPEECH DECODING
TUMOR MAPPING

Chapter 1:

In vivo Performance Evaluation of Ultra-conformable µECoG Arrays

As the first step of this translational study, *in vivo* rat experiments were carried out to define which µECoG array features may play a role in high-quality neural recordings. A dual approach was used to address the long-term stability issue: on one hand, the mechanical compliance of the arrays to the neural tissue was improved by acting on the thickness of the substrate material (i.e., PI); on the other hand, different electrode materials, such as Pt, IrOx, and PEDOT-poly(styrenesulfonate) (PEDOT/PSS) were chronically implanted to validate their reliability in the long-term. Moreover, taking into account our previous experience [77, 79], glassy carbon (GC), a versatile and stable material, was eventually incorporated into a highly conformable PI substrate with a fenestrated and finger-like footprint. Thus, the neural recording capabilities of GC electrodes of different diameters were evaluated in acute implants. Regarding spatial resolution, I analyzed how different geometries (electrodes diameter and pitch) affect the information in different frequency bands, with particular interest in high-frequency recordings (multi-unit spiking activity). The degree of crosstalk between closely routed electrodes was assessed *in vitro* and *in vivo* by impedance measurements and by cross-correlation of the recorded neural signals [80]. Finally, as another possible strategy for improving spatial selectivity during signal acquisition, different recording configurations (single-ended and differential) and reference-on-the-array designs were explored.

1. Conformability: Bringing the Electrodes Closer to the Signal Source

Strategies targeting structural aspects of the implants themselves are very efficient approaches for lowering the FBR to neural implants, and in turn, for acquiring high-quality data. Probes with reduced dimensions and minimized bending stiffness and rigidity clearly exhibit beneficial impacts on the electrode–tissue interface [81, 83]. The mechanical interaction between implants and the surrounding tissue (known as structural biocompatibility) applies to both the initial device–tissue coupling and to their interactions over time in terms of micromovements and stress at the interface [84, 85]. When the mechanical mismatch between implants and neural tissue is reduced, the biotic–abiotic interface is stabilized and electrodes remain in close contact with electrically active cells. Therefore, the high quality of the recorded signals can be sustained for longer periods [81, 82].

Although they sit on the brain surface and do not usually disrupt the blood–brain barrier, the mechanical mismatch between soft brain tissue (Young's modulus of ~10 kPa) and polymer-based ECoG arrays (greater Young's modulus of 6–7 orders of magnitude) remains an unsolved challenge. Long-term surface implants face glial cell activation, encapsulation of the electrodes, and depression of the underlying tissue [61]. Recent technologies have attempted to eliminate these effects and improve the mechanical and electrical tissue–electrode contact by using ultra-thin and highly fenestrated substrates. In practical terms, this translates into: i) wide conformal coverage over the convoluted brain surface, (ii) increased contact area between the tissue and recording sites, and (iii) reduced substrate footprint. The latter effect, in turn, allows the diffusion of soluble factors through the device and reduces the inflammatory response [27, 82, 86].

By following this approach, the critical thickness for achieving conformability with PI-based μECoG devices on a rat brain (radius of curvature, 3 mm [87]) was calculated using a general elasto-capillarity model [29]. The threshold value for conformability was found to be 10 μm, meaning that 10-μm thick arrays are predicted to naturally conform to the curvilinear rat brain only through elasto-capillary forces and without any additional pressure or adhesive strategy. To validate the analytical result, fenestrated arrays of various thicknesses (below and above the conformability threshold of 10 μm) were fabricated and chronically implanted in rats for 6 weeks.

Specifically, 4-, 8-, and 12-µm thick MuSA devices were used to quantify the cortex depression induced by their presence. Histological thionin staining allowed clear highlighting of the effect of arrays with different degrees of conformability on the rat brains and thus enabled better evaluation of the devices' impact on the soft tissue in chronic scenarios (Figure 9B).

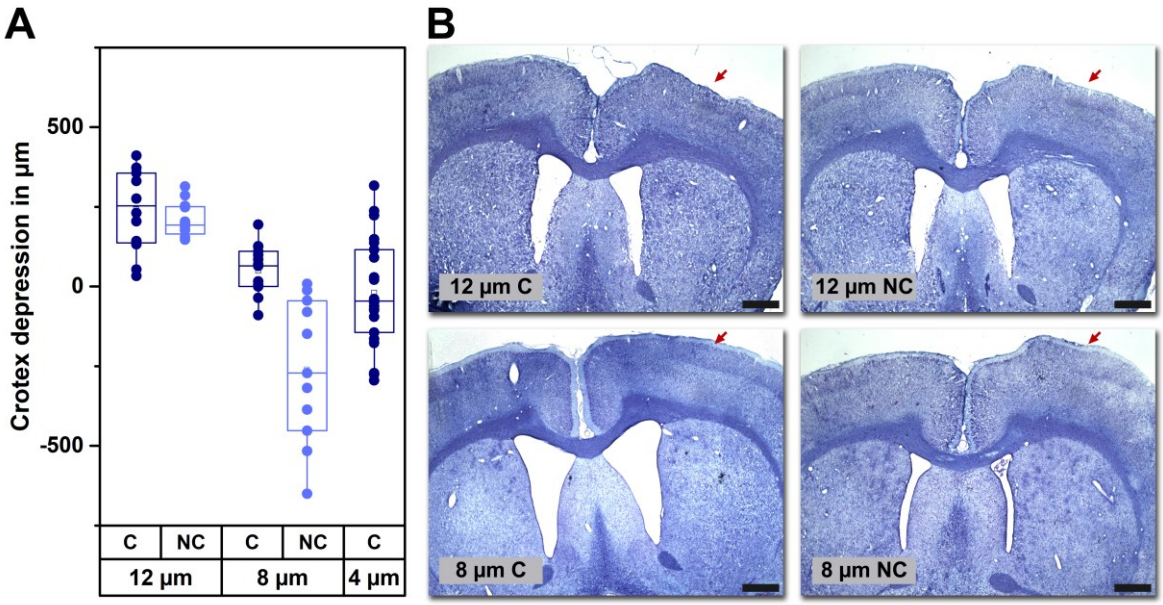

Figure 9 (A) Box plot of the cortex depression values calculated for each MuSA device implant. Negative values indicate swelling of the brain. (B) Representative brain thionin-stained slices of supra and subthreshold MuSA devices implanted for 6 weeks with and without connectors (C and NC, respectively). Red arrows indicate the region of the tissue under the implanted array. Scale bar = 1 mm.

Two types of implanting procedures were adopted for comparison purposes: type C (also used for recordings), where the PI devices were soldered to a connector fixed to the skull through a 3D-printed chamber and an acrylic cap, and type NC (only used for histological evaluations), where the PI devices were implanted without a connector and kept in place by a soft silicone-based polymer (Figure 35 in the Experimental Section). For NC implants, no acrylic cap or chamber was used to seal the craniotomy, and presumably negligible external pressure was exerted on the brain apart from that induced by the PI implants. The connector is necessary for creating an electrical connection between the implanted electrodes and the recording system. At the same time, it is accompanied by the need for a rigid cap or support that keeps the connector in place and allows access to it during recording sessions. Such a supporting structure usually surrounds the craniotomy and might have an influence on the deformation of the implanted brain. Therefore, to

distinguish the depression due to the PI implants from that induced by the headstage components, C and NC implants were performed and analyzed in parallel.

In accordance with the theoretical results, the thickness threshold value for conformability also appeared to lie within 8 and 12 µm for the *in vivo* analysis. Indeed, there were no statistically significant differences between the 4- and 8-µm thick MuSA devices implanted with the headstage components (Figure 9A, 4 µm C and 8 µm C), while the depression caused by the 12-µm thick MuSA device was significantly higher than that of the 8-µm thick MuSA device (Figure 9A, 12 µm C and 8 µm C). Moreover, when using subthreshold devices, physiological swelling of the brain (Figure 9B, 8 µm NC as an example of the phenomenon) out of the craniotomy borders was noted. The swelling of the brain is a consequence of the surgical intervention and is expected for any implant. However, counter-pressure can be generated by the presence of non-conformable devices forced to adhere to the brain and by the headstage components. When the counter-pressure is greater than the deformation caused by the swelling, the result is depressed and flattened tissue (Figure 9B, 12 µm C and NC). On the contrary, when conformable implants were used, they did not flatten the brain, but rather followed its curvature (Figure 9B, 8 µm C). The results also suggest that the presence of the acrylic and connector clearly has an effect on conformable implants as well, and for implants below the conformability threshold, it is the main cause of brain deformation (Figure 9A, 8 µm C and 4 µm C). The data are in line with a previous study conducted by our group [78], showing that mild activation of the inflammatory response attributable to the chronic setup per se (e.g., acrylic cap and screws) should be expected.

Cortical depression was also quantified in brains implanted for 6 weeks with 12-µm thick PI-based µECoG devices with the same percentage of fenestrated area over the solid PI substrate as for the MuSA devices (~17%), but with larger and less uniformly distributed fenestration holes within the electrode area (“poorly distributed fenestration”, PD in Figure 10A).

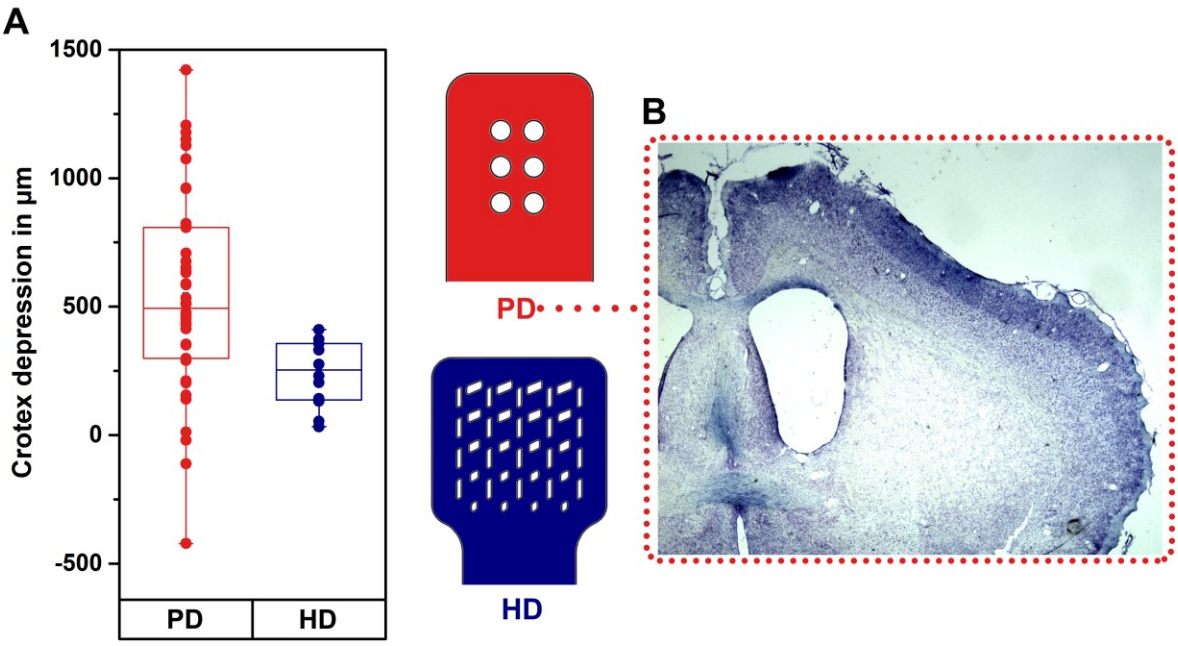

Figure 10 (A) Box plot showing cortex depression values calculated from brains implanted with a 12-µm thick PI-based ECoG with poorly fenestrated substrate (PD) and with a 12-µm thick MuSA device with highly fenestrated substrate (HD). The solid-to-fenestrated area ratio was the same for both the devices (17% of holes over the PI area), and both implant types were performed using connectors and headstage components. Schematics of the PD and HD devices are depicted to show the different distribution of the fenestration holes. Negative values indicate swelling of the brain. (B) Representative brain thionin-stained slice of a PD device implanted for 6 weeks.

The histological results (Figure 10) indicate that the brain depression greatly increased with devices with non-uniform fenestration when compared to all the other MuSA devices, i.e., conformable and non-conformable. Although they were fabricated using the same protocol and had the same total thickness (12 µm), the implants with non-uniformly distributed holes caused significantly greater brain depression than that caused by the MuSA devices ("highly distributed fenestration", HD in Figure 10A). The negative depression values obtained for the PD devices could be linked to the swelling of the brain through the large fenestration holes. Thus, by designing a mesh-like or fenestrated PI substrate, it is possible to improve the tissue–electrode interface even of non-conformable implants.

Additionally, *in vivo* implants performed using subthreshold (i.e., conformable, 8-µm thick) and suprathreshold (or non-conformable, 12-µm thick) MuSA devices were used to monitor electrode impedance for 5 weeks.

As expected, before implanting, electrodes of the same size had similar impedance independent of the thickness of the device to which they belonged (the *in vitro* curve in Figure 11 shows the impedance of a large Pt electrode in saline). After 1 week (Figure 11, W1), the magnitude of the impedance of both the conformable and non-

conformable electrodes remained comparable, probably due to a good initial tissue–electrode contact and to the increased wettability of the recording sites. At week 3, the impedance of the conformable electrodes remained the same overall, but that of the non-conformable electrodes increased significantly. This scenario was maintained until week 5 (Figure 11, W3 and W5). The behavior of the phase angle followed the same trend: starting from week 3, it reached a steady state in conformable implants while exhibiting more dynamic behavior (and thus it never stabilized) in non-conformable implants.

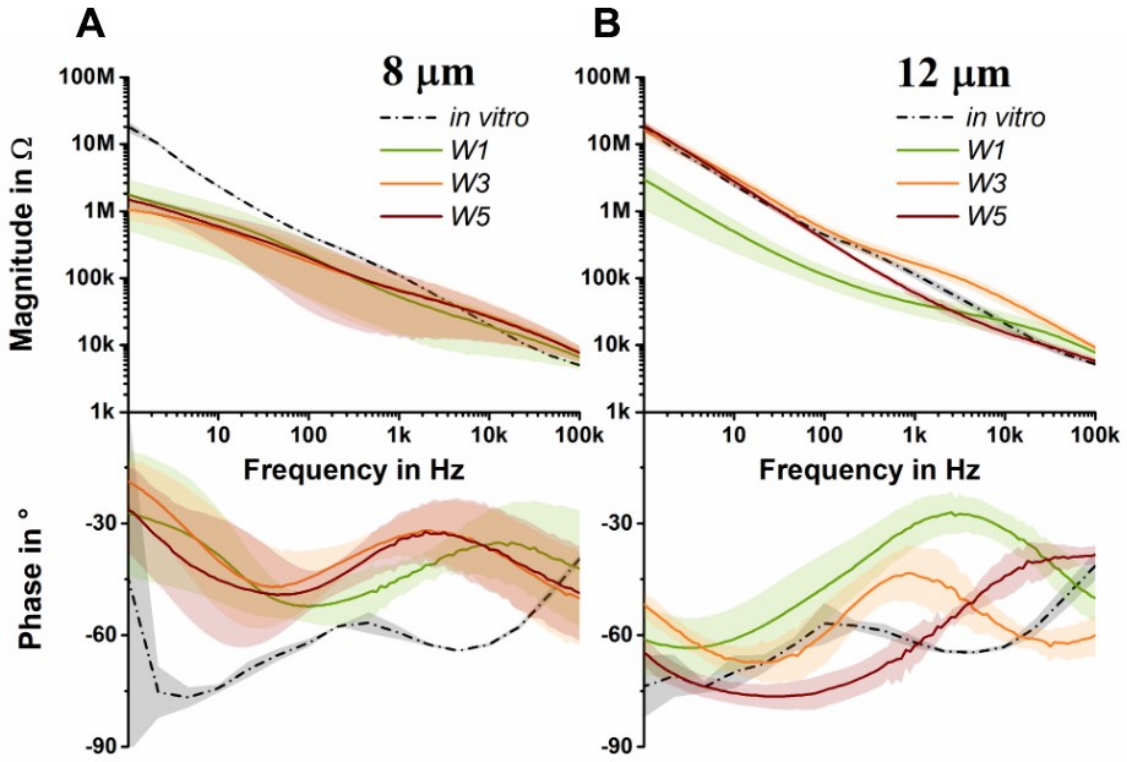

Figure 11 Bode plots (magnitude and phase) of 8-µm (A) and 12-µm thick (B) MuSA devices showing impedance measured *in vitro*, and after 1, 3, and 5 weeks from implanting (in rats). The diameter of the Pt electrodes, in both cases, was 100 µm (n = 4 per electrode type).

The fact that the impedance of the non-conformable electrodes increased over time could be ascribed to the type of interface they formed with the tissue: while the conformable device immediately adapted to the curvilinear surface of the brain, the non-conformable device, although forced to adhere to the brain surface, was not tightly bound to the tissue, but rather forcefully pushed onto it, and tended to assume a more energetically favorable shape/state over time. For the 8-µm thick device, the electrodes seemed to form a solid interface with the tissue and minimize the biotic–abiotic gap. Indeed, as shown in Figure 12, the ultra-conformable devices (metal-based MuSA and carbon-based CaLEAF [carbon LEAF] arrays) adapted perfectly

to the curvature of the rat barrel cortex and established strong contact with the tissue. With the adaptive and stable interaction at the electrode–tissue interface, it was possible to avoid both cortical depression and neuronal loss and to obtain high-quality recordings (see next sections for further details).

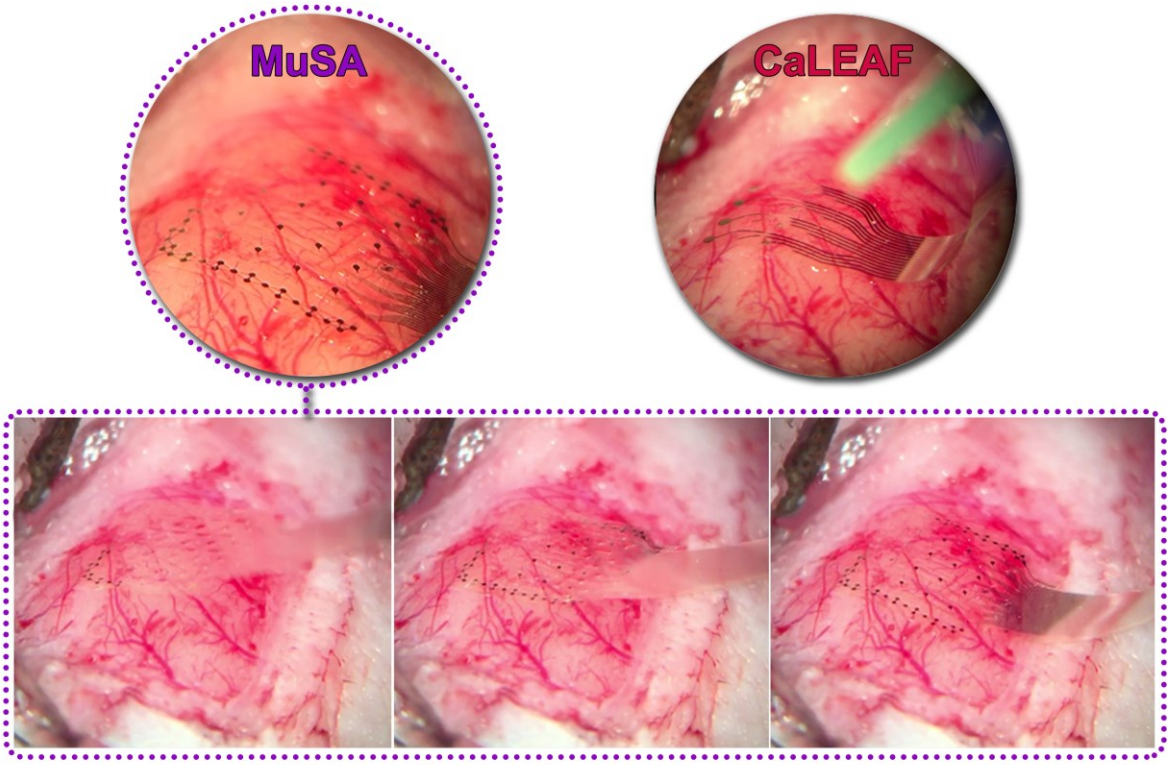

Figure 12 Pictures of the ultra-conformable μECoG arrays (8-μm thick) over the rat cortex: the MuSA array with metal-based electrodes and the CaLEAF array holding carbon-based electrodes. The sequence of pictures in the bottom row shows a MuSA array approaching the rat cortex.

2. High-frequency Recordings: Performance Evaluation of Different Electrodes Materials and Geometries

ECoG has become an important tool for applications such as brain tumor functional mapping, monitoring and preventing epileptic seizures, and BCI for controlling prosthetic devices [88–93], as it provides cortical activity mapping while remaining semi-invasive (the brain–blood barrier remains intact) [60, 94]. Moreover, as it has been demonstrated that action potentials, the main form of communication among neurons, can be detected from the surface of the brain [27], ECoG recordings represent the best compromise between the degree of invasiveness and the wealth of neural information. In fact, as reported by Bockhorst and colleagues [28], high-frequency signals (>200 Hz) recorded from the surface of the brain correlate to the synchronous spiking of the neurons in the underlying cortical layers. This result comes with two main advantages: i) no device insertion into the cortical tissue is required, and ii) the possibility of mapping the high-frequency cortical activity of large brain areas while preserving the spatial resolution (by using high-density µECoG devices) is enabled. The feasibility of resolving independent signals by using µECoG devices in humans and in animal models has been demonstrated previously [95–97]. Therefore, extending this achievement to higher frequency bands could yield new insights into the investigation of complex neural processes as well as great advantages in diagnostic and brain–machine interface applications. As such perspectives would imply long-term implants, the capability of the ultra-conformable (8-µm thick) MuSA devices for detecting multi-unit activity was verified in chronic scenarios (up to 12 weeks). Accordingly, while addressing the temporal resolution in long-term recordings, the spatial selectivity of micro-electrodes was investigated in parallel. On one hand, metal-based electrodes of different diameters (100 µm versus 10 µm) were compared. On the other hand, miniaturized electrodes (50, 100, 200, and 300 µm) of a novel material such as GC were evaluated in acute experiments focusing on different frequency domains.

2.1 Metal-based Electrodes Performances in Chronic Implants

Chronic experiments using 8-µm thick MuSA devices with Pt, IrOx, and PEDOT/PSS electrodes were performed to study the capability of different electrode materials to record high-frequency signals in the long-term, and to test the overall stability of the implants. To better preserve the cortex, the dura mater was left intact (devices were implanted epidurally), and possibly because of the low thickness of this membrane in rats (~80 µm) [98], no repercussions on the detection of the high-frequency components were expected. Only the implants that lasted a minimum of 6 weeks (four rats with Pt electrodes and another four rats with IrOx and PEDOT/PSS electrodes) were considered for the analysis. The failing implants (n = 2) reported issues at the interconnection board level rather than at the device or electrode level. Thus, MuSA arrays may maintain high-quality recordings even for >12 weeks (the longest recording shown in this study), as this time point was due to the conclusion of the investigation and not device failure.

To evaluate the three electrode materials' ability to discriminate burst-like activity triggered by the stimulation of rat whiskers (see Experimental Section for further details), spikes were detected, and peri-event time histograms were computed for all recording sessions, time-locking the detected spike events to the start of the whisker stimulation (Figure 13 shows an example of the 6-week time point).

All the tested materials could distinguish stimulus-dependent spikes from the ongoing activity with high peak/mean ratio values (PMR, see Experimental Section) at least up to 12 weeks (Figure 14A, B). Nevertheless, when compared to Pt electrodes, IrOx and PEDOT/PSS electrodes maintained an overall higher number of detected spikes in the long-term. Indeed, after 6 weeks from the implant day, the best case for Pt arrays was the capability for detecting 18.14 spikes/s, while IrOx and PEDOT/PSS arrays detected 32.78 and 34.12 spikes/s, respectively. The variability of the *in vivo* results can be attributed to different levels of anesthesia, the inflammatory course, and the intrinsic variability among animals. These factors have a substantial influence on the overall performance of the implants, but can hardly be controlled. An overall drop in the recording quality was observed with all tested materials after 3 weeks, but in most of the cases, the performances improved again after 6 weeks. This effect can be ascribed to the different phases of the inflammatory

response distinguished in acute (1–3 weeks) and chronic tissue reactions to the implanted devices [43, 99].

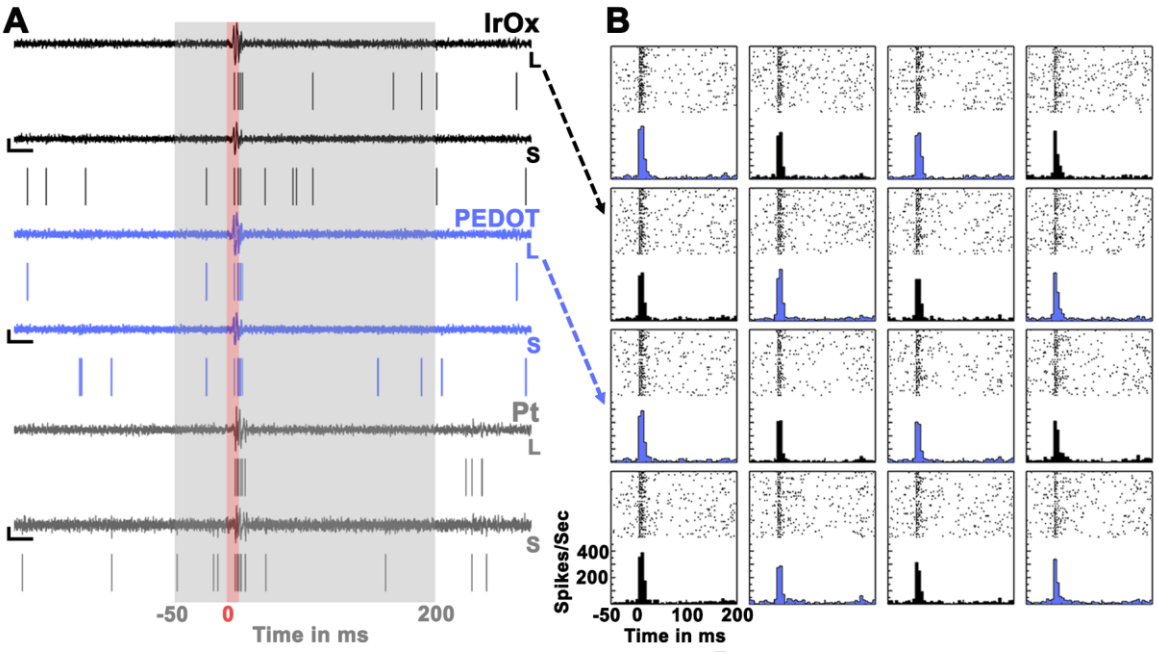

Figure 13 (A) Example of high-pass filtered traces recorded after 6 weeks (200 Hz, large [L] and small [S] electrodes belonging to the same couple for the three tested materials) and corresponding spike rasters (scale bar: 20 μV - 25 ms). Red background highlights the duration of the mechanical stimulation of the whiskers; grey indicates the time window used for the PMR calculation. (B) Representative raster plots and peri-event time histograms of the large IrOx and PEDOT/PSS channels after 6 weeks from implant day.

The design of the MuSA device was fabricated with the intent of having 16 recording sites (4 × 4 arrangement), each holding two electrodes with different diameters (10 and 100 μm), separated by a 45-μm gap, and recording from the same anatomical area (Figure 30C in the Experimental Section). Thus, it was possible to compare the recording capabilities of the two diameters directly. As shown in Figure 14A and B, higher PMR values were reported for the large electrodes on implant day for all electrode materials. However, consistently with the chronic impedance data shown in Figure 15, such critical difference in the recording quality between the large and small electrodes was resolved over time in all rats. In some cases, the relationship was even reversed (Figure 14C).

For all three electrode materials, it was observed that, starting from the first week after implanting, the impedance of large and small electrodes belonging to the same couple (i.e., placed about 45 μm from one another) became basically indistinguishable (Figure 15).

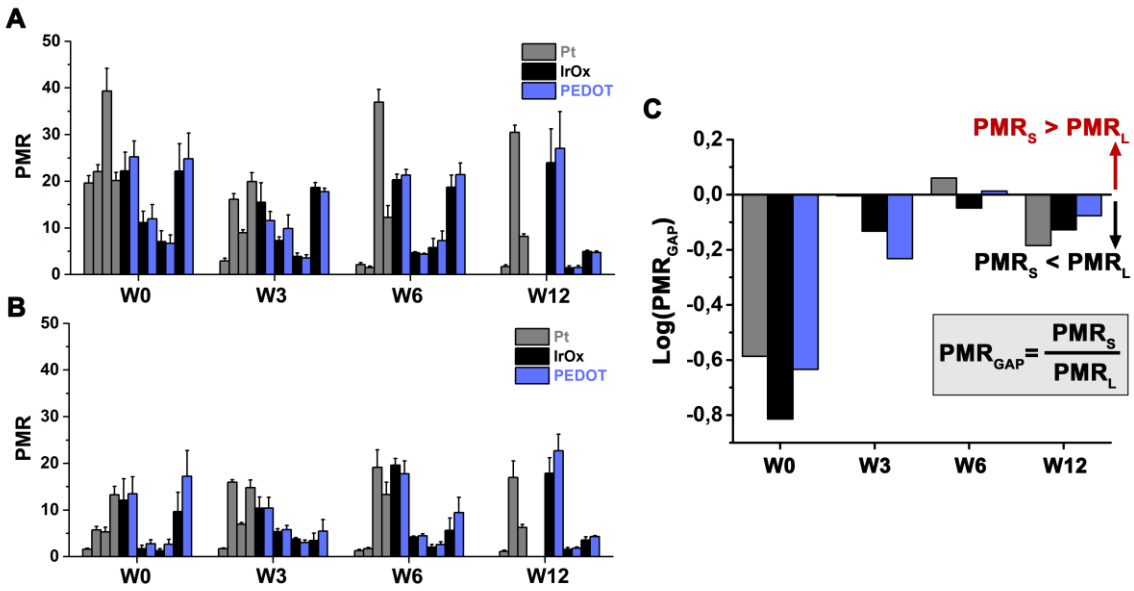

Figure 14 (A, B) Plot of the PMR values of large (A) and small (B) electrodes (mean of all channels ± SEM, each Pt rat, n = 16; each IrOx or PEDOT/PSS rat, n = 8) over the weeks for all the analyzed rats (total number of rats = 8, four Pt rats and four IrOx and PEDOT/PSS rats). Data belonging to the same rat are reported following the same order at each represented week. (C) Bar plot of the Log(PMRgap) calculated, as specified in the image, to compare the performances of the large and small electrodes over time. Representative data of one implant per type of electrode material are shown, but such results were consistent in all rats. Bar colors follow the same legend shown in A and B.

It should be noted that *in vivo* impedance was measured with a two-electrode setup using a distant skull screw as a reference/counter electrode. This arrangement provided an estimation of the conductivity path between the reference and working electrode, and was influenced by the eventual formation of fibrotic tissue around the implant. Between week 3 and week 6, the impedance of the small electrodes was even lower than that of the large electrodes. The logarithm of the ΔZ, defined as difference between the large electrode impedance ($|Z_L|$) and the small electrode impedance ($|Z_S|$), was the parameter used for interpreting the behavior of the tissue–electrode interface over time (Figure 15A). Such a value was positive for the first 2 weeks, and then became negative for all the electrode materials until week 12, when it reverted to positive. The Log of the ΔZ of a representative couple of large and small Pt electrodes in the 1 Hz to 100 kHz frequency range is plotted in Figure 15B. Here, it is clear that the inversion from positive to negative starts at week 2 and mainly affects the impedance values measured at frequencies below 2–3 kHz. At frequencies of >10 kHz, the large electrodes always had lower impedance than the small electrodes, although the ΔZ value decreased drastically between week 2 and week 6. At week 12, the overall situation reverted to the initial status, where the ΔZ value was positive in the entire frequency range.

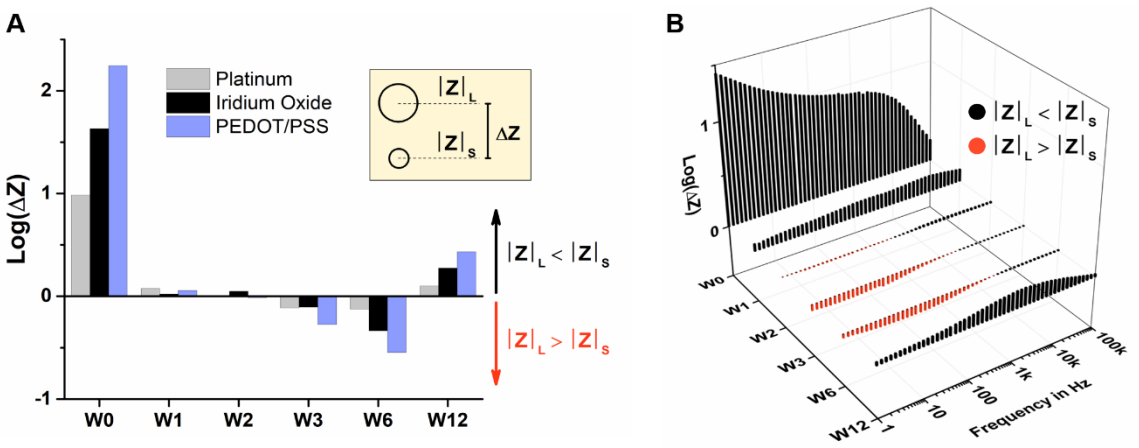

Figure 15 (A) Histogram showing the ΔZ, calculated as the difference between the impedance of a large and small electrode belonging to an electrode couple at 100 Hz, for three materials: Pt, IrOx, and PEDOT/PSS. (B) 3D plot showing the average impedance difference between a couple of Pt electrodes over the whole frequency range (1–100 kHz). In both (A) and (B), the gap is plotted over 12 weeks of implantation.

This scenario represents the majority of the performed chronic implants. In some of the implants, the impedance of the large and small electrodes over time did not follow a specific trend but rather was indistinguishable/superimposable after the second week from implantation. Although electrode impedance is theoretically highly dominated by the electrode area, after the first week in the brain, the geometric area of the implanted electrodes does not influence the measured *in vivo* impedance, which accounts for both electrodes and surrounding tissue. In the chronic implants performed in this study, the quality of the tissue–electrode interface disregarded the dimensions of the electrodes. Rather, it was determined by the coupling between the tissue and the electrodes, and the potential formation of glial scar.

In summary, no crucial difference in high-frequency recording capabilities was encountered when comparing Pt, IrOx, and PEDOT/PSS electrodes in the long-term. All the materials could detect sensory evoked multi-unit activity from the surface of the cortex up to 12 weeks. The overall better quality of the implant—as expected from the *in vivo* validations—seemed to be the key determinant of stable and reliable chronic recordings. Regarding the comparison between the large and small electrodes (100 vs 10 µm), the electrophysiological and impedance results consistently demonstrated that, after the first week of implant, performance disparities were annulled or in some cases even overturned.

2.2 Carbon-based Electrode Performances in Acute Implants

Among all the novel materials for neural interfaces, the main reason for the popularity of GC can be ascribed to its superior electrochemical stability, biocompatibility, and good long-term reliability [77, 78, 103]. Such non-graphitized forms of carbon have been incorporated into PI-based devices only recently [100–102], enabling the possibility of exploring its performance *in vivo*. Nowadays, this material is considered one of the most interesting solutions because of its capability to simultaneously serve as a recording, stimulation, and biosensing platform [104]. Nevertheless, the undeniable potential of carbon as an electrode material was thought to be restricted by the limitation in the miniaturization of the electrodes themselves—a fundamental prerequisite for fabricating high-density microarrays—due to the relatively low conductivity and high dimensional shrinkage during pyrolysis [105]. However, by increasing the surface and the structural biocompatibility of the device and focusing on the mechanical and chemical interaction of the whole implant with the host tissue, it was possible to improve the quality of the interface and the acquired signal by reducing the gap between the electrode and the neurons.

As a proof of concept, in this study, GC electrodes of different diameters (50, 100, 200, and 300 µm) were incorporated into a highly conformable PI substrate (8-µm thick) with a fenestrated, finger-like footprint (i.e., CaLEAF [79]). Subsequently, the conformable µECoG arrays were acutely placed over the rat barrel cortex (n = 5) in different positions to test the ability of each electrode geometry to record neural activity independently of its distance from the signal source. Moreover, an estimation of each diameter capability for detecting and discriminating the response evoked by one single barrel of the rat cortex [106, 107] was conducted by first stimulating all the whiskers simultaneously, and then only single whiskers.

For each position, the location of the largest recorded somatosensory evoked potential (SEP), identified as the signal source, moved on the electrode color-coded map consistently with the repositioning of the array on the cortex (Figure 16). When placed close to the signal source, in fact, every electrode, independent of its diameter, was able to record the largest peak-to-peak amplitude. Consequently, the resulting SNR values (Figure 16, bottom row) did not depend on the dimension of

the electrodes but correlated to the signal source location and signal intensity. Two main pieces of evidence led us to conclude that larger neural responses were mainly related to the location of the arrays rather than to the electrode diameter. First, SNR values of identical site diameter reported a large deviation, and this effect was clearly associated with the position of the array over the barrel cortex. Indeed, very small SNR values (channels 1, 2, 3, 4, 5, 8, 9, and 13 in Figure 16A) corresponded exactly to the electrodes that were more likely to be far from the center of the barrel cortex (i.e., the most posterior or medial ones). Second, a reversed trend of the SNR values was obtained after just repositioning the array over the cortex with a 90° rotation (Figure 16B). In this case, the smallest SNR values also belonged to the most posterior channels (channels 13, 14, 15, and 16 in Figure 16B).

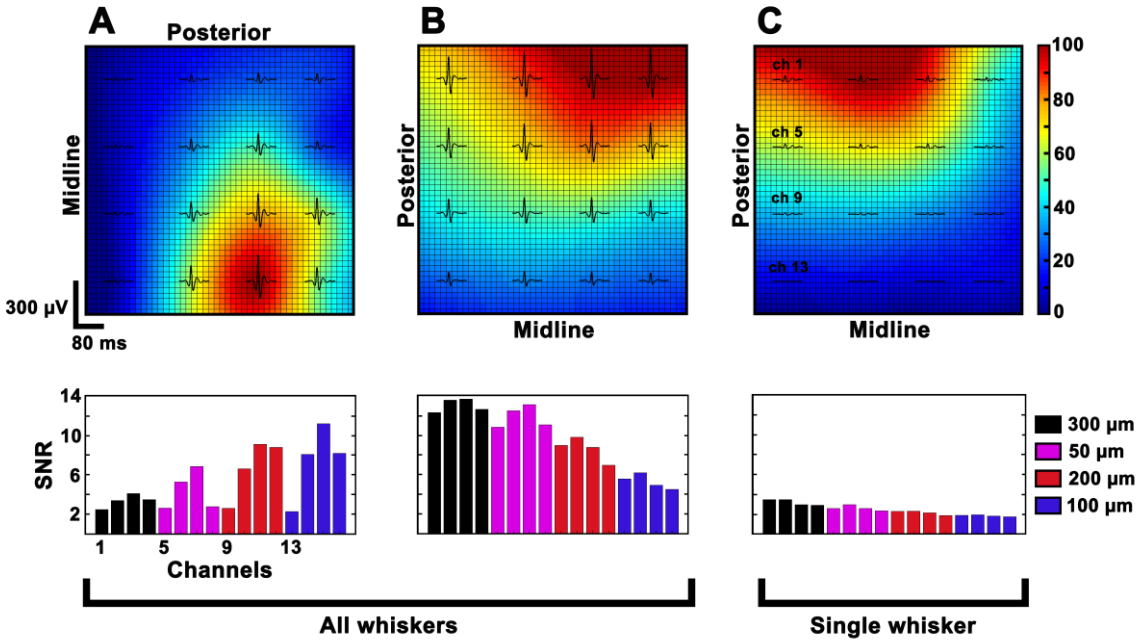

Figure 16 Representative interpolated maps of the averaged SEPs (first row) recorded in different positions (A, B) or in the same position but stimulating all and single whiskers (B, C). The colormap reflects the SEP sizes normalized in the range [0, 100] independently for each experimental condition. The second row shows the corresponding SNR histograms, which show how the same electrode can take high or low values depending on its position or the signal intensity. (From Vomero M. *et al.*, 2018)

When only single whiskers were stimulated (Figure 16C), smaller SEP amplitudes and lower SNR values were expected due to the reduced population of neurons involved in the task (with respect to the all-whiskers case of Figure 16A and 16B). In accordance with the barrel cortex organization, depending on which whisker was stimulated, the relative somatotopic shift of the neural response was detected with every electrode independently of its diameter (Figure 17). Ultimately, with SEP

recordings, no relevant difference between the recording performances could be associated to the different electrode diameters; all of them proved to be capable of reliably mapping the distribution of cortical sensory processes evoked by peripheral stimulation (Figures 16, 17).

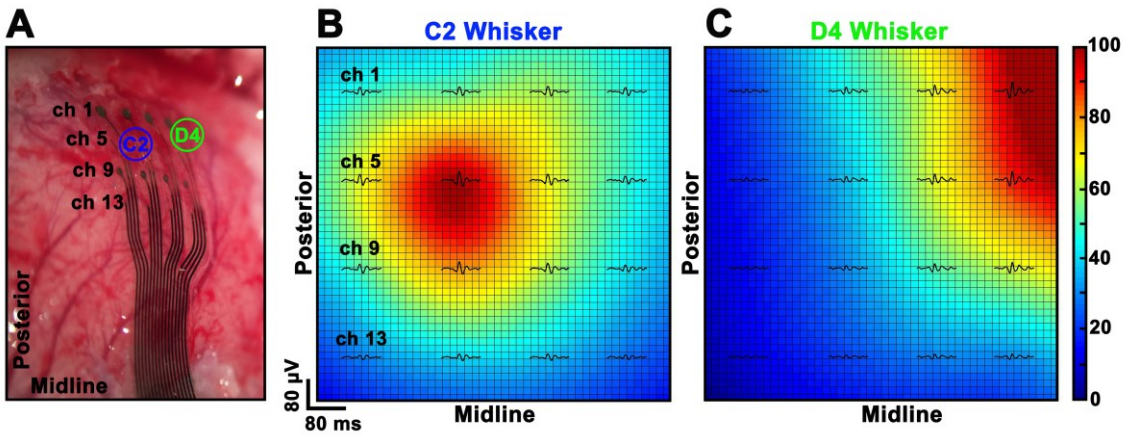

Figure 17 (A) Picture of the array over the barrel cortex where the position of the barrels of interest are overlaid. (B, C) Interpolated maps of the averaged SEPs obtained after stimulating the C2 and D4 whiskers showing the expected somatotopic shift. The colormap reflects the SEP sizes normalized in the range [0, 100] independently for each experimental condition. (From Vomero M. *et al.*, 2018)

Differently, a meaningful distinction between the diameters was noted in the high-frequency domain (>200 Hz). Indeed, the background noise band of the electrode increased along with the reduction of the electrode diameter, except for the transition between 300 and 200 µm, which did not show significant changes (Figure 18). This phenomenon had no remarkable consequences on the acquisition of slow and large neural responses (e.g., SEPs), but it may be a non-negligible issue when aiming to record faster and smaller neural signals such as spikes. In this case, spiking activity could remain totally embedded in the background noise, thus remaining indistinguishable. Such a setback prevents the possibility of recording the whole range of frequencies composing neural signals. When aiming to untangle the complexity of brain functions, the ideal neural device should be able to detect oscillations spanning from the slow and widespread varying potentials to the spatiotemporally resolved spiking activities. In this manner, neural interfaces would give access to a highly resolved picture of neural signals, holding the key to understanding the interplay within and between neural networks. Thus, smart strategies for achieving this goal should be sought. As presented in the Introduction, several routes can be taken to contrast the impedance increase—which in turn lowers the quality of the signal—experienced by miniaturized electrodes. Our

approach to addressing the noise band widening inclined towards the electrochemical deposition of PEDOT/PSS onto pristine GC electrodes (Figure 18B). As expected, the background noise band of the smallest electrodes (50 and 100 µm) was significantly reduced by the deposition of the CP. Specifically, small geometries showed values comparable to those of the larger electrodes (200 and 300 µm) that remained basically identical. Indeed, as well known from the literature, when compared to uncoated microelectrodes, high–surface area coatings exhibit lower impedance and higher SNR ratios [77, 108–110].

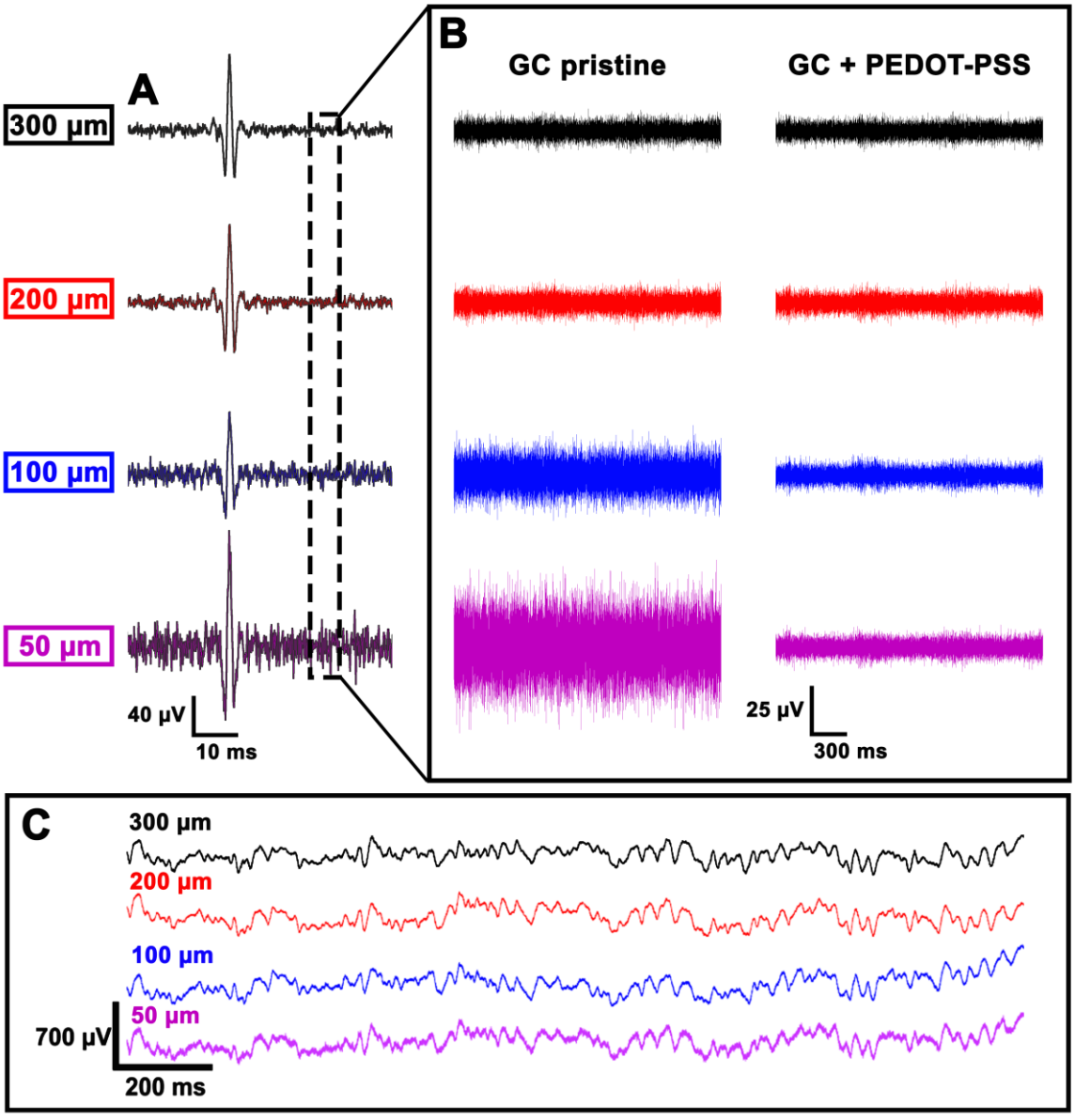

Figure 18 Representative continuous traces of one trial (A) recorded by all electrode diameters after high-pass filtering of data > 200 Hz. Box (B) represents the magnification of a small time window of spontaneous activity to highlight the background noise for every electrode diameter before and after PEDOT/PSS deposition. Box (C) shows ECoG raw data recorded from channels of various site diameters. (From Vomero M. *et al.*, 2018)

The “noisy” behavior of small diameters should not be ascribed to miniaturized GC electrodes per se. Metal-based devices (i.e., MuSA arrays presented in the previous section) were affected by the same phenomenon. Similarly, no differences between large (100 µm) and small (10 µm) Pt contacts were noted in the low-frequency band recordings (spontaneous or averaged activities such as SEPs). Instead, when aiming to detect low-noise multi-unit activity, PEDOT/PSS deposition played a crucial role for this purpose. A milder effect was seen for IrOx electrodes; possibly due to their natural roughness, similar high-frequency background noises were reported for the large and small electrodes, making the addition of PEDOT/PSS superfluous. It should be noted that, such observations refer only to acute scenarios. For chronic implants, based on impedance measurements and the quality of the recorded signal evaluations, performance disparities between different geometries were resolved over time, or in some cases, even overturned (see previous section for further details).

3. Crosstalk Assessment for High-frequency Recordings

The term crosstalk refers to the undesired coupling between two transmission lines (e.g., routing tracks of µECoG arrays), that is, the so-called active and passive lines. Galvanic (or resistive) coupling defines the physical contact between the lines (separated by an insulator as insulation resistance) and is independent of frequency, while capacitive coupling, arising from displacement currents generated by time-varying potentials across the lines, increases with frequency [111, 112].

As discussed in the Introduction, multiple causes (e.g., chemical reactions, film degradation, and mechanical stress) may induce the degradation of insulating layers, in turn introducing unintended parasitic current pathways. In a similar manner, it is expected that, when pushing the technology to its limit—as with high-density and ultra-thin devices (e.g., the MuSA and CaLEAF arrays evaluated in this study)—the risk of increasing crosstalk beyond what can be considered negligible becomes higher. Thoroughly investigating how much can crosstalk compromise recording quality becomes critical, especially in combination with a growing interest, as in our case, in extending the µECoG recording frequency band to the kHz range. Raising awareness of the issue of crosstalk was a response to the experimental observation of highly coherent signals (Figure 19A) registered by electrodes with neighboring tracks, even if placed far apart on the MuSA, in particular in the high-frequency band (500–6000 Hz). Therefore, after exploring the side effects of this phenomenon on the multi-unit activity recordings, the crosstalk between closely routed tracks was evaluated *in vitro*. Specifically, an impedance spatial sweep over the 32 tracks of the MuSA device was performed in phosphate-buffered saline (PBS) as a means of assessing the leakage resistance and capacitance between signal lines [80].

The coherence matrices and cross-correlograms computed from the *in vivo* data are shown in Figure 19, using the top right large electrode (100 µm) as the reference variable (R in Figure 19) of the calculations. Focusing on the coherence plots obtained from the data collected on implant day (Figure 19A, W0), it was evident that in the high-frequency band (>500 Hz), the R electrode showed high coherences with the electrodes disposed on the same column, which happened to be routed side by side along the track body (Figure 20A, Block 2–3). Nonetheless, the same

electrode did not share the same coherence level with the top electrodes of the neighboring column, which were very closely arranged on the array (Figure 20A, Block 1) but whose routing tracks were very far apart on the track body.

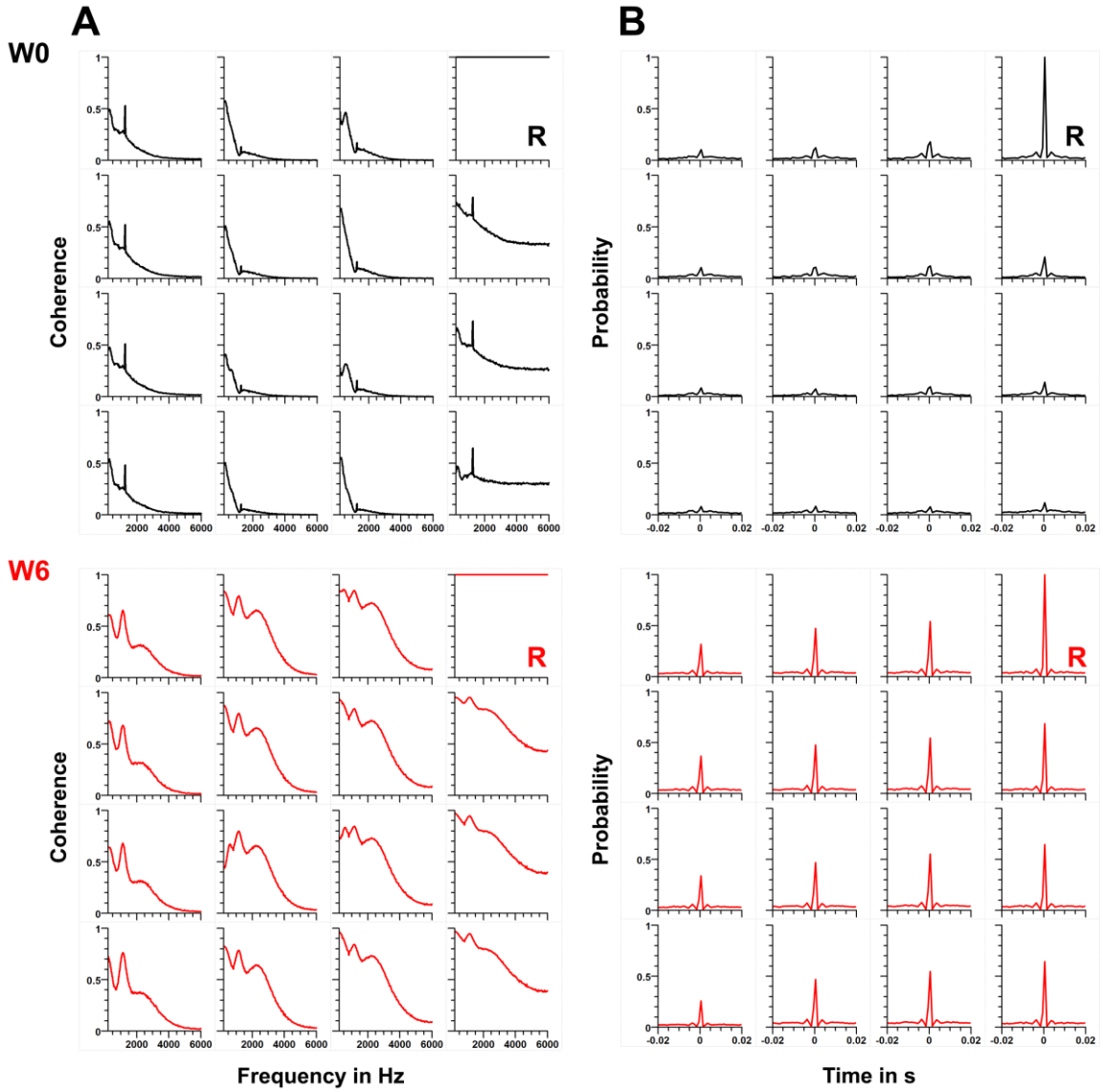

Figure 19 (A) Coherence matrixes (200–6000 Hz) of the large electrodes of the MuSA displayed following their arrangement over the rat cortex. The analysis was computed using the top right electrode as the reference variable (R in the image) on 300 s of spontaneous activity recorded on implant day (W0) and after 6 weeks (W6). (B) Cross-correlograms of the detected spike events using the spiking activity of the top right electrode as the reference variable (R in the image). As in (A), the same large electrodes of the MuSA are displayed following their arrangement over the rat cortex. Results at 0 and 6 weeks after implant (W0 and W6, respectively) are shown.

Moreover, similar effects were observed between columns placed on opposite sides of the array. This tendency, along with the column trend, was even clearer in a set of data recorded with the MuSA immersed in PBS (data not shown). Indeed, while the connection lines of these two sets were maximally separated at the track body,

their routing ended at the same row of pads interfacing the nanostrip connector (Figure 20A, Block 4). Thus, such coherence levels seemed to be completely unrelated to the distance between the actual electrode sites on the array, but appear highly dependent on the distance between routing tracks and on the track end-connection to the connector. Any physiological explanation for the trend was discarded by its recurring observation in the PBS control experiments. Moreover, further evidence was found when shifting the reference electrode used for the coherence calculation. Indeed, the resulting column trend was recursive for each of the four columns composing the electrode matrix.

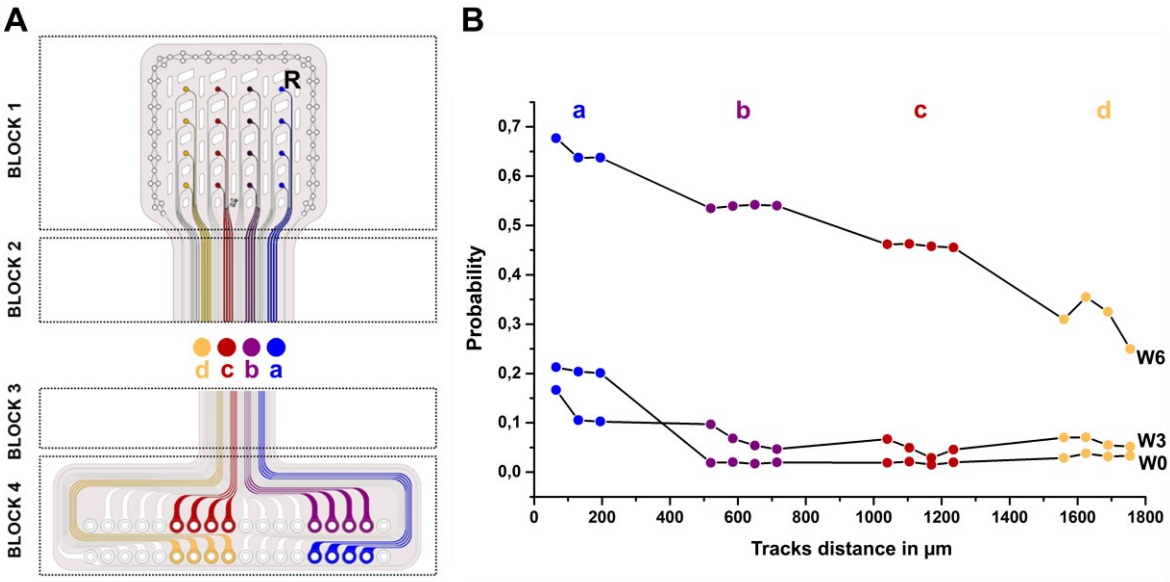

Figure 20 (A) Routing scheme of the 32 electrodes composing the array. Track subsets a, b, c, and d, colored blue, purple, red, and yellow, respectively, correspond to the four columns of large electrodes. The position of the electrode used as the reference variable for both coherence and cross-correlogram analysis is marked on the array (R in Block 1). The device is divided into four blocks that indicate the array (Block 1), the track body (Block 2–3), and the nanostrip connector (Block 4). (B) Plot of the synchronized spike probability after sorting the channels by following the track distances in Block 2–3. Labels and colors refer to the track subsets shown in (A). Channels used as reference value (R in the array sketch) of the calculation are not reported. Data are presented for the recordings performed at 0, 3, and 6 weeks (W0, W3 and W6, respectively) after implant. *(*Adapted from Cruz M. F. P. *et al.*, 2019)

Cross-correlograms of the detected spike events using the spiking activity of the top right electrode as the reference variable were performed to understand how the crosstalk could affect the multi-unit activity recordings (Figure 19B). In line with the coherence plots, high probabilities of detecting synchronized spikes with different electrodes seemed better related to the track distance rather than to the actual spatial distribution of the electrodes over the rat cortex. To corroborate this

hypothesis, the probability values—extracted as the maximum value of the cross-correlogram plots—were sorted by track distance (Figure 20B). As predicted, a decreasing trend was found, with overall higher and similar values within consecutive columns (column a–d in Figure 20). On the contrary, according to the cortical arrangement of the rat brain, electrodes close on the recording site portion of the device (Figure 20A, Block 1) were expected to share more common neural activity.

As both galvanic and capacitive coupling depend on the surrounding medium, and on the water uptake of the polymer insulating the lines [113, 114], it was unsurprising to encounter progressive enhancement of the crosstalk effects during chronic evaluations (Figure 19A, B and Figure 20B). Indeed, after 6 weeks of implantation, a general increase in coherence values was recorded for all electrodes (Figure 19A), and the number of synchronized spikes increased consistently for all channels independently of their position on the array (Figure 19B). Interestingly, as shown in Figure 20B, the decreasing trend was maintained, meaning that even after 6 weeks—and regardless of the overall enhancement of the phenomenon—the dependence of such side effects remained clearly related to the track distances. All the aforementioned considerations should be interpreted as independent of electrode diameter. Indeed, the same results were obtained for the small electrodes (10 µm) of the MuSA (data not shown) and across different subjects.

The main raison µECoG is increasingly gaining popularity involves its capability of resolving independent signals at the submillimeter scale [95–97]. Therefore, crosstalk—and more specifically how this phenomenon compromises the spatial specificity of multi-unit activity detection—undoubtedly represents a major concern for this application. Moreover, as this undesired coupling is predictably enhanced by several effects related to the close and protracted interaction between neural interfaces and neural tissue, the possibility of reliably mapping high-frequency signals in the long-term— the raison d'être of such neural devices—becomes extremely challenging.

As the first step towards finding efficient strategies to confine crosstalk, the combined leakage resistance and capacitance between the signal lines and the targeted brain tissue was estimated *in vitro*. With this aim, an impedance spatial sweep over the 32 tracks routing the MuSA electrodes was collected in PBS in a two-electrode electrochemical impedance spectroscopy setup. The *in vitro* impedance sweep of all 31 tracks (one track was used as the counter electrode) of

one representative device is displayed as a Bode plot (Figure 21), with each curve referring to one of the 31 tracks set as a working electrode at a time to investigate the transfer behavior and frequency dependence of the voltage–current relation. Consistent with the *in vivo* results, the magnitude increased gradually from the nearest to the furthest track (fading from blue to red), with an overall value of 22.0 ± 1.5 MΩ at 1 kHz. Closer tracks showed a resistive component up to 3 kHz, while further tracks demonstrated fully capacitive behavior below 1 kHz (90° phase).

The column trend observed in the *in vivo* data suggests a threshold impedance between signal lines and connection pads, below which the crosstalk becomes critical. This idea is in accordance with the impedance spectrum between track pairs, which shows a shift from a resistive–capacitive behavior between nearer tracks to fully capacitive behavior between further tracks in the considered frequency band.

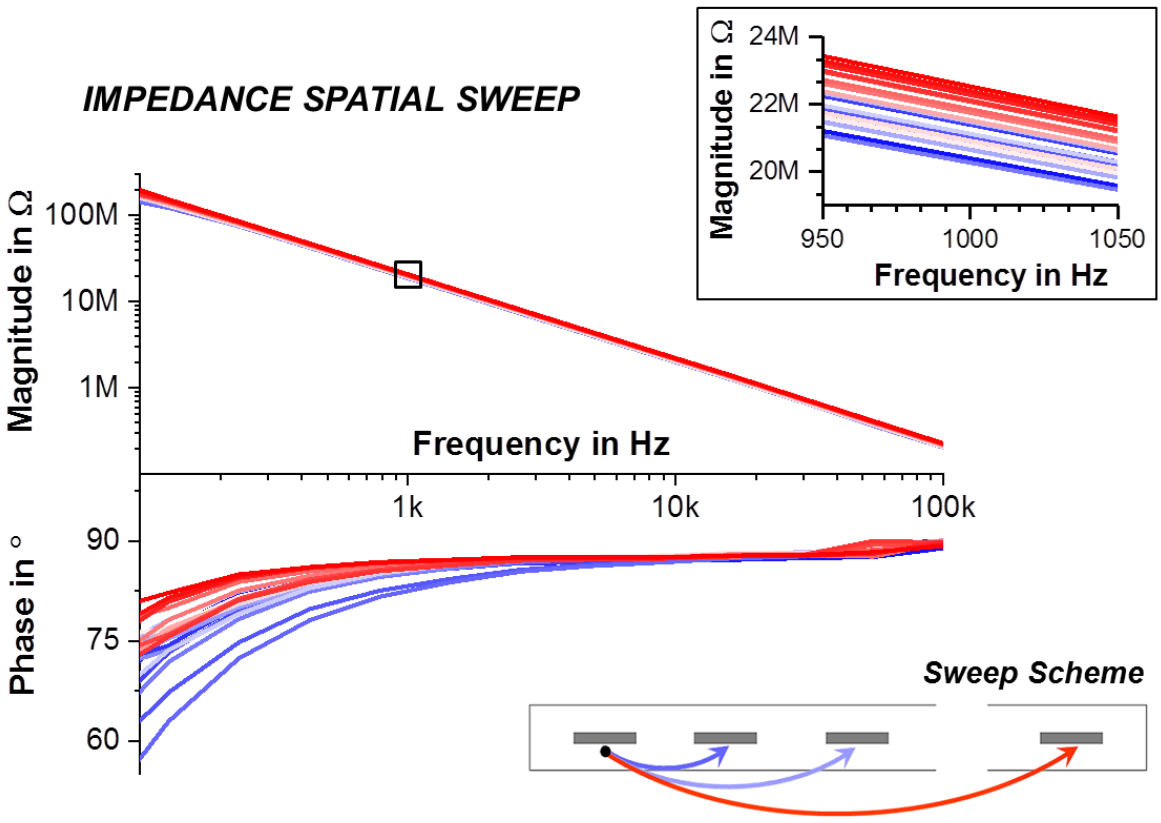

Figure 21 Bode plot representative of the impedance spatial sweep over the 32 tracks composing the MuSA, using the leftmost track as the counter. The color gradient from blue to red represents the increasing distance between the counter and the working track. (From Cruz M. F. P. *et al.*, 2019)

The setup used for the impedance sweep discarded the electrode–electrolyte interface by placing the array outside the solution while the track body remained

immersed. In theory, however, the initial segment of the tracks branching from the array area should also be included in the measurement. One possible means of overcoming this would be to perform the same sweep using a testing device with closed electrodes (not etched openings), which could be fully immersed in solution. In addition, the influence of residue on the contact pads and on the surface of the device at the connector level could lead to decreased insulation resistance between adjacent lines. This effect, as well as the contribution of the passive electrical properties of the neuronal target tissue (load impedance), will be investigated in a more comprehensive study to derive a model of a transmission line taking into account all the different components. This model could aid the design of micro-electrode arrays according to its spatial limits and with a minimum level of crosstalk for high-quality µECoG recordings of LFPs and spiking activity.

4. Recording Configurations: Improving the Spatial Resolution

Standard configurations for neurophysiology recordings can be categorized into single-ended and differential, which mainly differ by the number of electrodes and how they are connected at the headstage level. The term working electrode (W_e) refers to the electrodes placed right on the source of the potentials of interest, while reference electrode (R_e) indicates electrodes placed in the vicinity of the working electrodes with the aim of picking up common noises but not the potentials of interest. Lastly, ground electrodes (G_e) are placed at sites with an averaged stable potential, usually relatively far from the active electrode (e.g., skull screw placed on the contralateral hemisphere or the dura mater in human recordings). Accordingly, at the headstage level, three different connection pads (W_e, R_e, and G_e) interface as many amplifier inputs (Figure 36 in the Experimental Section). Regardless of which type of configuration is selected, the analog input of the amplifier (non-inverting input) is wired to a working electrode and the amplifier ground pin is connected to a low-impedance electrode at a stable potential (e.g., skull screw). In single-ended recordings, the reference and ground pins are tight together at the headstage level and connected to a skull screw. In this manner, the potential of a working electrode is measured with respect to a non-active reference. Such a configuration is used whenever the signal of interest is relatively large in comparison to noise signals (e.g., LFPs). On the contrary, when using differential configurations, the reference and ground pins are decoupled at the headstage level, requiring a minimum of three electrodes: working electrode, ground electrode, and one reference electrode close to the working electrode. Common-mode signals, as noises or offsets arising from impedance mismatch between the ground and differential electrodes (W_e and R_e), are rejected, allowing the amplification of very small differential-mode signals. One disadvantage of this configuration is that, despite the spatial arrangement of the reference on the probe, it can pick up signals of interest, which are ultimately subtracted from the active recordings. Nevertheless, differential configuration could be very useful when aiming to record single- or multi-unit activity.

According to these fundamentals, two different reference designs of the MuSA (crown and branched, Figure 31 in the Experimental Section) were tested using a differential configuration and compared to the outcomes obtained with the single-

ended design. The reference and ground pins were coupled and decoupled through a switch solder on top of the headstage, enabling a direct comparison between the performances of the two recording configurations.

As expected from an evaluation regarding low-frequency oscillations (3–300 Hz, peripherally evoked potentials), when compared to the signals detected with single-ended configuration, smaller peak-to-peak amplitudes were ascribed to the recordings collected in differential referencing mode with both types of reference design (Figure 22).

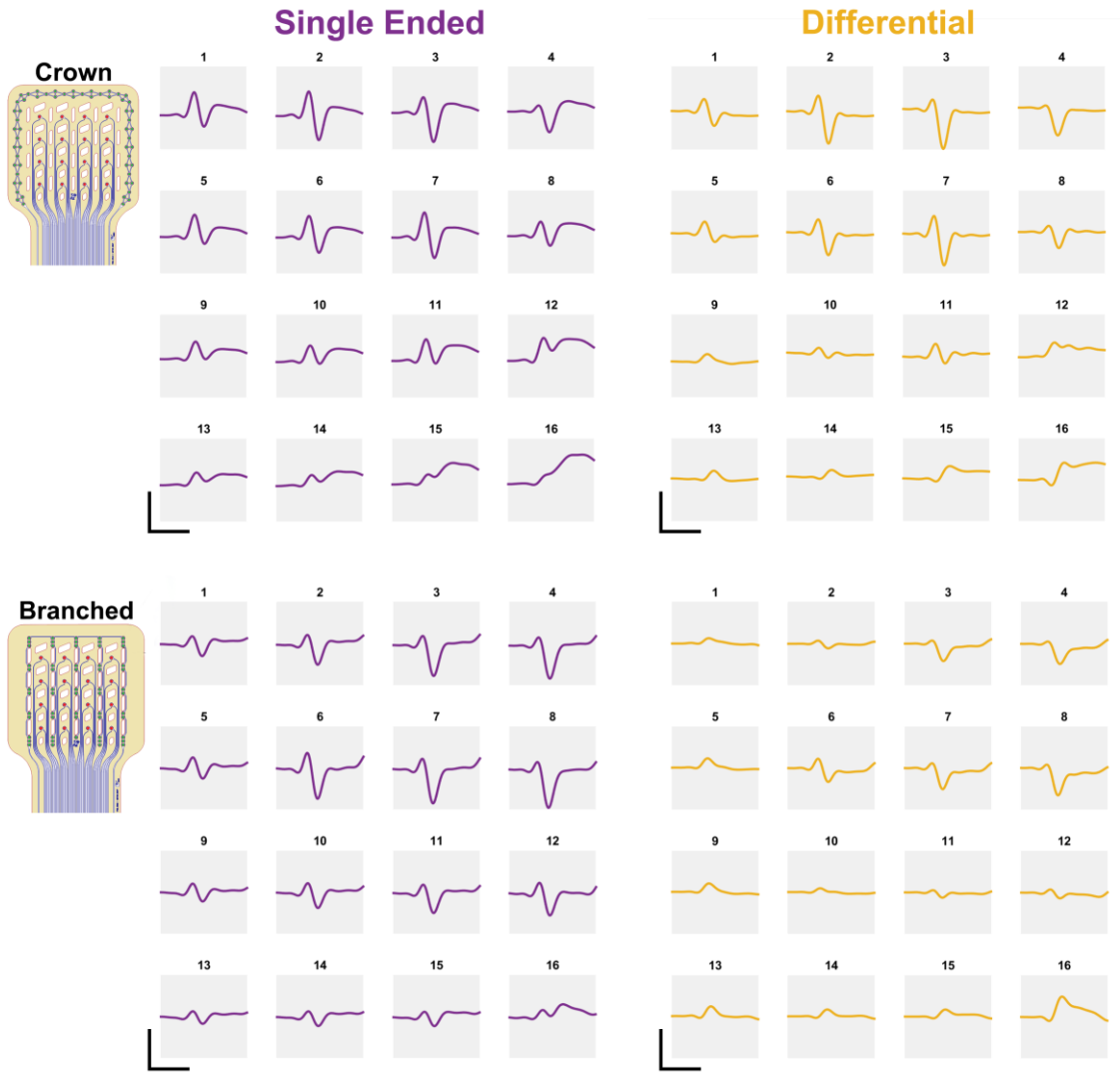

Figure 22 SEP maps of band-pass–filtered data (3–300 Hz, mean of 60 trials) reported for both recording configurations and reference designs collected on implant day. Large electrodes of the MuSA are displayed following their arrangement over the rat cortex. Scale bars measure 600 µV – 40 ms.

The fact that more focalized activations were obtained when using a differential configuration could be construed as an improvement of the recordings' spatial resolution. Nevertheless, as a phase reversal of the evoked potentials emerged due

to the subtraction of the potential fluctuations caught by the reference electrode, these anti-correlated signals could yield misleading interpretations when aiming to investigate still unknown neural responses.

On the contrary, for multi-unit recordings, positive effects were attributed to the use of a differential configuration. Indeed, without compromising the overall number of detected spikes (Figure 23), better performances were obtained in terms of: i) number of synchronized spikes detected from different electrodes (Figure 24), and ii) coherence values of the recorded signal (Figure 25).

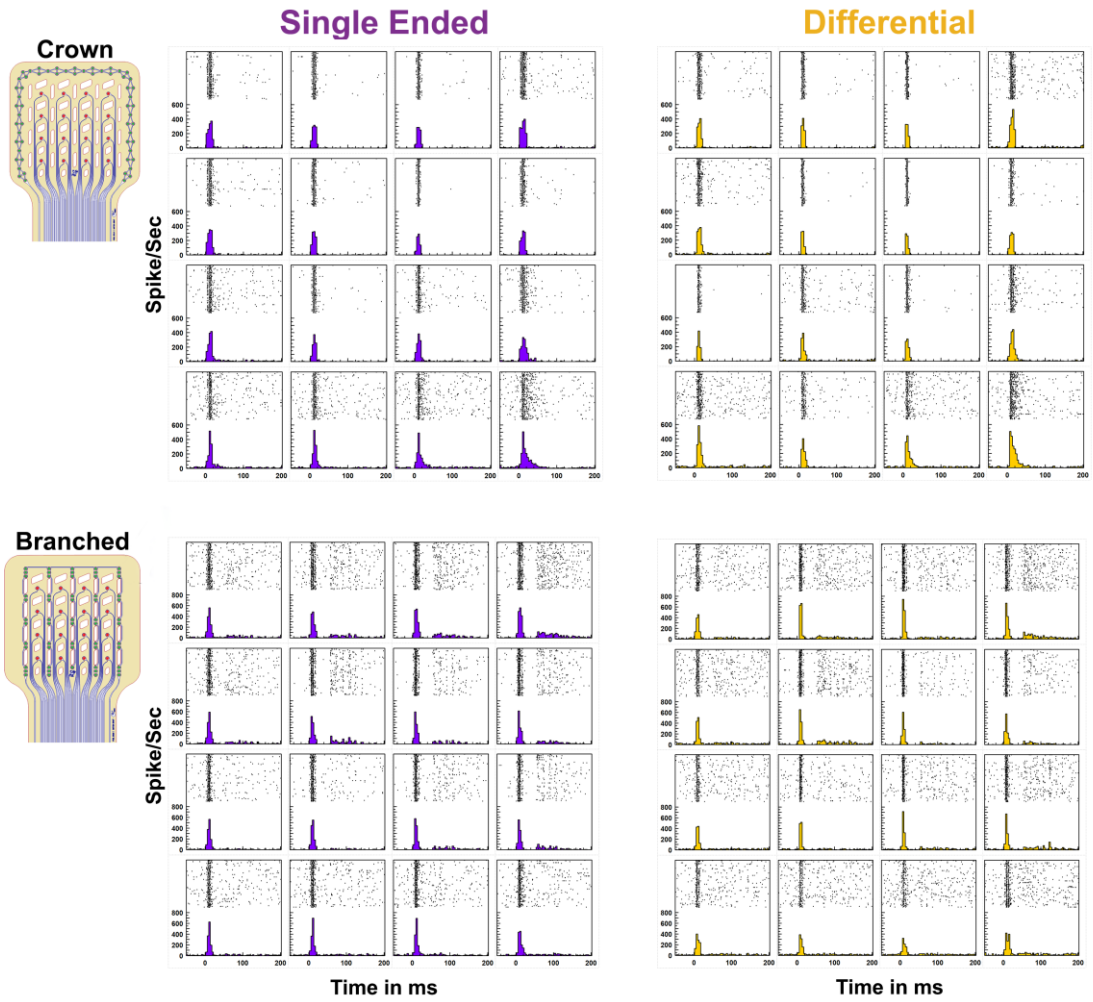

Figure 23 Raster plots and peri-event time histograms of large MuSA electrodes (implant day recordings). Data are reported for both configurations and reference designs and time-locked to the start of the whisker stimulation (spike counts of 60 trials). Electrodes are displayed following their arrangement over the rat cortex.

Based on the raster plots and peri-event histograms in Figure 23, it is clear that the number of detected spikes evoked by peripheral stimulation remained basically unchanged when taking advantage of a crown-shape reference in a differential configuration. Differently, the results obtained with the branched design showed a

slight decrease in the number of spikes detected from some electrodes (bottom row in Figure 23). More interestingly, in differential recordings, there was an overall decrease in the probability of detecting the same spontaneous spiking activity with different electrodes (Figure 24). As expected from an intermingled arrangement, the impact was even more evident when using the branched design with respect to the crown design (reference electrodes are placed around the recording site area). Therefore, when extending the frequency range of interest towards the spiking activity, recordings in differential referencing mode represent a valuable approach to avoid the detection of redundant information.

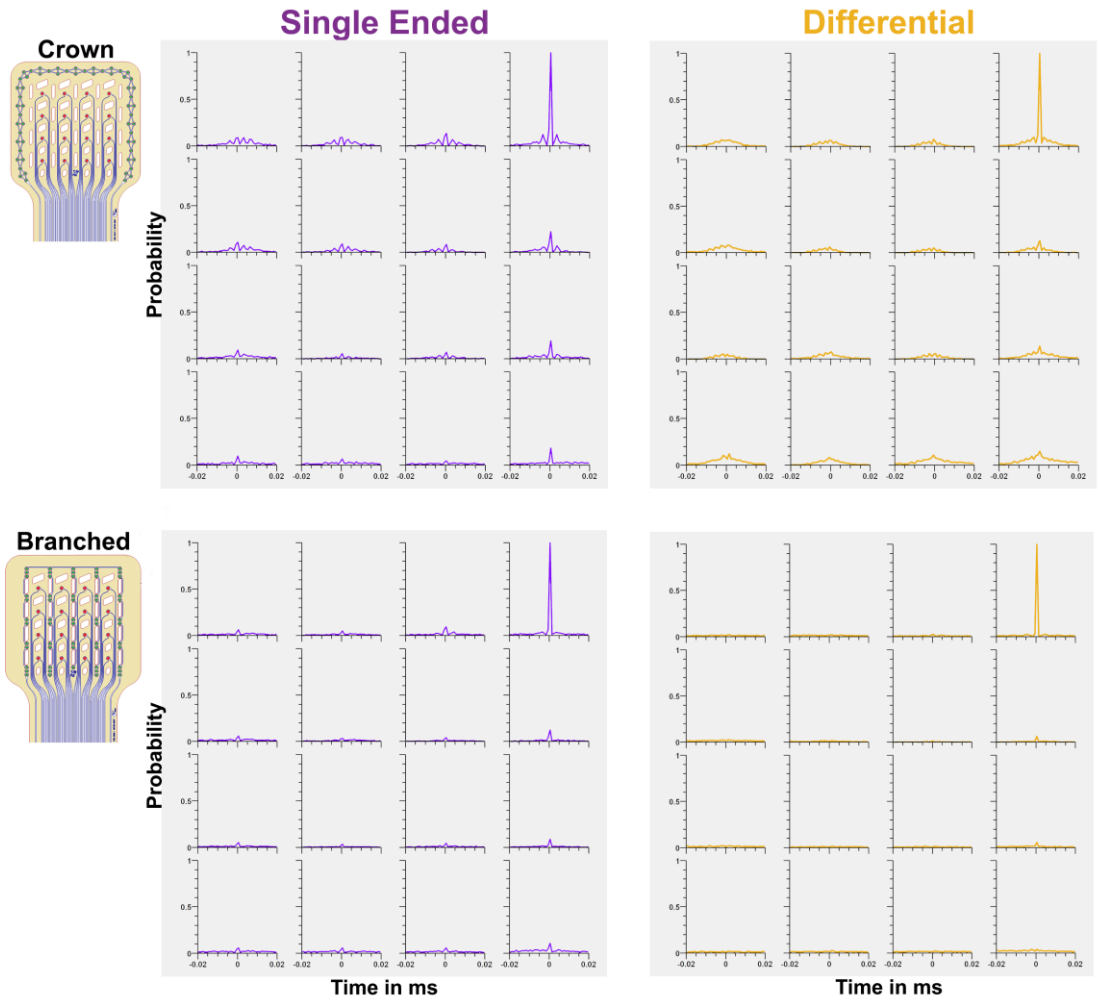

Figure 24 Cross-correlograms of the detected spike events using the spiking activity of the top right electrode as the reference variable for the calculation. Data belong to large electrodes of the MuSA (300 s of spontaneous activity recorded on implant day) and are displayed following their arrangement over the rat cortex. Results obtained from both configurations and reference designs were compared.

The spatial selectivity improvement associated with the differential configuration was corroborated by the comparison between the coherence maps of the single-ended and differential data (Figure 25). A general decrease of the coherence values

over the whole analyzed frequency range (200–6000 Hz) was attributed to the switch from a single-ended to a differential configuration. In line with the previous analysis, the branched reference, with respect to the crown reference, seemed to have a more powerful effect in lowering the signal coherence of neighboring electrodes.

Notably, the column behavior—discussed in the previous section on crosstalk—persisted also when using a differential configuration. Indeed, as reported in the coherence maps of differential data (Figure 25), only the electrodes that had closely routed tracks or ending at the same row of pads interfacing the nanostrip connector continued to show higher correlated signals. This result confirmed the identification of crosstalk as the cause of detecting redundant information from different electrodes, which had no apparent spatial correlation over the cortex.

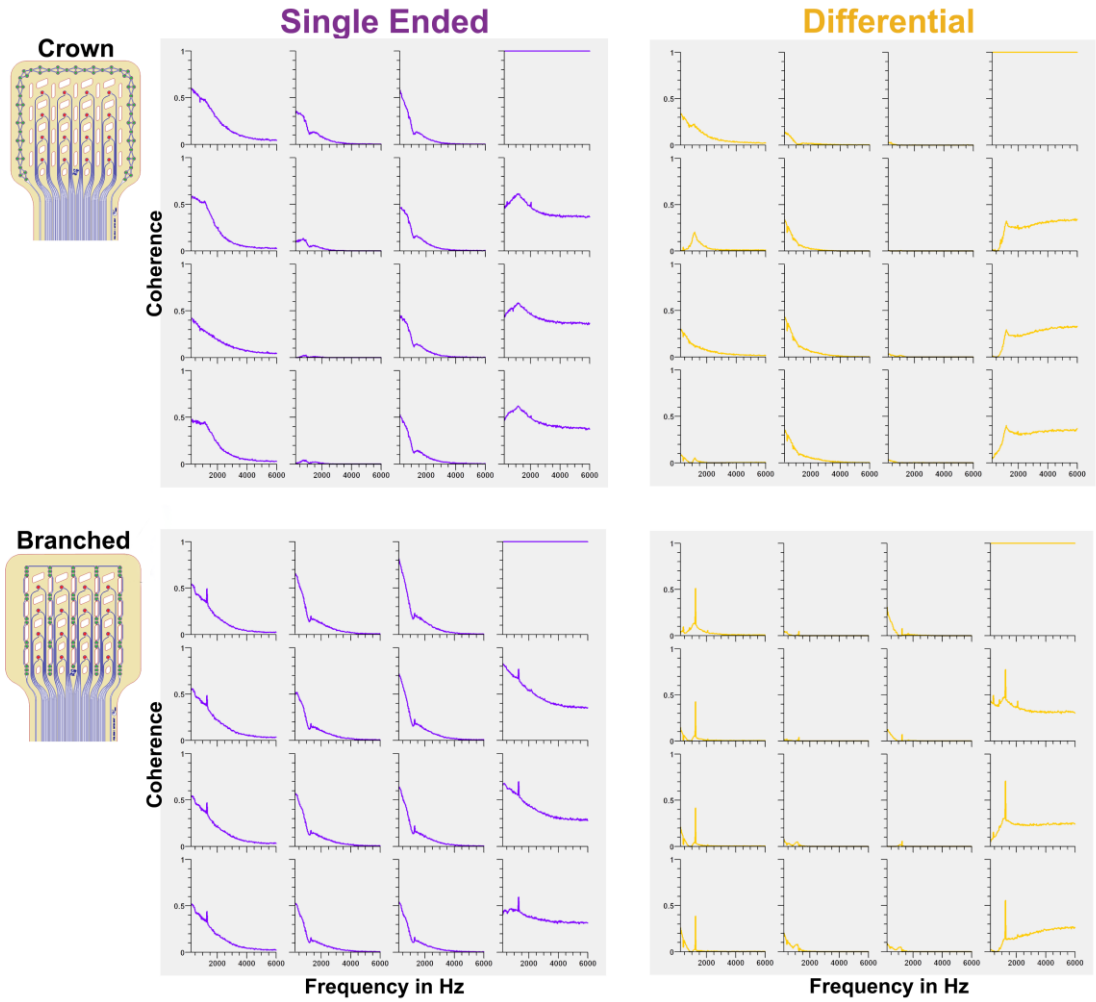

Figure 25 Coherence maps using the top right electrode as the reference variable for the calculation performed in the 200–6000 Hz frequency range. Data belong to large electrodes of the MuSA (300 s of spontaneous activity recorded on implant day) and are displayed following their arrangement over the rat cortex. Results obtained from both configurations and reference designs were compared.

In summary, we found that, when dealing with multi-unit activity signals, using a differential referencing mode could improve the spatial resolution of high-frequency recordings. Moreover, when comparing different reference designs, an arrangement intermingled with the recording sites enabled more efficient suppression of the redundant information caught by submillimeter-spaced electrodes. These results were found also when analyzing the performance of the small electrodes (10 μm, data not shown) and were consistent in all rats.

Chapter 2:

Human μECoG Recordings

ECoG is routinely used during brain tumor resection as a tool for localizing specific brain regions (e.g., the central sulcus as the prominent landmark separating the primary motor cortex from the primary somatosensory cortex), and for monitoring potential epileptic seizures during surgery [115–118]. Moreover, as maximizing the extent of glioma resection is associated with survival benefits for both low- and high-grade gliomas [119], the possibility of finely delineating tumor borders together with epileptic foci through neural correlates would allow remarkable progress in this crucial surgical compromise. From one aspect, more extensive surgical resection extends life expectancy. On the other hand, it is extremely important to preserve functional sites to avoid permanent deficits [120]. Unfortunately, the lack of spatial selectivity of gold-standard devices (from 1 cm to 4 mm) renders them an inadequate candidate for these purposes. Moreover, taking into account neuroprosthetic applications as well, the stiffness and dimension of such ECoG grids causes major complications during chronic evaluations (e.g., tissue damage and recording failure) by limiting the tolerability of the implants [61, 81]. Certainly, technological failures and biological reactions to implanted devices can be considered the primary barrier preventing neural interfaces from reaching their full potential as reading and rewriting neural tools [30]. Although current technologies have enabled great achievements in the past decades [2], the complexity of brain functions requires ceaseless efforts to elucidate still unknown neural processes.

To address the root causes, the ultra-conformable MuSA [29] was fabricated with the intent of first assessing its mechanical compliance with soft tissues and electrophysiological performances in the long-term using rat models, and eventually, to transfer the technology to humans. Such devices—being ultra-flexible and with miniaturized dimensions—represent a promising deal between invasiveness and the spatiotemporal resolution of the acquired signals. Indeed, the idea behind targeting specific brain regions with high-density microgrids is that a more comprehensive representation of complex neural dynamics could be achieved [121, 122].

Following this approach, after an in-depth investigation of rat models, the µECoG array was tested on one human subject undergoing awake neurosurgery for tumor resection. The device was used intraoperatively (Figure 26) with the main goal of exploring neural correlates of speech processing at the submillimeter scale. Accordingly, the µECoG was placed subdurally over the speech arrest area (evoked by direct cortical stimulation) and the patient was asked to perform a naming task (Figure 38 in the Experimental Section) [123, 124].

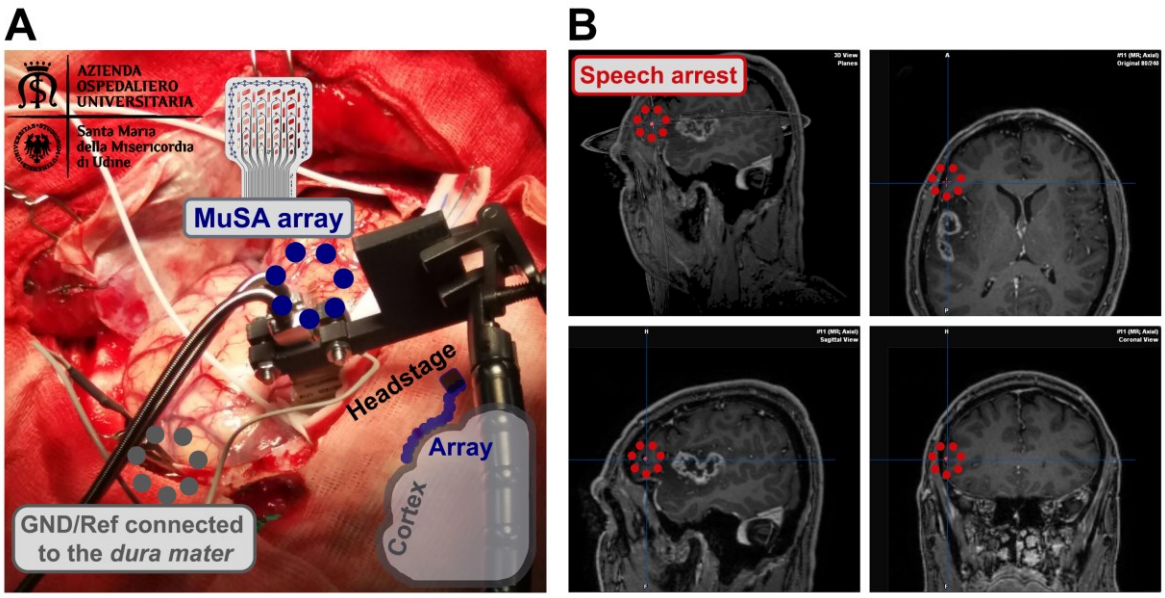

Figure 26 (A) Picture of the MuSA placed over the patient cortex during the intraoperative recording. (B) Snapshot from the neuronavigation system showing the speech arrest area—and thus the location of the µECoG array—superimposed on the patient's magnetic resonance imaging (MRI) scan. Different brain sections are displayed (clockwise from the top left: 3D view, horizontal plane, coronal plane, and sagittal plane).

As expected from the investigations on rat models, the array proved to perfectly adapt to the human cortex in a glove-like manner, making array positioning faster and easier for the neurosurgeon. Indeed, thanks to elasto-capillary forces, strong contact with the neural tissue was established without requiring additional pressure or adhesive strategies. Consequently, environmental noise caused by medical devices in the surgery room was substantially constrained, determining an immediate positive effect on the quality of the neural signal (Figure 27A). On the contrary, using standard ECoG arrays often requires repositioning of the grid over the cortex because of weak contact between the electrodes and the tissue, which translates into poor signal quality, need for external pressure, and wasted time.

On the different electrode geometries, recordings collected with the small electrodes (10 µm) of the MuSA were less stable and reliable (Figure 27A) when compared to

the performance obtained with the large electrodes (100 µm). Indeed, consistent with the outcomes obtained from acute implants in rats, the high-frequency noise band of smaller geometries, possibly due to lower wettability, was evidently wider than that of the larger geometries (Figure 27B). Hence, only the signals recorded with large electrodes were considered for further investigations.

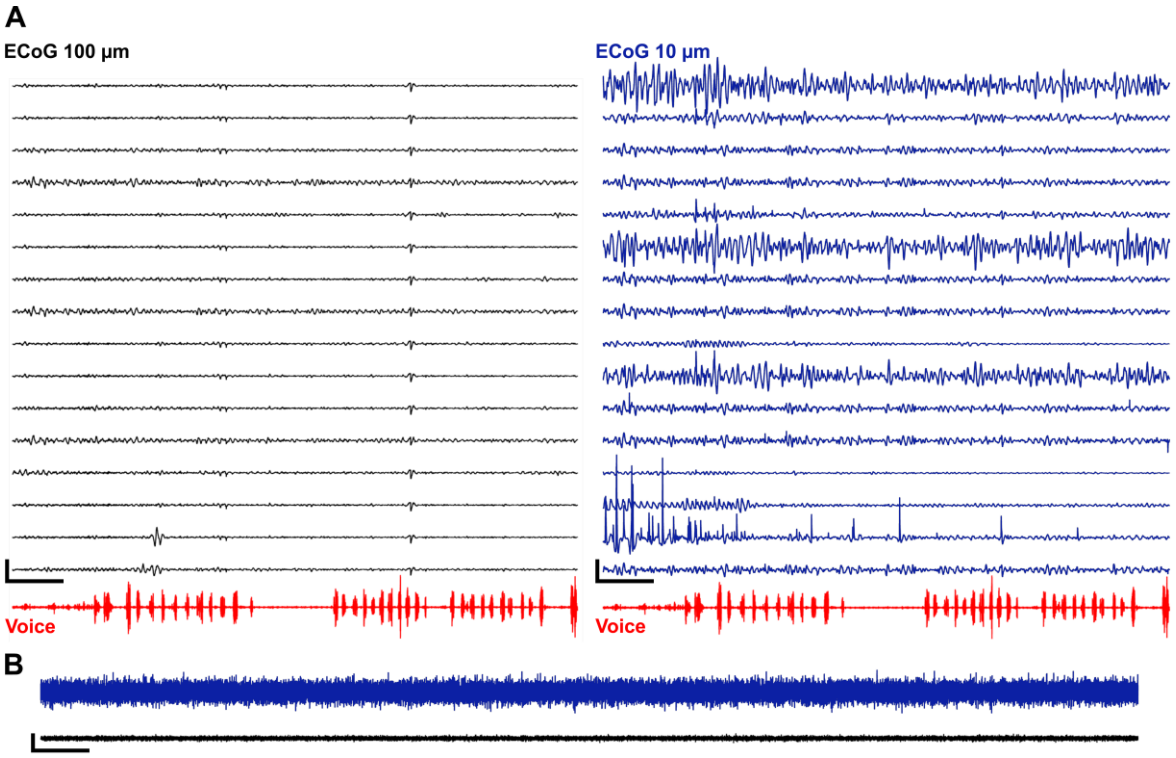

Figure 27 (A) Band-pass–filtered traces (3–300 Hz) recorded intraoperatively with the MuSA aligned with the subject's voice. Black indicates the large electrodes; blue indicates the small electrodes. Scale bars measure 2 mV – 10 s. (B) Representative high-pass filtered traces (200 Hz) of one small electrode (blue) and one large electrode (black). Scale bars measure 100 µV – 1 s.

The spatiotemporal relationships between neural signals were explored focusing on the search for relevant speech-related activities assuming that diverse time–frequency dynamics could be finely described at the submillimeter scale. In this regard, neural continuous traces were filtered in different frequency ranges, allowing thorough visual inspection. Specifically, attention was drawn to canonical ECoG frequency bands such as beta (15–30 Hz) and high gamma (70-150 Hz), and to perform the single-trial time–frequency analysis, the data were segmented into trials time-locking the signal to the speech onset. The spectrograms averaged across trials of the high gamma and beta bands are shown in Figure 28 following the electrode arrangement on the array. Based on the power of both frequency bands, it is clear that the µECoG signals recorded with neighboring electrodes (spaced by

750 µm) could provide distinct and spatially coherent representations of the speech production process. In fact, the power associated to the high gamma range emerged prominently in the bottom left portion of the array (Figure 28B) and gradually faded over the distance. Differently, the beta band power (Figure 28A), starting from the top right side of the matrix, was more widespread among different electrodes. Moreover, the two frequency bands were characterized by opposite activation timings: power increase in the beta band occurred right after speech onset, while that related to the high gamma range arose before the subject started speaking.

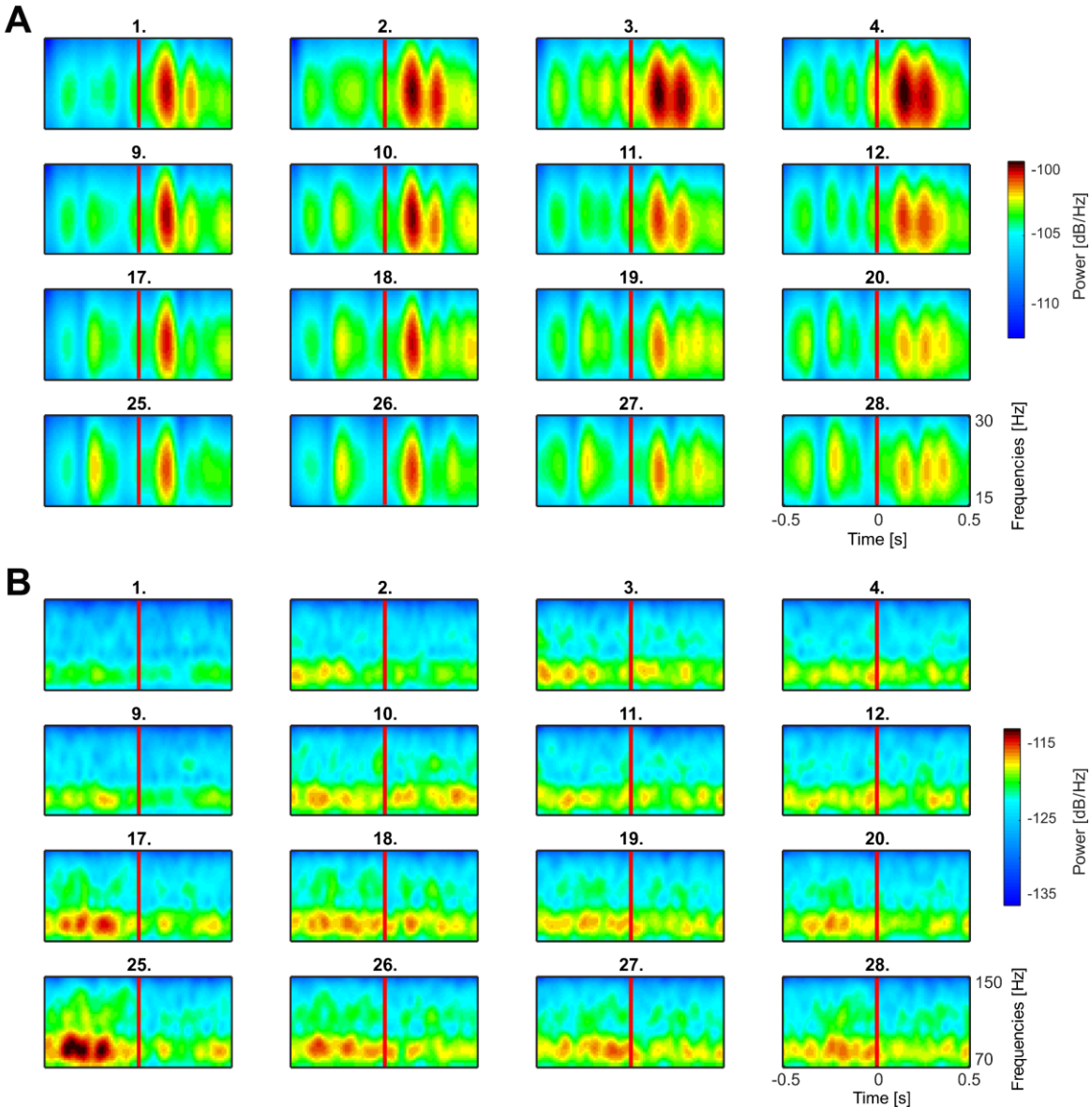

Figure 28 Averaged spectrograms across trials (n = 30) of the large MuSA electrodes calculated in the beta (15–30 Hz, A) and high gamma (70–150 Hz, B) frequency bands. Electrode displacement follows their actual arrangement over the subject cortex. The vertical red line (t = 0) represents the speech onset.

According to the mean power profiles of the three repetitions of the same word (Figure 29), the most active electrodes showed a fast increase and decrease in the high gamma power, anticipating the speech onset (approximately 250 ms before). Such a power profile, being highly similar across trials, can be understood as proof of the temporal coherence attributed to the speech-related high gamma activity. This tendency was less obvious for the beta band, which reported more variable behavior across different trials (data not shown).

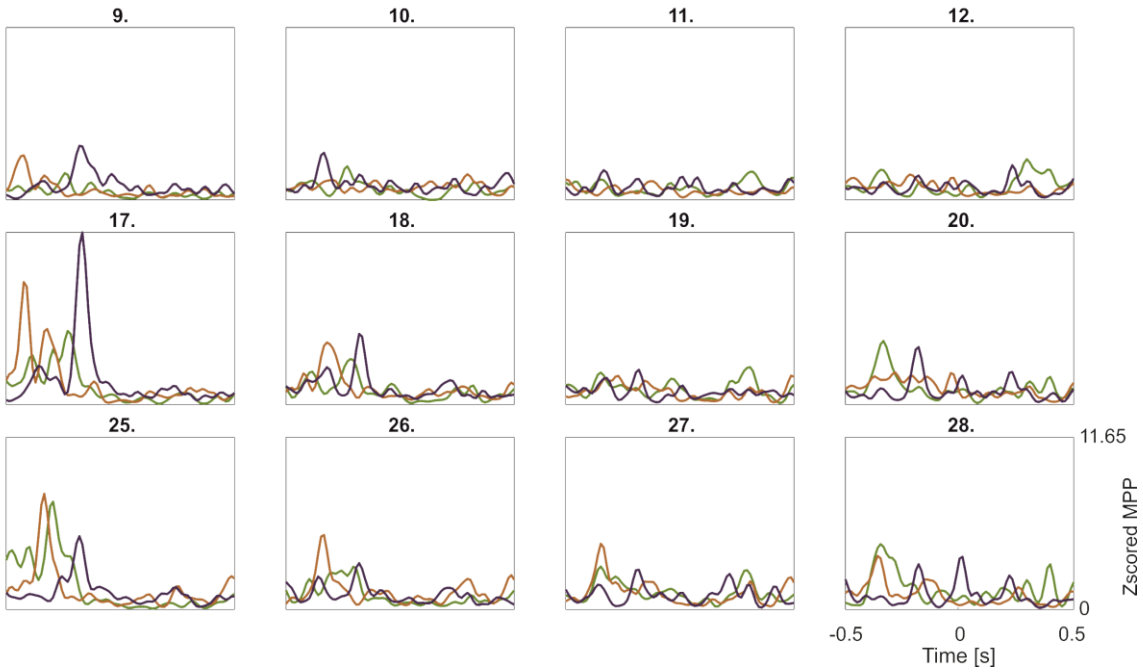

Figure 29 Spectrograms averaged across the frequency range of 70–150 Hz (high gamma band). Some selected channels (the most active ones) are reported following their arrangement over the subject cortex. The three colors represent different trials aligned to the speech onset (t = 0).

In summary, regardless of its small dimension (total active area of 2.25 mm × 2.25 mm), the MuSA could provide valuable information related to the speech production process. Closely spaced electrodes (750 µm) detected neural signals with diverse and well-defined spatiotemporal dynamics, demonstrating that non-redundant information was acquired. It is important to note that one electrode of a standard ECoG grid covers the entire active area of the MuSA; hence, by using standard recording tools, much neural information might have been lost. Due to the volume conduction phenomena, acquiring the signal with just one larger electrode provides an averaged representation of the voltage fluctuations in the underlying cortical layers mostly at the expense of fast oscillations [15]. In this scenario, the spatial specificity of the speech arrest area—verified with the µECoG recordings—might

have been cancelled. On the contrary, the use of submillimeter-spaced electrodes made the preservation of these diverse neural dynamics possible. Interestingly, anticipatory features of speech production were found in the high gamma band, and such powerful signals originating from this brain area could be used to predict when the subject is going to speak with extremely high spatial precision. This perspective could be remarkably useful for BCI applications. Indeed, such neuronal cues could serve to cleverly start speech decoding in patients with major motor impairments, such as paralysis or locked-in syndrome.

Conclusions and Future Perspectives

In this study, it has been shown that, to improve the longevity and tolerability of neural implants, the ultra-conformability of epicortical devices plays a pivotal role in high-quality recordings. Indeed, we demonstrated that, when taking advantage of arrays able to establish strong contact with the neural tissue but that at the same time exert minimal pressure on the cortex, high-frequency recordings (multi-unit activity) from the surface of the rat brain can be sustained for long periods (12 weeks and possibly beyond). Moreover, histological evaluations proved that cortical depression caused by non-conformable arrays can be avoided by using devices whose mechanical properties are specifically tuned for the targeted brain.

When aiming to build an efficient and reliable neural interface, the undeniable positive effects of conformable substrates should be accompanied by equally stable electrode materials. In this investigation, several alternatives—from traditional metals to novel carbon applications—were evaluated in terms of recording performance and ability to withstand the biological environment. All the tested materials (Pt, IrOx, PEDOT/PSS, and GC) were demonstrated to be good candidates for long-term neural interface development because of the quality of the recorded signal and the absence of corrosion/delamination signs. More precisely, PEDOT/PSS coatings provided evident advantages for miniaturized electrodes by limiting the background noise level and in turn improving the high-frequency detection during acute recordings. This expected outcome can be ascribed to the well-known ability of PEDOT/PSS to lower electrode impedance and its mixed conduction properties (ionic and electronic). In chronic scenarios, due to the decreased impedance in miniaturized electrodes over time, the background noise level of large and small electrodes became comparable also in the case of metal electrodes (Pt and IrOx), making the deposition of PEDOT/PSS superfluous.

Miniaturization of the recording sites was necessary for the aim of this study, which proposes the use of high-density microelectrode arrays as a promising solution for both clinical and basic investigations in human neurosciences. Accordingly, spatially resolved high-frequency signals recorded with ultra-conformable μECoG devices were investigated during chronic implants in rats, leading to two major results. First, we demonstrated that the spatial selectivity of the detected multi-unit activity can be

improved using a reference electrode intermingled with the recording sites in a differential recording mode. Second, undesired crosstalk between closely routed tracks and closely spaced pads at the connector level was observed. To address this issue, preliminary experiments were conducted to quantify the degree of this phenomenon *in vitro*. Concurrently, the ways in which crosstalk can affect the recorded signal were evaluated on the data collected *in vivo*. This effect, as well as the contribution of the passive electrical properties of the neuronal target tissue (load impedance), will be investigated in a more comprehensive study to derive a model of the transmission line including all the different components. This approach could help in the design of microelectrode arrays according to its spatial limits and with a minimum level of crosstalk for high-quality µECoG recordings.

Finally, fulfilling the translational purpose of this investigation, the ultra-conformable MuSA array was tested on one human subject undergoing awake neurosurgery to investigate neural correlates of speech processing. As expected from the rat experiments results, the array adapted perfectly to the human cortex in a glove-like manner, requiring no additional pressure or adhesive strategy. High-quality recordings were obtained mainly due to the strong contact between the electrodes and the neural tissue. Regardless of its small dimension, the µECoG array provided valuable information related to the speech production process recorded from the frontal cortical region for speech production. Closely spaced electrodes (750 µm) detected neural signals with diverse and well-defined spatiotemporal dynamics, demonstrating that non-redundant information was acquired. Interestingly, anticipatory features of speech production were found in the high gamma band, and such powerful signals originating from this brain area could be used to predict when the subject is going to speak with extremely high spatial precision. Detecting speech preparation could bring remarkable progress in speech recognition system development. Indeed, such neuronal cues could be employed as the trigger for starting the decoding when an explicit alignment is not possible (e.g., in covert speech).

Finally, a bigger version of the MuSA was designed to further investigate neural processes with a device that better fits the dimensions of the human brain (Figure 30).

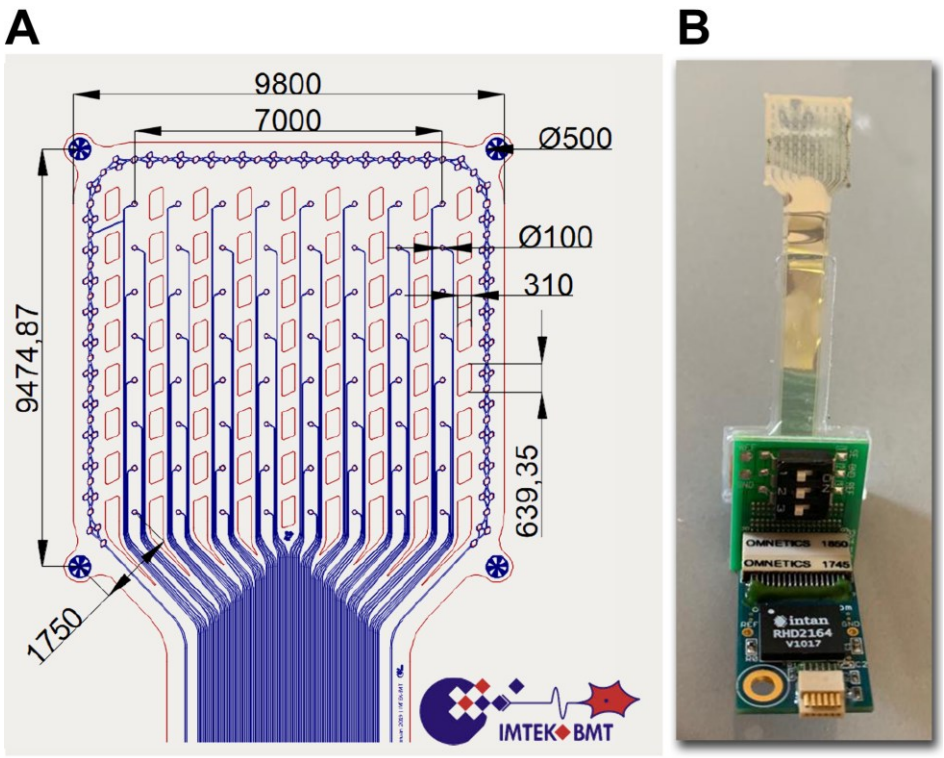

Figure 30 (A) Schematic of the 64-channel MuSA for human applications. Dimension labels are reported in µm (8 x 8 layout, electrodes diameter of 100 µm, electrodes pitch of 1mm). (B) Picture of the array connected to the headstage amplifier of the recording system (Intan Technologies LLC, USA) through a custom-made printable circuit board.

The recording site density was maintained by increasing the number of the contacts (from 16 to 64 channels), and the electrode diameter was set to 100 µm. A reference-on-the-array was included, and accordingly, a custom-made printable circuit board was fabricated to easily switch from the single-ended configuration (using the patient's dura mater as the ground electrode) to the differential configuration (thus exploiting the reference-on-the-array). Four targets were placed on the array corners to precisely localize the device position over the cortex with the neuronavigation system used in the surgery room.

The 64-channel MuSA will be used intraoperatively in the future for speech decoding purposes as well as for tumor border identification by taking advantage of high-quality µECoG signals.

Experimental Section

1. Fabrication of Ultra-conformable µECoG Arrays

The ultra-conformable µECoG devices used in this study were fabricated by Maria Vomero and Maria Francisca Porto Cruz in the cleanroom facilities of IMTEK (Institut für Mikrosystemtechnik), University of Freiburg (RSC, class 100).

1.1 MuSA Array

The MuSA [29] were fabricated using standard microlithography techniques shown in Figure 31A.

First, U-Varnish-S PI (UBE Industries Ltd., Japan) was spun on silicon wafers (at 3000, 4500, and 9000 rpm for achieving thicknesses of 6, 4, and 2 µm, respectively). Then, tracks, connection pads, and recording sites were patterned with the high-resolution image reversal photoresist AZ 5214E (MicroChemicals GmbH, Germany). O_2 plasma (80 W, Plasma System 300-E, PVA TePla, Germany) was used as an adhesion promoter for the metal, which was subsequently evaporated onto each wafer (300 nm Pt, Univex 500 Electron-Beam Evaporator, Leybold GmbH, Germany). Lift-off to remove the excess metal was done in acetone; after it was completed, the same image reversal photoresist was used to pattern the recording sites of the devices that were to be coated with IrOx. Consequently, 100 nm iridium followed by 700 nm IrOx (obtained by introducing O_2 in the sputtering chamber of the Univex 500, Leybold GmbH) were sputtered on the devices and the lift-off in acetone was repeated. Again, O_2 plasma was used to activate the surface of the wafers before a second PI layer was spun onto all of them. The positive photoresist AZ 9260 (MicroChemicals GmbH) was used as masking layer for the opening of the contact pads and electrode sites and for setting the device outlines. PI was finally etched using O_2 plasma in a reactive ion etching (RIE) machine (STS Multiplex ICP, SPTS Technologies, United Kingdom) with a multi-step protocol (200 W first and 100 W after, with time varying with PI thickness). Finally, the photoresist was stripped off in an acetone bath and the devices were mechanically peeled off the wafers using flat tweezers.

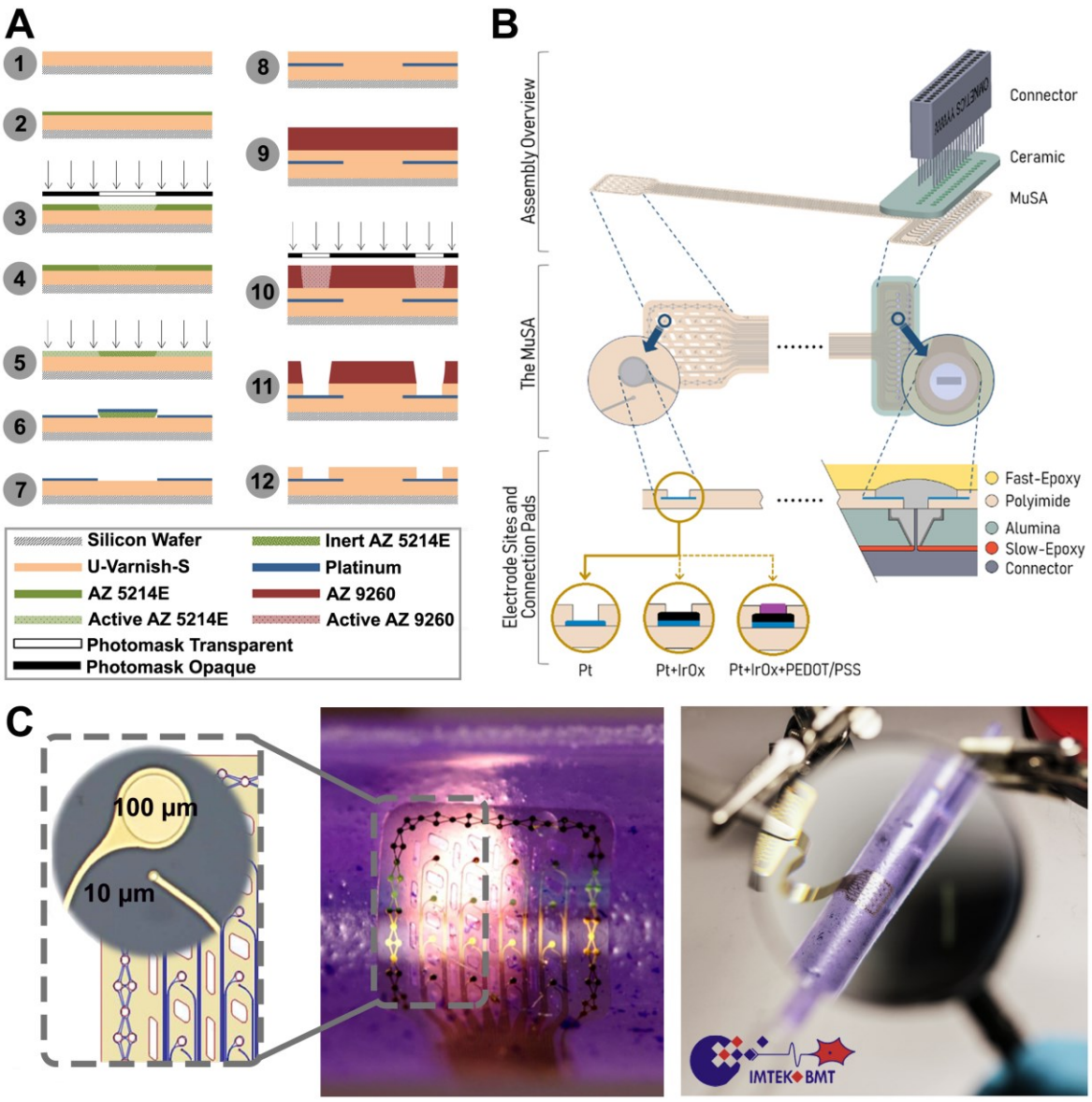

Figure 31 (A) Fabrication protocol: (1) U-Varnish-S spincoating (4 µm); (2) AZ 5214E spincoating (1.4 µm); (3) exposure; (4) reversal bake; (5) flood exposure; (6) Pt evaporation (300 nm); (7) life-off; (8) U-Varnish-S spincoating (4 µm); (9) AZ 9260 spincoating (14 µm); (10) exposure; (11) PI etching using RIE; (12) AZ 9260 stripping. (B) Schematic of the assembly of a 32-channel MuSA device to a fully custom-made ceramic board on which an Omnetics connector was soldered. Different versions of the MuSA have different electrode materials: Pt, IrOx, or PEDOT/PSS. (C) Schematic of a portion of the MuSA showing the electrode diameters (10 µm and 100 µm) and pictures of the array wrapped around a pipet of about 8-mm diameter.

To interface the recording system, the MuSA devices were connected to a male Omnetics connector (NPD-36-DD-GS, Omnetics Connector Corporation, USA) via a metallized ceramic board. The assembly consisted of the following steps: (1) cutting and pressing HTCC (high temperature co-fired ceramic) tape (44000, ESL ElectroScience, USA) at 27 MPa; (2) laser-patterning the holes (through which the Omnetics connector pins are inserted) and board outline; (3) organic burnout at

550°C and sintering at 1500°C; (4) applying AgPd (silver–palladium) paste to the front of the holes and removing the excess from the back to ensure homogeneous coverage of their inner walls; (5) firing at 850°C and grinding both the front and back sides. Once the connectors were soldered to one side of the ceramic boards, the MuSA devices were soldered on the other side, and two-component epoxy was used to protect and insulate the solder joints.

As shown in Figure 31C, the resulting arrays had recording electrodes of two sizes: 10 and 100 µm, distributed in four rows of four electrodes each (pitch of 750 µm). Large and small electrodes were separated by a 45-µm gap with the aim of recording from the same anatomical area. Pt and IrOx were used as the device metallization materials, and two versions of the reference electrode on the array (58 pads with a diameter of 100 µm) were fabricated: a crown reference surrounding the recording site area and a branched reference whose pads were intermingled with the recording electrodes (Figure 32). PI was patterned in a “breathable” (incorporating holes) shape, and its thickness was set to 8 µm for the neural recordings and also to 4 and 12 µm for histological evaluations.

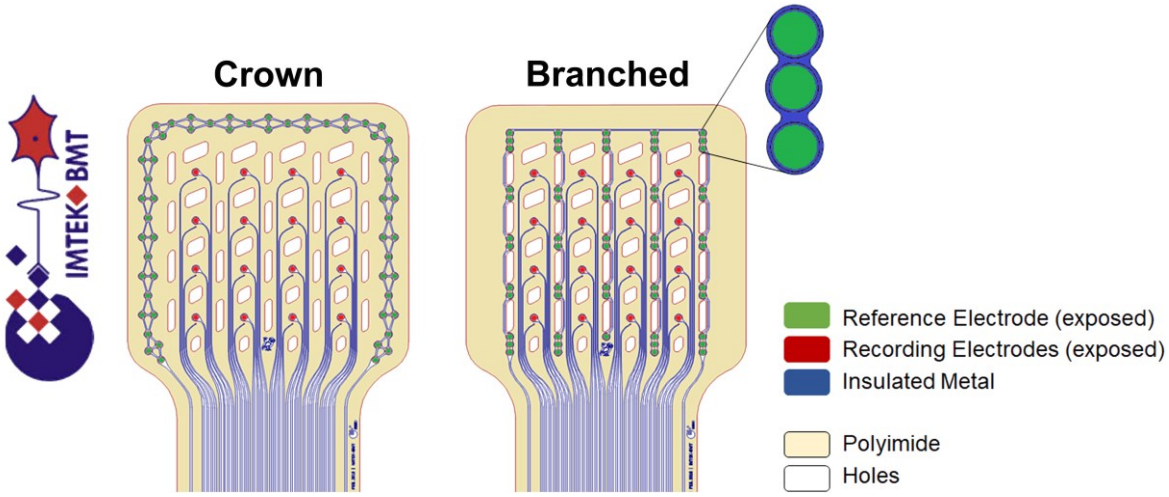

Figure 32 Sketches of the MuSA showing the two different reference electrode designs (green pads): a crown reference surrounding the recording site area (left) and a branched reference whose pads were intermingled with the recording electrodes (right).

1.2 CaLEAF Array

The CaLEAF arrays [79] were fabricated using a microelectromechanical systems (MEMS) protocol [78] following the steps shown in Figure 33A.

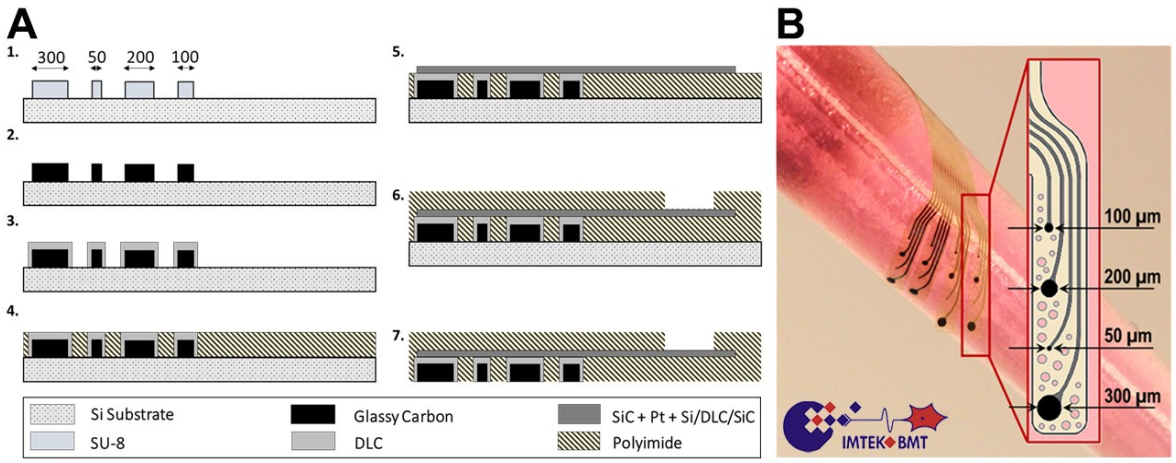

Figure 33 (A) The MEMS process used to fabricate the ultra-conformable PI-based ECoG devices with GC electrodes: (1) Lithographically patterned SU-8 disks with diameters of 50, 100, 200, and 300 µm and height of 13 µm. (2) Pyrolysis of SU-8 structures (1000°C) to obtain GC electrodes. (3) PECVD (plasma-enhanced chemical vapor deposition) of 50 nm DLC (diamond-like carbon) onto GC electrodes. (4) First layer of PI (4 µm), patterned to open the vias to the GC electrodes. (5) PECVD of 50 nm SiC (silicon carbide) on the tracks of the devices, followed by evaporated Pt (300 nm) and 50 nm Si/DLC/SiC. (6) Second layer of PI (4 µm), patterned to access the metal bump pads. (7) Buffered oxide etch (BOE) for releasing the devices from the silicon wafer. (B) Picture of a CaLEAF array wrapped around a pipet of about 8 mm diameter. The inset shows one of the four PI "breathable" fingers with the different-diameter GC electrodes. (From Vomero M. *et al.*, 2018)

As the first step, SU-8 3010 (MicroChem, USA) was spun on a silicon wafer and photolithographically patterned in 4 × 4 arrays of disk-shaped structures with diameters of 50, 100, 200, and 300 µm and height of 13 µm. They were then pyrolyzed in a furnace (PEO-601, ATV-Technologie GmbH, Germany) at 1000°C in N_2 atmosphere (60 min), creating the GC recording sites. The electrodes were then coated with 50 nm methane-based PECVD DLC (plasma-enhanced chemical vapor deposition of diamond-like carbon). PI (U-Varnish, UBE Industries Ltd.) was spin-coated onto the substrate and cured at 450°C to 4-µm thickness, and a second photolithography step was implemented to define openings on the backside of the carbon electrodes. Then, a third photolithography step (AZ 5214E, MicroChemicals GmbH) was performed to define the tracks for the electrical routing and a 50-nm layer of silicon carbide (SiC) was deposited, followed by 300 nm Pt and 50 nm silicon (Si), DLC, and SiC (PECVD). A second layer of PI was spun onto the tracks (4 µm)

for insulation and patterned to access the interconnection sites. Finally, the devices were released from the silicon wafer through a buffered oxide etching process.
To interface the recording system, the array was inserted into a zero insertion force (ZIF) connector on a custom-made printed circuit board (PCB).
As shown in Figure 33B, the obtained design was a 4 × 4 array with electrode diameters of 50, 100, 200, and 300 μm, separated by 400 μm. PI was patterned in a finger-like and “breathable” (incorporating holes) shape, and its thickness was set to 8 μm.

2. PEDOT/PSS Deposition

PEDOT/PSS was deposited on a subset of the MuSA devices by Maria Francisca Porto Cruz in the facilities of IMTEK following a previously described electrochemical protocol [127]. To improve the stability of the coating, only IrOx electrodes were coated [128]. Prior to the polymer deposition, all probes were immersed in PBS (0.01 M) and electrochemically cleaned by cyclic voltammetry (from -0.6 V to 0.9 V, 100 mV/s, 10 scans) to obtain a chemically well-defined IrOx surface. Subsequently, the probes were transferred to an aqueous electrolyte containing the monomer EDOT (0.01 M) and the dopant poly(sodium 4-styrene sulfonate) (NaPSS, 5 mg/ml). PEDOT/PSS coatings were potentiostatically deposited with an Autolab 302N potentiostat (Metrohm Autolab, Germany) in a three-electrode configuration (with an Ag/AgCl [silver/silver chloride] reference electrode and a large stainless steel counter electrode) at 0.9 V potential and using a polymerization charge density of 300 mC/cm^2.

When required by the aims of the study, the GC electrodes of the CaLEAF array were similarly coated with the CP by Stefano Carli in the facilities of Italian Institute of Technology (IIT). PEDOT/PSS was prepared by anodic electrodeposition from a solution of EDOT (0.02 M) and NaPSS (0.1 M) in water. The electrochemical deposition was carried out in potentiodynamic mode in the potential range of 0–0.95 V and with a scan rate of 100 mV/s (20 cycles per electrode). A Reference 600 potentiostat (Gamry Instruments, USA) connected to a three-electrode electrochemical cell (with an Ag/AgCl reference electrode and a Pt wire counter electrode) was used for the electrodeposition.

3. In vivo Electrochemical Impedance Spectroscopy

In vivo impedances of chronically implanted MuSA electrodes were carried out using a potentiostat/galvanostat (Reference 600, Gamry Instruments) in a two-electrode setup. Each electrode was referenced to a low-impedance stainless steel screw inserted into the rat skull, and measurements were collected every week for the whole duration of the implants (up to 12 weeks). During the impedance measurements, a sine wave (100 mV RMS [root-mean-square] amplitude) was

imposed onto the open circuit potential while varying the frequency from 1 to 100 kHz.

4. Impedance Spatial Sweep for Crosstalk Assessment

To understand how impedance between tracks changes with the distance between them, a spatial sweep was performed on the MuSA devices based on electrochemical impedance spectroscopy using an Autolab PGSTAT (Metrohm Autolab BV, the Netherlands). The leftmost track (assuming the device stands vertically with the array oriented upwards and the open contacts facing the front) was used as the counter, and the remaining 31 tracks were set as the working electrode, one at the time (two-electrode setup). To investigate the influence of PBS (pH 7.4) on the coupling between the lines, the device was bent concave, as depicted in Figure 34, so that only the track body remained immersed in PBS as a means of ensuring that the electrode–electrolyte interface was excluded from the measurements. The samples were immersed 2 hours before the start of the experiment to minimize drifts caused by water uptake of the PI. As high impedances were expected, a Faraday cage was used. The AC excitation voltage was set to 100 mV at open circuit potential (OCP) and its frequency swept from 100 Hz to 100 kHz.

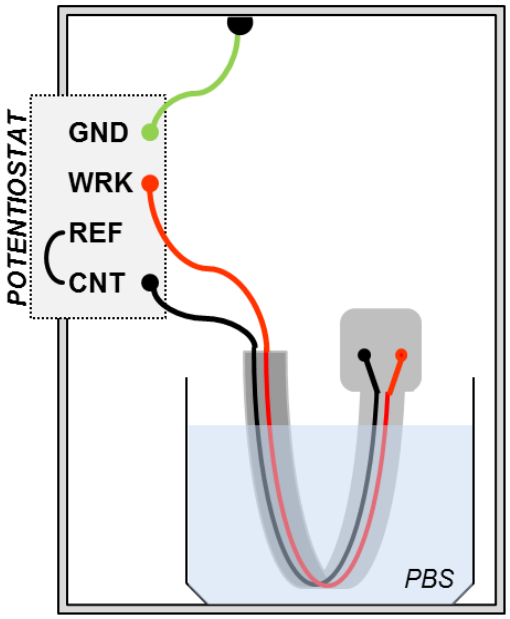

Figure 34 Electrochemical experimental setup used for the impedance spectroscopy measurements. GND, ground; WRK, working; REF, reference; CNT, counter electrode. (Adapted from Cruz M. F. P. *et al.*, 2019)

5. Surgical Procedures for Acute and Chronic Implants in Rat Models

The ultra-conformable µECoG devices were tested *in vivo* in rat models (adult male Long–Evans rats, 400–500 g). The experimental plan was designed in compliance with the guidelines established by the European Communities Council (Directive 2010/63/EU, Italian Legislative Decree n. 26, 4/3/2014) and the protocol was approved by the ethics committee for animal research of the University of Ferrara and by the Italian Ministry of Health (authorization n 332/2015-PR). Specifically, five rats were acutely implanted with CaLEAF arrays and 16 rats were used for the MuSA experiments: eight for acute recordings and eight for chronic recordings.

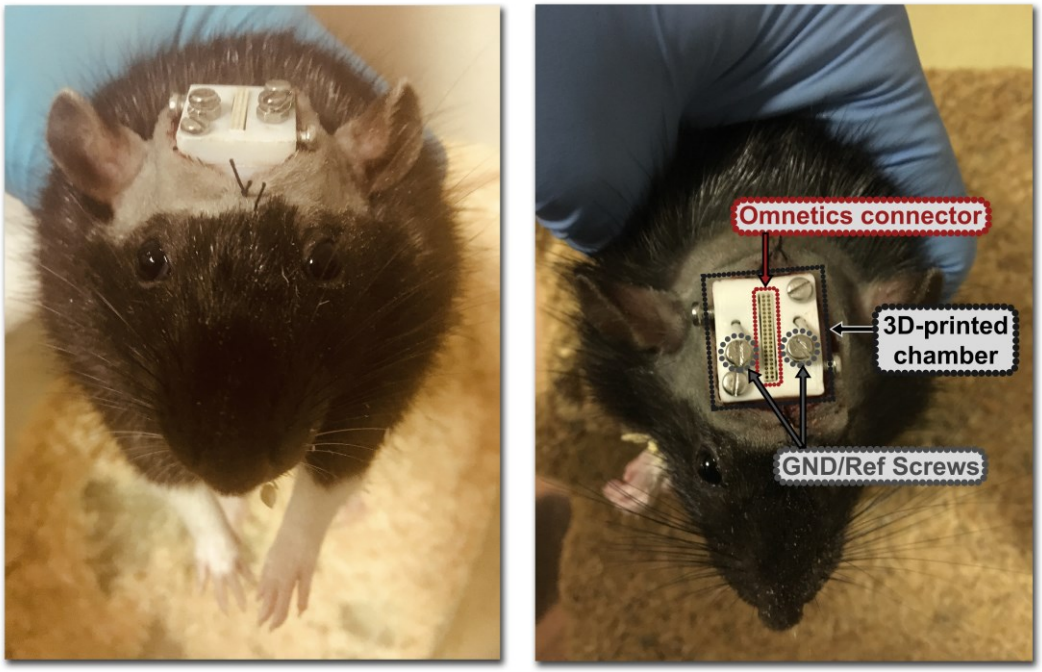

Figure 35 Pictures of a chronically implanted rat. Labels refer to the implanted components and the connections.

On implantation day, the rats were anesthetized with a mixture of Zoletil (Virbac, France; 30 mg/kg) and xylazine (Bayer, Germany; 5 mg/kg) administered intraperitoneally (i.p.). For the duration of the procedure, the depth of anesthesia was monitored by testing the absence of hind limb withdrawal reflex and was maintained by additional intramuscular (i.m.) doses of anesthetic. The anesthetized animals were then placed in a stereotaxic apparatus (David Kopf Instruments, USA) equipped with ear bars (Model 957 for small animals) and a ≈2-cm long incision was made along the midline of the cranium. The underlying muscle and connective

tissue were retracted to expose the skull, and a craniotomy (≈6 × 6 mm^2) was made in the parietal bone to expose the somatosensory cortex identified according to vascular landmarks and stereotaxic coordinates [87]. Sterile saline solution was applied while drilling to avoid any local heating and to keep the bone surface clean. The ultra-conformable µECoG devices were then placed over the dura mater in the primary somatosensory barrel field (S1BF).

When performing chronic implants, the surface of the implanted tissue was protected using Kwik-Sil silicone polymer (World Precision Instruments Inc., USA). To hold the implant in place, five stainless steel bone screws were inserted into the skull (one also serving as the reference/ground electrode), and the connector of the array was fixed to a custom-made chamber fabricated with a 3D printer (Voxel8 Inc., USA). Finally, the implant was cemented to the skull using dental acrylic (Jet Repair Acrylic, Lang Dental Manufacturing, USA), and the skin was sutured around the chamber and cement (Figure 35 and Figure 36, type C).

6. Histology and Rat Cortex Depression Evaluation

Histological techniques were used to assess the cortex depression caused by the μECoG chronic implants.

In accordance with the surgical procedures described in the previous section, eight adult Long–Evans rats (400–500 g) were implanted with devices with differing PI thickness (MuSA 4, 8, and 12 μm) or PI fenestration hole density (HD, 12-μm thick arrays with highly distributed fenestration; PD, 12-μm thick array with poorly distributed fenestration). As a control for assessing the connectors' influence on cortex depression, the implants performed to compare the 12- and 8-μm arrays were also carried out with (C) and without connectors (NC), thus avoiding the use of dental acrylic and screws (Figure 36).

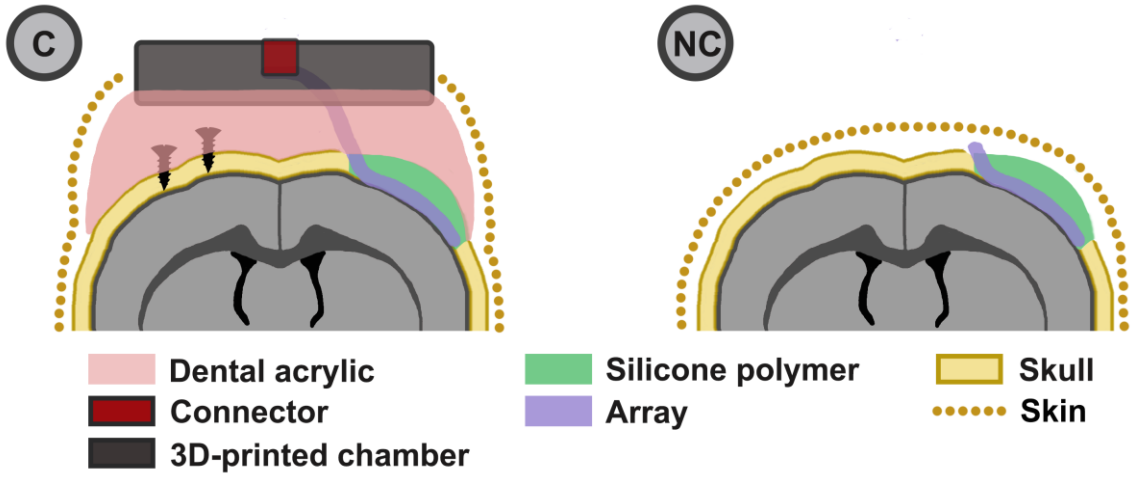

Figure 36 Sketch (not to scale) displaying how the implants with connectors (C, also shown in Figure 35) and without connectors (NC) were carried out.

After six weeks from the implant day, deep anesthesia was maintained for the animals, which were transcardially perfused with 300 ml 0.9% saline solution at room temperature, followed by 500 ml cold fixative solution of 2.0% paraformaldehyde, 1.25% glutaraldehyde, and 2.0% sucrose (all from VWR, USA), prepared in 500 ml 0.1 M sodium PBS (pH 7.4). The brains were then removed, post-fixed overnight at 4°C, and placed in a 30% sucrose-buffered solution until they sank. Then, they were frozen, and 50-μm thick coronal sections were cut using a sliding microtome (SM2000 R; Leica Microsystems, Canada).

To investigate the mechanical compliance of the devices to the tissue, the brain sections were then stained with thionin (Sigma Aldrich, USA) and viewed under

bright field illumination with an Olympus BX51 microscope (Olympus, USA) coupled with a CX9000 color video camera (MicroBrightField, USA) and the Neurolucida system (MicroBrightField). Thionin-stained sections were acquired at 125× magnification and the images were post-processed and analyzed using ImageJ software (developed at the National Institutes of Health, USA). An ImageJ plugin was used to draw a grid over the acquired images of the brain sections. The cortex depression was then calculated as the difference (D = Lctr - Lexp) between the distance from two fixed points of the control hemisphere (Lctr) and of the implanted hemisphere (Lexp). To cover the entire area below the array, in each brain section, the difference (D) was calculated at three different positions for both hemispheres. At least twelve images were analyzed for each implanted device. The significance of the data was evaluated using two-way analysis of variance (ANOVA), followed by Bonferroni's post hoc test for multi-comparison between the thickness and presence of the connector; one-way ANOVA followed by Bonferroni's post hoc test was used to assess the significance of the data on the density of PI fenestration holes and the comparison between 4- and 8-µm thick MuSA devices.

7. In vivo µECoG Recordings and Sensory Stimulation in Rats

For chronic implants, neural signal recordings from the anesthetized and head-fixed rats were collected after the surgical procedure (day 0) and the following weeks (1–6, and week 12) using a Tucker-Davis Technologies multi-channel recording system 3 (USA) that included: a ZIF-Clip® headstage with unity (1×) gain, RZ2 real-time processor, and PZ2-256 battery-powered preamplifier. To reduce electromagnetic noise, the experimental setup was placed in a Faraday cage. Data were digitized at a sample rate of 12207 samples/s at 18-bit resolution and transferred from the RZ2 processor to computer by fast fiber optic connection.

Two different recording configurations were used: (1) single-ended (the reference and ground pins of the headstage are tied together and connected to a skull screw); and (2) differential (the reference and ground pins are decoupled; the ground pin is tied to a skull screw and the reference pin is connected to the reference electrode on the array). As mentioned earlier, two reference electrode designs on the array were tested (Figure 32). The recording chain and headstage configurations are depicted in Figure 37.

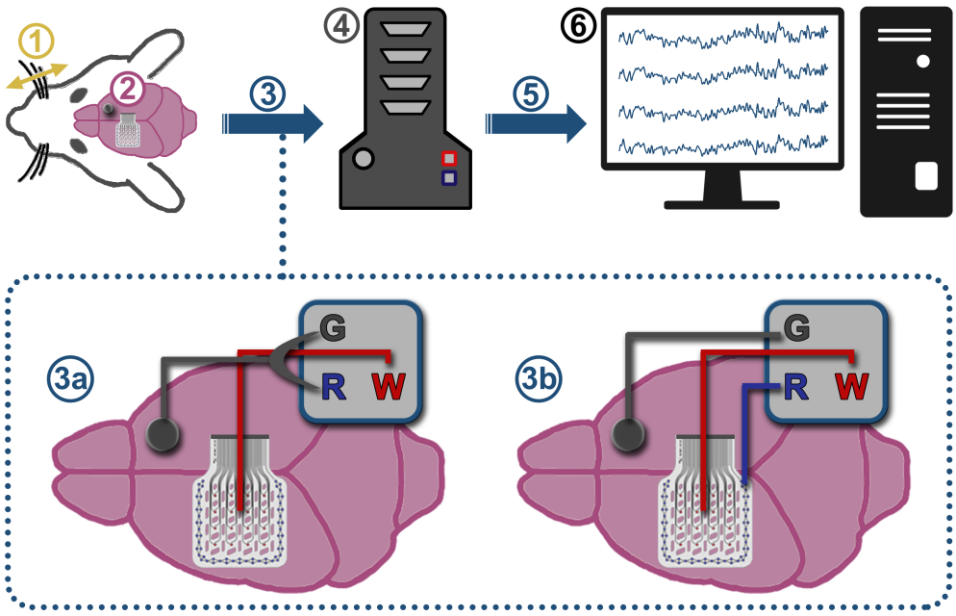

Figure 37 Sketch (not to scale) showing the setup used for the µECoG recordings in rats: (1) Mechanical stimulation of the rat whiskers; (2) Contralateral µECoG recordings from the primary somatosensory cortex; (3) ZIF-Clip® headstage depicted as required by the single-ended (3a) and differential (3b) configuration; G, Ground, R, Reference; W, Working electrodes. Black circle represents a skull screw; (4) PZ2-256 battery-powered preamplifier; (5) fast fiber optic connection; (6) Workstation equipped with the RZ2 real-time processor and a computer.

To elicit the SEPs, a vibrating system was used to produce a multi-whisker deflection along the horizontal plane. Rat whiskers contralateral to the craniotomy were shortened to 2–3 cm and inserted in a Velcro strip attached to a rod moved by a shaker (Type 4810 mini shaker, Brüel & Kjær, Denmark) controlled by a National Instruments board (USA). In single whisker stimulation, in place of the Velcro strip, the whisker of interest was inserted into a needle attached to the rod. In both cases, the deflection stimulus—consisting of a sine waveform of 12-ms duration and an amplitude coincident with whisker deflection of 500 μm—was repeated 60 times and separated from the others by a 4 s pause.

8. Intraoperative µECoG Recordings in Humans

With the aim of recording neural signal related to speech production, the ultra-conformable MuSA was tested on one male subject undergoing awake neurosurgery for tumor resection (low-grade glioma). The patient provided informed consent, and the protocol was approved by the ethics committee of Azienda Ospedaliera Universitaria Santa Maria della Misericordia (Udine, Italy). Before use, the device was sterilized using ethylene oxide (EtO) as required by hospital procedures. Data were collected before the brain tumor resection was performed. The placement of the µECoG over a healthy and informative portion of the cortex was obtained via preoperative and intraoperative investigations. Indeed, as required by the pre-surgical routine, the patient underwent functional magnetic resonance imaging (fMRI) while performing a naming task to localize the responsive areas and their distance from the tumor. Finally, to identify the speech arrest area and center the µECoG array above it, cortical mapping was carried out through intraoperative electrical stimulation (IES).

Neural data were acquired at 3051 samples/s using the same recording system described in the previous section. The reference and ground pins of the headstage were tied together (single-ended configuration) and connected to the subject's dura mater. The patient's voice was acquired at 24 kHz for the entire recording session.

The subject, an Italian native speaker, was asked to repeat the same naming assignment performed during the fMRI scan. This procedure is also routinely used together with others (e.g., counting task) during surgery to monitor speech functionality while removing the tumor. The task consisted of naming 10 different images shown on a screen three times in the same order (Figure 38).

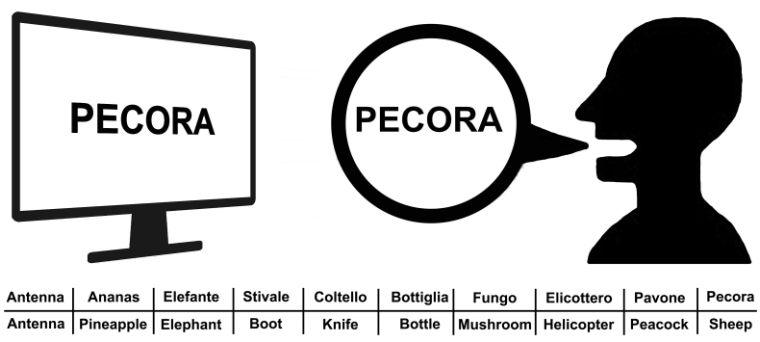

Figure 38 Sketch of the naming task and Italian nouns repeated during the assignment with the relative English translation.

9. In vivo Recording Data Analysis

9.1 Rat Data Analysis

Neural signal analysis of the MuSA was performed using NeuroExplorer® software (Version 5.115, Nex Technologies, USA). To verify the consistency of the multi-unit activity recorded from the surface of the cortex after the peripheral stimulation, spike detection from ECoG raw signals was performed as follows: data were band-pass–filtered between 200 Hz and 6 kHz (filter order, 4) a -3 standard deviation threshold was set, and no refractory period was assumed [28]. The detected spike times of occurrence were then visualized by computing raster plots. Subsequently, peri-event time histograms were calculated, time-locking the data to the start of the whisker stimulation. This analysis shows the conditional probability of a spike at time *t0+t* on the condition that there is a reference event at *t0*. Here, *t0* was set at the start of the whisker stimulation and *t* was set to 5-ms long bins. Spikes/s normalization was obtained as follows:

$$\frac{n_{counts}}{n_{trials} \times t}$$

where n_{counts} were the bin counts of the histogram and n_{trials} were the number of whisker stimulations (specifically, $n_{trials} = 60$).

To assess the chronic performances of the different electrode materials, the PMR was calculated as the peri-event histogram peak value divided by the background mean value (bins outside peak and trough) considering a time window from 50 ms before and 200 ms after the stimulation. Data reported in Figure 14 are presented as the mean of all channels ± SEM (specifically, for each Pt rat, n = 16; for each IrOx or PEDOT/PSS rat, n = 8) over the weeks for a total of eight rats (four Pt rats and four IrOx and PEDOT/PSS rats). The Log(PMRgap) was calculated as the base 10-logarithm of the ratio between the PMR mean value of the small electrodes over that of the large electrodes at every recorded week from two representative rats (one Pt rat and one IrOx and PEDOT/PSS rat).

The coherence matrixes—understood as a measure of the degree of the relationship between two time series, as a function of frequency—were calculated

on 300 s of spontaneous activity from 200 to 6000 Hz (256 frequency values, Hamming windowing function, window overlap of 50%).

To obtain the conditional probability of a spike at *t0+t* (considering as the reference event at *t0* the detected spike events of one selected electrode), cross-correlograms were calculated on 300 s of spontaneous activity, *t* was set at 1 ms long bins, and probability normalization was obtained dividing the bin count by the number of reference events (number of spikes detected by the electrode selected as the reference variable).

For the signal processing of the CaLEAF data, analysis was carried out using built-in tools and custom-made functions developed in MATLAB Environment (version 9.3, Mathworks) by Emanuela Delfino. Raw data were segmented into trials of 80 ms, time-locked to the stimulation (ranging from 20 ms before the onset to 60 ms after it). A 100-ms interval preceding the stimulation onset was considered for each trial as the background noise to compute the SNR. To extract the high-frequency components (HFCs) of the SEP, time series were band-pass–filtered from 200 to 1000 Hz using a digital zero-phase fourth-order Butterworth filter. Then, the filtered trials were averaged for visualization and for comparing the SEPs in the different experimental conditions. To better understand the spatial distribution of the evoked potentials, the analytic upper envelope of the averaged HFCs was considered. The peak amplitude of the envelope was used as the feature to quantify the size of the evoked responses recorded with different electrodes. To model the spatial distribution of the SEPs across the array, the features were spatially interpolated in a bidimensional map by fitting the 4 × 4 peak amplitude matrix with a thin-plate spline model available in the MATLAB Curve Fitting Toolbox. To assess the quality of the recordings for the HFCs of each electrode, the SNR was calculated as follows:

$$SNR_{el} = median\left(\frac{S_{i,el}}{2 * std(N_{i,el})}\right)$$

where $S_{i,el}$ is the peak-to-peak amplitude of the i^{th} trial for the electrode *el*, and $N_{i,el}$ is the standard deviation of 100 ms before the i^{th} stimulation for the same electrode. Then, the SNR_{el} was computed as the median value over trials.

9.2 Human Data Analysis

The analyses of the data recorded from the human subject were conducted in MATLAB (version 9.5, Mathworks, Inc., USA) by Emanuela Delfino. Speech timings were extracted with the free software Audacity® (version 2.1.2). The recorded signals were filtered using eighth-order Butterworth band-pass filters in the traditional beta (15–30 Hz), gamma (30–60 Hz), and high gamma (70–150 Hz) bands. Accordingly, 50 Hz and the harmonics up to 150 Hz were removed with notch filters. The timing of the speech production was used to segment the filtered data into trials starting from 500 ms before to 500 ms after the speech onset. For the spectrograms, the power was extracted every 10 ms, considering a window of 100 ms. Then, the mean spectrogram for each electrode was obtained, averaging across trials. The single-trial and mean spectrograms of all frequency bands of interest were then visually inspected to exclude the presence of artefacts. Subsequently, the spectrograms calculated on the entire recording for the frequency bands of interest were averaged across frequencies to obtain a mean time-varying profile of the power spectral density, referred to as the mean power profile (MPP).

Publications

I. Flexible Bioelectronic Devices Based on Micropatterned Monolithic Carbon Fiber Mats

Vomero M., Gueli C., Zucchini E., Fadiga L., Erhardt J.B., Sharma S. and Stieglitz T.

Abstract. Polymer-derived carbon can serve as an electrode material in multimodal neural stimulation, recording and neurotransmitter sensing platforms. The primary challenge in its applicability in implantable, flexible neural devices is its characteristic mechanical hardness that renders it difficult to fabricate the entire device using only carbon. We introduce a microfabrication technique for patterning flexible, cloth-like, polymer-derived carbon fiber (CF) mats embedded in polyimide (PI), via selective reactive ion etching (RIE). This scalable, monolithic manufacturing method eliminates any joints or metal interconnects and creates electrocorticography (ECoG) electrode arrays based on a single CF mat. The batch-fabricated CF/PI composite structures, with critical dimension of 12.5 µm, are tested for their mechanical, electrical and electrochemical stability, as well as to chemicals that mimic acute post-surgery inflammatory reactions. Their recording performance is validated in rat models. Reported CF patterning process can benefit various carbon micro-devices that are expected to feature flexibility, material stability and biocompatibility.

Advanced Materials Technologies, 2019 (Accepted)

II. Can Crosstalk Compromise the Recording of High-Frequency Neural Signals?

Porto Cruz M.F., Vomero M., Zucchini E., Delfino E., Asplund M., Stieglitz T. and Fadiga L.

Abstract. Two big trends are leading the way to a new generation of thin-film electrocorticography (ECoG) micro electrode arrays (MEAs): miniaturization, which combines higher electrode densities with thinner substrates for conformability purposes; and the pursuit to extend the recording frequency band to 1 kHz and beyond (recording of spikes). When combining these two trends,

however, the frequency-dependent phenomenon of crosstalk emerges as a possible setback to the so desired spatial selectivity. In this work, high *in vivo* coherences at 1 kHz be-tween electrodes with neighboring tracks are reported when using the MuSA (Multi-Species Array) as recording ECoG MEA on rats. These results suggest a high degree of crosstalk between closely routed electrodes, even if placed far apart on the array, and are corroborated by coherence plots of control recordings *in vitro* in phosphate buffered saline (PBS). As means to estimate the combined leakage resistance and capacitance between the signal lines and the targeted brain tissue, an impedance spatial sweep over the 32 tracks routing the MuSA electrodes is performed in PBS in a two-electrode electrochemical impedance spectroscopy setup. This study should raise awareness of crosstalk as an important aspect to consider when aiming for high-quality, high-density and high-frequency neural recordings.

International IEEE/EMBS Conference on Neural Engineering, NER, 2019
DOI: 10.1109/NER.2019.8717009

III. Electrodeposited PEDOT:Nafion Composite for Neural Recording and Stimulation

Carli S., Bianchi M., Zucchini E., Di Lauro M., Prato M., Murgia M., Fadiga L. and Biscarini F.

Abstract. Microelectrode arrays are used for recording and stimulation in neurosciences both *in vitro* and *in vivo*. The electrodeposition of conductive polymers, such as poly(3,4-ethylene dioxythiophene) (PEDOT), is widely adopted to improve both the *in vivo* recording and the charge injection limit of metallic microelectrodes. The workhorse of conductive polymers in the neurosciences is PEDOT:PSS, where PSS represents polystyrene-sulfonate. In this paper, the counterion is the fluorinated polymer Nafion, so the composite PEDOT:Nafion is deposited onto a flexible neural microelectrode array. PEDOT:Nafion coated electrodes exhibit comparable *in vivo* recording capability to the reference PEDOT:PSS, providing a large signal-to-noise ratio in a murine animal model. Importantly, PEDOT:Nafion exhibits a minimized polarization during electrical stimulation, thereby resulting in an improved

charge injection limit equal to 4.4 mC cm−2, almost 80% larger than the 2.5 mC cm−2 that is observed for PEDOT:PSS.

Advanced healthcare materials, 2019

DOI: 10.1002/adhm.201900765

IV. Achieving Ultra-Conformability with Polyimide-Based ECoG Arrays

Vomero M., Cruz M.F.P., Zucchini E., Shabanian A., Delfino E., Carli S., Fadiga L., Ricci D. and Stieglitz T.

Abstract. Micro-electrode arrays for electrocorticography (ECoG) represent the best compromise between invasiveness and signal quality, as they are surface devices that still allow high sensitivity recordings. In this work, an assessment of different technical aspects determining the ultimate performance of ultra-conformable polyimide-based μECoG arrays is conducted via a finite element model, impedance spectroscopy measurements and recordings of sensorimotor evoked potentials (SEPs) in rats. The finite element model proves that conformability of thin-film arrays can be achieved with polyimide, a non-stretchable material, by adjusting its thickness according to the curvature of the targeted anatomical area. From the electrochemical characterization of the devices, intrinsic thermal noise of platinum and gold electrodes is estimated to be 3-5 μV. Results show that electrode size and *in vitro* impedance do not influence the amplitude of the recorded SEPs. However, the use of a reference on-skull (a metal screw), as compared to reference on-array (a metal electrode surrounding the recording area), provides higher-amplitude SEPs. Additionally, the incorporation of a grounded metal shield in the thin-film devices limits crosstalk between tracks and does not compromise the recording capabilities of the arrays.

Annual International Conference of the IEEE Engineering in Medicine and Biology – Proceedings, 2018

DOI: 10.1109/EMBC.2018.8513171

V. Glassy carbon electrocorticography electrodes on Ultra-Thin and Finger-Like Polyimide Substrate: Performance evaluation based on different electrode diameters

*Vomero M., *Zucchini E., Delfino E., Gueli C., Mondragon N.C., Carli S., Fadiga L. and Stieglitz T.

*equally contributed to this work

Abstract. Glassy carbon (GC) has high potential to serve as a biomaterial in neural applications because it is biocompatible, electrochemically inert and can be incorporated in polyimide-based implantable devices. Miniaturization and applicability of GC is, however, thought to be partially limited by its electrical conductivity. For this study, ultra-conformable polyimide-based electrocorticography (ECoG) devices with different-diameter GC electrodes were fabricated and tested *in vitro* and in rat models. For achieving conformability to the rat brain, polyimide was patterned in a finger-like shape and its thickness was set to 8 µm. To investigate different electrode sizes, each ECoG device was assigned electrodes with diameters of 50, 100, 200 and 300 µm. They were electrochemically characterized and subjected to 10 million biphasic pulses-for achieving a steady-state-and to X-ray photoelectron spectroscopy, for examining their elemental composition. The electrodes were then implanted epidurally to evaluate the ability of each diameter to detect neural activity. Results show that their performance at low frequencies (up to 300 Hz) depends on the distance from the signal source rather than on the electrode diameter, while at high frequencies (above 200 Hz) small electrodes have higher background noises than large ones, unless they are coated with poly(3,4-ethylenedioxythiophene)-poly(styrenesulfonate) (PEDOT:PSS).

Materials, 2018

DOI: 10.3390/ma11122486

VI. Glassy carbon MEMS for novel origami-styled 3D integrated intracortical and epicortical neural probes

Goshi N., Castagnola E., Vomero M., Gueli C., Cea C., Zucchini E., Bjanes D., Maggiolini E., Moritz C., Kassegne S., Ricci D. and Fadiga L.

Abstract. We report on a novel technology for microfabricating 3D origami-styled micro electromechanical systems (MEMS) structures with glassy carbon (GC) features and a supporting polymer substrate. GC MEMS devices that open to form 3D microstructures are microfabricated from GC patterns that are made through pyrolysis of polymer precursors on high-temperature resisting substrates like silicon or quartz and then transferring the patterned devices to a flexible substrate like polyimide followed by deposition of an insulation layer. The devices on flexible substrate are then folded into 3D form in an origami-fashion. These 3D MEMS devices have tunable mechanical properties that are achieved by selectively varying the thickness of the polymeric substrate and insulation layers at any desired location. This technology opens new possibilities by enabling microfabrication of a variety of 3D GC MEMS structures suited to applications ranging from biochemical sensing to implantable microelectrode arrays. As a demonstration of the technology, a neural signal recording microelectrode array platform that integrates both surface (cortical) and depth (intracortical) GC microelectrodes onto a single flexible thin-film device is introduced. When the device is unfurled, a pre-shaped shank of polyimide automatically comes off the substrate and forms the penetrating part of the device in a 3D fashion. With the advantage of being highly reproducible and batch-fabricated, the device introduced here allows for simultaneous recording of electrophysiological signals from both the brain surface (electrocorticography-ECoG) and depth (single neuron). Our device, therefore, has the potential to elucidate the roles of underlying neurons on the different components of μECoG signals. For *in vivo* validation of the design capabilities, the recording sites are coated with a poly(3,4-ethylenedioxythiophene)-polystyrene sulfonate-carbon nanotube composite, to improve the electrical conductivity of the electrodes and consequently the quality of the recorded signals. Results show that both μECoG and intracortical arrays were able to acquire neural signals with high-sensitivity that increased with depth, thereby verifying the device functionality.

Journal of Micromechanics and Microengineering, 2018

DOI: 10.1088/1361-6439/aab061

VII. Incorporation of Silicon Carbide and Diamond-Like Carbon as Adhesion Promoters Improves *In Vitro* and *In Vivo* Stability of Thin-Film Glassy Carbon Electrocorticography Arrays

Vomero M., Castagnola E., Ordonez J.S., Carli S., Zucchini E., Maggiolini E., Gueli C., Goshi N., Ciarpella F., Cea C., Fadiga L., Ricci D., Kassegne S. and Stieglitz T.

Abstract. Thin-film neural devices are an appealing alternative to traditional implants, although their chronic stability remains matter of investigation. In this study, a chronically stable class of thin-film devices for electrocorticography is manufactured incorporating silicon carbide and diamond-like carbon as adhesion promoters between glassy carbon (GC) electrodes and polyimide and between GC and platinum traces. The devices are aged in three solutions—phosphate-buffered saline (PBS), 30 × 10 −3 and 150 × 10 −3 m H 2 O 2 /PBS—and stressed using cyclic voltammetry (2500 cycles) and 20 million biphasic pulses. Electrochemical impedance spectroscopy (EIS) and image analysis are performed to detect eventual changes of the electrodes morphology. Results demonstrate that the devices are able to undergo chemically induced oxidative stress and electrical stimulation without failing but actually improving their electrical performance until a steady state is reached. Additionally, cell viability tests are carried out to verify the noncytotoxicity of the materials, before chronically implanting them into rat models. The behavior of the GC electrodes *in vivo* is monitored through EIS and sensorimotor evoked potential recordings which confirm that, with GC being activated, impedance lowers and quality of recorded signal improves. Histological analysis of the brain tissue is performed and shows no sign of severe immune reaction to the implant.

Advanced Biosystems, 2018

DOI: 10.1002/adbi.201700081

VIII. *In Vivo* Dopamine Detection and Single Unit Recordings Using Intracortical Glassy Carbon Microelectrode Arrays

Castagnola E., Winchester Vahidi N., Nimbalkar S., Rudraraju S., Thielk M., Zucchini E., Cea C., Carli S., Gentner T.Q., Ricci D., Fadiga L. and Kassegne S.

Abstract. In this study, we present a 4-channel intracortical glassy carbon (GC) microelectrode array on a flexible substrate for the simultaneous *in vivo* neural activity recording and dopamine (DA) concentration measurement at four different brain locations (220m vertical spacing). The ability of GC microelectrodes to detect DA was firstly assessed *in vitro* in phosphate-buffered saline solution and then validated *in vivo* measuring spontaneous DA concentration in the Striatum of European Starling songbird through fast scan cyclic voltammetry(FSCV). The capability of GC microelectrode arrays and commercial penetrating metal microelectrode arrays to record neural activity from the Caudomedial Neostriatum of European starling songbird was compared. Preliminary results demonstrated the ability of GC microelectrodes in detecting neurotransmitters release and recording neural activity *in vivo*. GC microelectrodes array may, therefore, offer a new opportunity to understand the intimate relations linking electrophysiological parameters with neurotransmitters release.

MRS Advances, 2018

DOI: 10.1557/adv.2018.98

IX. Single walled carbon nanohorns composite for neural sensing and stimulation

Carli S., Lambertini L., Zucchini E., Ciarpella F., Scarpellini A., Prato M., Castagnola E., Fadiga L. and Ricci D.

Abstract. Oxidized single walled carbon nanohorns (ox-SWCNH) were electrodeposited onto gold microelectrode arrays in conjunction with poly(3,4-ethylenedioxythiophene) (PEDOT) and polystirenesulfonate (PSS), and the properties of the new composite material for neural recording and stimulation were assessed. PEDOT/ox-SWCNH composites were compared with films prepared with one of the most notorious carbonaceous material in this field, the oxidized multi-walled Carbon Nanotubes (ox-MWCNT). The PEDOT/ox-SWCNH exhibited superior charge transfer capability, reflecting greater electroactive surface, as confirmed by SEM and EIS characterizations. As a consequence, a charge injection limit of 11.6 mC/cm2 was observed for the new

composite, which is higher than the one of PEDOT/ox-MWCNT (8.7 mC/cm2). Having confirmed comparable neural recording performance, the PEDOT/ox-SWCNH composite results very promising for improving therapeutic electrical stimulation in the central and peripheral nervous systems.

Sensors and Actuators, B: Chemical, 2018

DOI: 10.1016/j.snb.2018.05.083

X. Highly Stable Glassy Carbon Interfaces for Long-Term Neural Stimulation and Low-Noise Recording of Brain Activity

Vomero M., Castagnola E., Ciarpella F., Maggiolini E., Goshi N., Zucchini E., Carli S., Fadiga L., Kassegne S. and Ricci D.

Abstract. We report on the superior electrochemical properties, in-vivo performance and long term stability under electrical stimulation of a new electrode material fabricated from lithographically patterned glassy carbon. For a direct comparison with conventional metal electrodes, similar ultra-flexible, micro-electrocorticography (μ-ECoG) arrays with platinum (Pt) or glassy carbon (GC) electrodes were manufactured. The GC microelectrodes have more than 70% wider electrochemical window and 70% higher CTC (charge transfer capacity) than Pt microelectrodes of similar geometry. Moreover, we demonstrate that the GC microelectrodes can withstand at least 5 million pulses at 0.45 mC/cm2 charge density with less than 7.5% impedance change, while the Pt microelectrodes delaminated after 1 million pulses. Additionally, poly(3,4-ethylenedioxythiophene)-poly(styrenesulfonate) (PEDOT-PSS) was selectively electrodeposited on both sets of devices to specifically reduce their impedances for smaller diameters (<60 μm). We observed that PEDOT-PSS adhered significantly better to GC than Pt, and allowed drastic reduction of electrode size while maintaining same amount of delivered current. The electrode arrays biocompatibility was demonstrated through in-vitro cell viability experiments, while acute *in vivo* characterization was performed in rats and showed that GC microelectrode arrays recorded somatosensory evoked potentials (SEP) with an almost twice SNR (signal-to-noise ratio) when compared to the Pt ones.

Scientific Reports, 2017

DOI: 10.1038/srep40332

XI. Improved long-term stability of thin-film glassy carbon electrodes through the use of silicon carbide and amorphous carbon

Vomero M., Castagnola E., Ordonez J.S., Carli S., Zucchini E., Maggiolini E., Gueli C., Goshi N., Fadiga L., Ricci D., Kassegne S. and Stieglitz T.

Abstract. Long-term stability of neural interfaces is a challenge that has still to be overcome. In this study, we manufactured a highly stable multi-layer thin-film class of carbon-based devices for electrocorticography (ECoG) incorporating silicon carbide (SiC) and amorphous carbon (DLC) as adhesion promoters between glassy carbon (GC) electrodes and polyimide (PI) substrate and between PI and platinum (Pt) traces. We aged the thin-film electrodes in 30 mM H2O2 at 39 °C for one week - to mimic the effects of post-surgery inflammatory reaction - and subsequently stressed them with 2500 CV cycles. We additionally performed stability tests stimulating the electrodes with 15 million biphasic pulses. Finally, we implanted the electrodes for 6 weeks into rat models and optically characterized the explanted devices. Results show that the fabricated ECoG devices were able to withstand the *in vitro* and *in vivo* tests without significant change in impedance and morphology.

International IEEE/EMBS Conference on Neural Engineering, NER, 2017
DOI: 10.1109/NER.2017.8008347

XII. pHEMA encapsulated PEDOT-PSS-CNT microsphere microelectrodes for recording single unit activity in the brain

Castagnola E., Maggiolini E., Ceseracciu L., Ciarpella F., Zucchini E., De Faveri S., Fadiga L. and Ricci D.

Abstract. The long-term reliability of neural interfaces and stability of high-quality recordings are still unsolved issues in neuroscience research. High surface area PEDOT-PSS-CNT composites are able to greatly improve the performance of recording and stimulation for traditional intracortical metal microelectrodes by decreasing their impedance and increasing their charge transfer capability. This enhancement significantly reduces the size of the

implantable device though preserving excellent electrical performances. On the other hand, the presence of nanomaterials often rises concerns regarding possible health hazards, especially when considering a clinical application of the devices. For this reason, we decided to explore the problem from a new perspective by designing and testing an innovative device based on nanostructured microspheres grown on a thin tether, integrating PEDOT-PSS-CNT nanocomposites with a soft synthetic permanent biocompatible hydrogel. The pHEMA hydrogel preserves the electrochemical performance and high quality recording ability of PEDOT-PSS-CNT coated devices, reduces the mechanical mismatch between soft brain tissue and stiff devices and also avoids direct contact between the neural tissue and the nanocomposite, by acting as a biocompatible protective barrier against potential nanomaterial detachment. Moreover, the spherical shape of the electrode together with the surface area increase provided by the nanocomposite deposited on it, maximize the electrical contact and may improve recording stability over time. These results have a good potential to contribute to fulfill the grand challenge of obtaining stable neural interfaces for long-term applications.

Frontiers in Neuroscience, 2016
DOI: 10.3389/fnins.2016.00151

References

[1] L. Galvani, “De Viribus Electricitatis in Motu Musculari Commentarius,” *Bol. Accad. delle Sci.*, 1791.

[2] G. Hong and C. M. Lieber, “Novel electrode technologies for neural recordings,” *Nat. Rev. Neurosci.*, vol. 20, no. 6, pp. 330–345, 2019.

[3] M. Pais-Vieira *et al.*, “A Closed Loop Brain-machine Interface for Epilepsy Control Using Dorsal Column Electrical Stimulation,” *Sci. Rep.*, vol. 6, p. 32814, Sep. 2016.

[4] R. Alkawadri, “Brain–Computer Interface (BCI) Applications in Mapping of Epileptic Brain Networks Based on Intracranial-EEG: An Update ,” *Frontiers in Neuroscience* , vol. 13. p. 191, 2019.

[5] A. Gummadavelli, H. P. Zaveri, D. D. Spencer, and J. L. Gerrard, “Expanding Brain-Computer Interfaces for Controlling Epilepsy Networks: Novel Thalamic Responsive Neurostimulation in Refractory Epilepsy,” *Front. Neurosci.*, vol. 12, p. 474, Jul. 2018.

[6] J. Y. Fang and C. Tolleson, “The role of deep brain stimulation in Parkinson’s disease: an overview and update on new developments,” *Neuropsychiatr. Dis. Treat.*, vol. 13, pp. 723–732, Mar. 2017.

[7] P. Limousin and T. Foltynie, “Long-term outcomes of deep brain stimulation in Parkinson disease,” *Nat. Rev. Neurol.*, vol. 15, no. 4, pp. 234–242, 2019.

[8] M. D. Serruya, N. G. Hatsopoulos, L. Paninski, M. R. Fellows, and J. P. Donoghue, “Instant neural control of a movement signal,” *Nature*, vol. 416, no. 6877, pp. 141–142, 2002.

[9] L. R. Hochberg *et al.*, “Neuronal ensemble control of prosthetic devices by a human with tetraplegia,” *Nature*, vol. 442, no. 7099, pp. 164–171, 2006.

[10] J. M. Carmena *et al.*, “Learning to Control a Brain–Machine Interface for Reaching and Grasping by Primates,” *PLOS Biol.*, vol. 1, no. 2, p. e42, Oct. 2003.

[11] J. L. Collinger *et al.*, “High-performance neuroprosthetic control by an individual with tetraplegia,” *Lancet*, vol. 381, no. 9866, pp. 557–564, Feb. 2013.

[12] N. Kasthuri and J. W. Lichtman, “Neurocartography,” *Neuropsychopharmacology*, vol. 35, no. 1, pp. 342–343, Jan. 2010.

[13] P. G. Haydon, “Glia: listening and talking to the synapse,” *Nat. Rev. Neurosci.*, vol. 2, no. 3, pp. 185–193, 2001.

[14] B. A. Barres, “The Mystery and Magic of Glia: A Perspective on Their Roles in Health and Disease,” *Neuron*, vol. 60, no. 3, pp. 430–440, Nov. 2008.

[15] G. Buzsáki, C. A. Anastassiou, and C. Koch, “The origin of extracellular fields and currents — EEG, ECoG, LFP and spikes,” *Nat. Rev. Neurosci.*, vol. 13, no. 6, pp. 407–420, 2012.

[16] J. Rivnay, H. Wang, L. Fenno, K. Deisseroth, and G. G. Malliaras, “Next-generation probes, particles, and proteins for neural interfacing,” *Sci. Adv.*, vol. 3, no. 6, pp. 1–20, 2017.

[17] R. Biran, D. C. Martin, and P. A. Tresco, “Neuronal cell loss accompanies the brain tissue response to chronically implanted silicon microelectrode arrays,” *Exp. Neurol.*, vol. 195, no. 1, pp. 115–126, 2005.

[18] M. Jorfi, J. L. Skousen, C. Weder, and J. R. Capadona, “Progress towards biocompatible intracortical microelectrodes for neural interfacing applications,” *J. Neural Eng.*, vol. 12, no. 1, p. 11001, Feb. 2015.

[19] M. E. J. Obien, K. Deligkaris, T. Bullmann, D. J. Bakkum, and U. Frey, “Revealing neuronal function through microelectrode array recordings,” *Front. Neurosci.*, vol. 8, p. 423, Jan. 2015.

[20] R. Yuste, “From the neuron doctrine to neural networks,” *Nat. Rev. Neurosci.*, vol. 16, no. 8, pp. 487–497, 2015.

[21] R. Chen, A. Canales, and P. Anikeeva, “Neural recording and modulation technologies,” *Nat. Rev. Mater.*, vol. 2, no. 2, pp. 1–16, 2017.

[22] K. M. Szostak, L. Grand, and T. G. Constandinou, “Neural Interfaces for Intracortical Recording: Requirements, Fabrication Methods, and Characteristics,” *Front. Neurosci.*, vol. 11, p. 665, Dec. 2017.

[23] S. Machado *et al.*, “EEG-based Brain-Computer Interfaces: An Overview of Basic Concepts and Clinical Applications in Neurorehabilitation,” *Reviews in the Neurosciences*, vol. 21. p. 451, 2010.

[24] I. Lazarou, S. Nikolopoulos, P. C. Petrantonakis, I. Kompatsiaris, and M. Tsolaki, “EEG-Based Brain–Computer Interfaces for Communication and Rehabilitation of People with Motor Impairment: A Novel Approach of the 21st Century ,” *Frontiers in Human Neuroscience* , vol. 12. p. 14, 2018.

[25] G. Buzsáki, *Rhythms of the Brain*. 2009.

[26] S. Ray and J. H. R. Maunsell, “Do gamma oscillations play a role in cerebral

cortex?," *Trends Cogn. Sci.*, vol. 19, no. 2, pp. 78–85, Feb. 2015.

[27] D. Khodagholy *et al.*, "NeuroGrid: recording action potentials from the surface of the brain," *Nat. Neurosci.*, vol. 18, p. 310, Dec. 2014.

[28] T. Bockhorst, F. Pieper, G. Engler, T. Stieglitz, E. Galindo-Leon, and A. K. Engel, "Synchrony surfacing: Epicortical recording of correlated action potentials," *Eur. J. Neurosci.*, vol. 48, no. 12, pp. 3583–3596, Dec. 2018.

[29] M. Vomero *et al.*, "Achieving Ultra-Conformability With Polyimide-Based ECoG Arrays," in *2018 40th Annual International Conference of the IEEE Engineering in Medicine and Biology Society (EMBC)*, 2018, pp. 4464–4467.

[30] M. Jorfi, J. L. Skousen, C. Weder, and J. R. Capadona, "Progress towards biocompatible intracortical microelectrodes for neural interfacing applications," *J. Neural Eng.*, vol. 12, no. 1, 2015.

[31] M. P. Ward, P. Rajdev, C. Ellison, and P. P. Irazoqui, "Toward a comparison of microelectrodes for acute and chronic recordings," *Brain Res.*, vol. 1282, pp. 183–200, 2009.

[32] A. Prasad *et al.*, "Comprehensive characterization and failure modes of tungsten microwire arrays in chronic neural implants," *J. Neural Eng.*, vol. 9, no. 5, p. 56015, 2012.

[33] A. Prasad *et al.*, "Abiotic-biotic characterization of Pt/Ir microelectrode arrays in chronic implants ," *Frontiers in Neuroengineering* , vol. 7. p. 2, 2014.

[34] J. C. Barrese *et al.*, "Failure mode analysis of silicon-based intracortical microelectrode arrays in non-human primates," *J. Neural Eng.*, vol. 10, no. 6, p. 66014, 2013.

[35] E. Patrick, M. E. Orazem, J. C. Sanchez, and T. Nishida, "Corrosion of tungsten microelectrodes used in neural recording applications," *J. Neurosci. Methods*, vol. 198, no. 2, pp. 158–171, 2011.

[36] L. A. Geddes and R. Roeder, "Criteria for the selection of materials for implanted electrodes," *Ann. Biomed. Eng.*, vol. 31, no. 7, pp. 879–890, 2003.

[37] G. Schmitt, J.-W. Schultze, F. Faßbender, G. Buß, H. Lüth, and M. J. Schöning, "Passivation and corrosion of microelectrode arrays," *Electrochim. Acta*, vol. 44, no. 21, pp. 3865–3883, 1999.

[38] C. S. Bjornsson *et al.*, "Effects of insertion conditions on tissue strain and vascular damage during neuroprosthetic device insertion," *J. Neural Eng.*, vol. 3, no. 3, pp. 196–207, 2006.

[39] P. A. House, J. D. MacDonald, P. A. Tresco, and R. A. Normann, "Acute

microelectrode array implantation into human neocortex: preliminary technique and histological considerations.," *Neurosurg. Focus*, vol. 20, no. 5, p. E4, May 2006.

[40] J. Subbaroyan, D. C. Martin, and D. R. Kipke, "A finite-element model of the mechanical effects of implantable microelectrodes in the cerebral cortex," *J. Neural Eng.*, vol. 2, no. 4, pp. 103–113, 2005.

[41] A. Hess *et al.*, "A bio-inspired, chemo-responsive polymer nanocomposite for mechanically dynamic microsystems," in *TRANSDUCERS 2009 - 2009 International Solid-State Sensors, Actuators and Microsystems Conference*, 2009, pp. 224–227.

[42] S. R. Goldstein and M. Salcman, "Mechanical Factors in the Design of Chronic Recording Intracortical Microelectrodes," *IEEE Trans. Biomed. Eng.*, vol. BME-20, no. 4, pp. 260–269, 1973.

[43] V. S. Polikov, P. A. Tresco, and W. M. Reichert, "Response of brain tissue to chronically implanted neural electrodes," *J. Neurosci. Methods*, vol. 148, no. 1, pp. 1–18, 2005.

[44] R. Biran, D. C. Martin, and P. A. Tresco, "The brain tissue response to implanted silicon microelectrode arrays is increased when the device is tethered to the skull," *J. Biomed. Mater. Res. Part A*, vol. 82A, no. 1, pp. 169–178, Jul. 2007.

[45] K. A. Potter, A. C. Buck, W. K. Self, and J. R. Capadona, "Stab injury and device implantation within the brain results in inversely multiphasic neuroinflammatory and neurodegenerative responses," *J. Neural Eng.*, vol. 9, no. 4, p. 46020, 2012.

[46] M. Ravikumar, S. Jain, R. H. Miller, J. R. Capadona, and S. M. Selkirk, "An organotypic spinal cord slice culture model to quantify neurodegeneration," *J. Neurosci. Methods*, vol. 211, no. 2, pp. 280–288, 2012.

[47] J. Gehrmann, Y. Matsumoto, and G. W. Kreutzberg, "Microglia: Intrinsic immuneffector cell of the brain," *Brain Res. Rev.*, vol. 20, no. 3, pp. 269–287, 1995.

[48] M. L. Block, L. Zecca, and J.-S. Hong, "Microglia-mediated neurotoxicity: uncovering the molecular mechanisms," *Nat. Rev. Neurosci.*, vol. 8, no. 1, pp. 57–69, 2007.

[49] C. C. Chao, S. Hu, and P. K. Peterson, "Glia, cytokines, and neurotoxicity.," *Crit. Rev. Neurobiol.*, vol. 9, no. 2–3, pp. 189–205, 1995.

[50] U.-K. Hanisch and H. Kettenmann, “Microglia: active sensor and versatile effector cells in the normal and pathologic brain,” *Nat. Neurosci.*, vol. 10, no. 11, pp. 1387–1394, 2007.

[51] A. Mantovani, S. Sozzani, M. Locati, P. Allavena, and A. Sica, “Macrophage polarization: tumor-associated macrophages as a paradigm for polarized M2 mononuclear phagocytes,” *Trends Immunol.*, vol. 23, no. 11, pp. 549–555, Nov. 2002.

[52] M. Aschner, U. Sonnewald, and K. H. Tan, “Astrocyte Modulation of Neurotoxic Injury,” *Brain Pathol.*, vol. 12, no. 4, pp. 475–481, Oct. 2002.

[53] V. Guénard, G. Frisch, and P. M. Wood, “Effects of Axonal Injury on Astrocyte Proliferation and Morphologyin Vitro:Implications for Astrogliosis,” *Exp. Neurol.*, vol. 137, no. 2, pp. 175–190, 1996.

[54] D. F. Louw, T. Masada, and G. R. Sutherland, “Ischemic Neuronal Injury is Ameliorated by Astrocyte Activation,” *Can. J. Neurol. Sci. / J. Can. des Sci. Neurol.*, vol. 25, no. 2, pp. 102–107, 1998.

[55] M. D. Norenberg, “Astrocyte Responses to CNS Injury,” *J. Neuropathol. Exp. Neurol.*, vol. 53, no. 3, pp. 213–220, May 1994.

[56] E. M. Schmidt, M. J. Bak, and J. S. McIntosh, “Long-term chronic recording from cortical neurons,” *Exp. Neurol.*, vol. 52, no. 3, pp. 496–506, 1976.

[57] J. C. Williams, J. A. Hippensteel, J. Dilgen, W. Shain, and D. R. Kipke, “Complex impedance spectroscopy for monitoring tissue responses to inserted neural implants.,” *J. Neural Eng.*, vol. 4, no. 4, pp. 410–423, Dec. 2007.

[58] J. C. COLLIAS and E. E. MANUELIDIS, “Histopathological changes produced by implanted electrodes in cat brains; comparison with histopathological changes in human and experimental puncture wounds.,” *J. Neurosurg.*, vol. 14, no. 3, pp. 302–328, May 1957.

[59] J. Thelin *et al.*, “Implant Size and Fixation Mode Strongly Influence Tissue Reactions in the CNS,” *PLoS One*, vol. 6, no. 1, p. e16267, Jan. 2011.

[60] A. D. Degenhart *et al.*, “Histological evaluation of a chronically-implanted electrocorticographic electrode grid in a non-human primate,” *J. Neural Eng.*, vol. 13, no. 4, p. 46019, Aug. 2016.

[61] P. Moshayedi *et al.*, “The relationship between glial cell mechanosensitivity and foreign body reactions in the central nervous system,” *Biomaterials*, vol. 35, no. 13, pp. 3919–3925, 2014.

[62] S. P. Lacour, G. Courtine, and J. Guck, “Materials and technologies for soft implantable neuroprostheses,” *Nat. Rev. Mater.*, vol. 1, no. 10, p. 16063, 2016.

[63] J. P. Seymour and D. R. Kipke, “Neural probe design for reduced tissue encapsulation in CNS,” *Biomaterials*, vol. 28, no. 25, pp. 3594–3607, 2007.

[64] J. L. Skousen, S. M. E. Merriam, O. Srivannavit, G. Perlin, K. D. Wise, and P. A. Tresco, “Reducing surface area while maintaining implant penetrating profile lowers the brain foreign body response to chronically implanted planar silicon microelectrode arrays,” in *Brain Machine Interfaces: Implications for Science, Clinical Practice and Society*, vol. 194, J. Schouenborg, M. Garwicz, and N. B. T.-P. in B. R. Danielsen, Eds. Elsevier, 2011, pp. 167–180.

[65] D. Kuzum *et al.*, “Transparent and flexible low noise graphene electrodes for simultaneous electrophysiology and neuroimaging,” *Nat. Commun.*, vol. 5, no. 1, p. 5259, 2014.

[66] E. W. Keefer, B. R. Botterman, M. I. Romero, A. F. Rossi, and G. W. Gross, “Carbon nanotube coating improves neuronal recordings,” *Nat. Nanotechnol.*, vol. 3, no. 7, pp. 434–439, 2008.

[67] A. Ansaldo, E. Castagnola, E. Maggiolini, L. Fadiga, and D. Ricci, “Superior Electrochemical Performance of Carbon Nanotubes Directly Grown on Sharp Microelectrodes,” *ACS Nano*, vol. 5, no. 3, pp. 2206–2214, Mar. 2011.

[68] G. Baranauskas *et al.*, “Carbon nanotube composite coating of neural microelectrodes preferentially improves the multiunit signal-to-noise ratio,” *J. Neural Eng.*, vol. 8, no. 6, p. 66013, 2011.

[69] E. Castagnola *et al.*, “PEDOT-CNT-Coated Low-Impedance, Ultra-Flexible, and Brain-Conformable Micro-ECoG Arrays,” *IEEE Trans. Neural Syst. Rehabil. Eng.*, vol. 23, no. 3, pp. 342–350, 2015.

[70] X. Luo, C. L. Weaver, D. D. Zhou, R. Greenberg, and X. T. Cui, “Highly stable carbon nanotube doped poly(3,4-ethylenedioxythiophene) for chronic neural stimulation,” *Biomaterials*, vol. 32, no. 24, pp. 5551–5557, 2011.

[71] E. Castagnola *et al.*, “pHEMA Encapsulated PEDOT-PSS-CNT Microsphere Microelectrodes for Recording Single Unit Activity in the Brain ,” *Frontiers in Neuroscience* , vol. 10. p. 151, 2016.

[72] S. Carli *et al.*, “Single walled carbon nanohorns composite for neural sensing and stimulation,” *Sensors Actuators B Chem.*, vol. 271, pp. 280–288, 2018.

[73] P. Fattahi, G. Yang, G. Kim, and M. R. Abidian, “A Review of Organic and

Inorganic Biomaterials for Neural Interfaces," *Adv. Mater.*, vol. 26, no. 12, pp. 1846–1885, Mar. 2014.

[74] R. Green and M. R. Abidian, "Conducting Polymers for Neural Prosthetic and Neural Interface Applications," *Adv. Mater.*, vol. 27, no. 46, pp. 7620–7637, Dec. 2015.

[75] U. A. Aregueta-Robles, A. J. Woolley, L. A. Poole-Warren, N. H. Lovell, and R. A. Green, "Organic electrode coatings for next-generation neural interfaces ," *Frontiers in Neuroengineering* , vol. 7. p. 15, 2014.

[76] S. M. Wellman and T. D. Y. Kozai, "Understanding the Inflammatory Tissue Reaction to Brain Implants To Improve Neurochemical Sensing Performance," *ACS Chem. Neurosci.*, vol. 8, no. 12, pp. 2578–2582, Dec. 2017.

[77] M. Vomero *et al.*, "Highly Stable Glassy Carbon Interfaces for Long-Term Neural Stimulation and Low-Noise Recording of Brain Activity," *Sci. Rep.*, vol. 7, p. 40332, Jan. 2017.

[78] M. Vomero *et al.*, "Incorporation of Silicon Carbide and Diamond-Like Carbon as Adhesion Promoters Improves In Vitro and In Vivo Stability of Thin-Film Glassy Carbon Electrocorticography Arrays," *Adv. Biosyst.*, vol. 2, no. 1, p. 1700081, 2018.

[79] M. Vomero *et al.*, "Glassy Carbon Electrocorticography Electrodes on Ultra-Thin and Finger-Like Polyimide Substrate: Performance Evaluation Based on Different Electrode Diameters," *Materials (Basel).*, vol. 11, no. 12, 2018.

[80] M. F. P. Cruz *et al.*, "Can Crosstalk Compromise the Recording of High-Frequency Neural Signals?," in *2019 9th International IEEE/EMBS Conference on Neural Engineering (NER)*, 2019, pp. 924–927.

[81] I. R. Minev *et al.*, "Electronic dura mater for long-term multimodal neural interfaces," *Science (80-.).*, vol. 347, no. 6218, pp. 159 LP – 163, Jan. 2015.

[82] D.-H. Kim *et al.*, "Dissolvable films of silk fibroin for ultrathin conformal bio-integrated electronics," *Nat. Mater.*, vol. 9, p. 511, Apr. 2010.

[83] L. Luan *et al.*, "Ultraflexible nanoelectronic probes form reliable, glial scar–free neural integration," *Sci. Adv.*, vol. 3, no. 2, p. e1601966, Feb. 2017.

[84] G. Lind, C. E. Linsmeier, and J. Schouenborg, "The density difference between tissue and neural probes is a key factor for glial scarring," *Sci. Rep.*, vol. 3, p. 2942, Oct. 2013.

[85] A. Gilletti and J. Muthuswamy, "Brain micromotion around implants in the

rodent somatosensory cortex," *J. Neural Eng.*, vol. 3, no. 3, pp. 189–195, 2006.

[86] A. A. Schendel *et al.*, "The effect of micro-ECoG substrate footprint on the meningeal tissue response," *J. Neural Eng.*, vol. 11, no. 4, p. 46011, Aug. 2014.

[87] G. Paxinos and C. Watson, "The rat brain in stereotaxic coordinates," *London Acad. Press*, 2009.

[88] P. M. Black and S. F. Ronner, "Cortical Mapping for Defining the Limits of Tumor Resection," *Neurosurgery*, vol. 20, no. 6, pp. 914–919, Jun. 1987.

[89] S. Boussen, L. Velly, C. Benar, P. Metellus, N. Bruder, and A. Trébuchon, "In Vivo Tumour Mapping Using Electrocorticography Alterations During Awake Brain Surgery: A Pilot Study," *Brain Topogr.*, vol. 29, no. 5, pp. 766–782, 2016.

[90] I. Osorio *et al.*, "Performance Reassessment of a Real-time Seizure-detection Algorithm on Long ECoG Series," *Epilepsia*, vol. 43, no. 12, pp. 1522–1535, Dec. 2002.

[91] E. C. Leuthardt, G. Schalk, J. R. Wolpaw, J. G. Ojemann, and D. W. Moran, "A brain–computer interface using electrocorticographic signals in humans," *J. Neural Eng.*, vol. 1, no. 2, pp. 63–71, 2004.

[92] G. Schalk *et al.*, "Two-dimensional movement control using electrocorticographic signals in humans," *J. Neural Eng.*, vol. 5, no. 1, pp. 75–84, 2008.

[93] F. H. Guenther *et al.*, "A Wireless Brain-Machine Interface for Real-Time Speech Synthesis," *PLoS One*, vol. 4, no. 12, p. e8218, Dec. 2009.

[94] J. P. Seymour, F. Wu, K. D. Wise, and E. Yoon, "State-of-the-art MEMS and microsystem tools for brain research," *Microsystems Nanoeng.*, vol. 3, no. 1, p. 16066, 2017.

[95] I. Rembado *et al.*, "Independent Component Decomposition of Human Somatosensory Evoked Potentials Recorded by Micro-Electrocorticography," *Int. J. Neural Syst.*, vol. 27, no. 04, p. 1650052, Aug. 2016.

[96] X. Wang *et al.*, "Mapping the fine structure of cortical activity with different micro-ECoG electrode array geometries," *J. Neural Eng.*, vol. 14, no. 5, p. 56004, 2017.

[97] N. Rogers *et al.*, "Correlation Structure in Micro-ECoG Recordings is Described by Spatially Coherent Components," *PLOS Comput. Biol.*, vol. 15, no. 2, p. e1006769, Feb. 2019.

[98] J. T. Maikos, R. A. I. Elias, and D. I. Shreiber, “Mechanical Properties of Dura Mater from the Rat Brain and Spinal Cord,” *J. Neurotrauma*, vol. 25, no. 1, pp. 38–51, Jan. 2008.

[99] A. Campbell and C. Wu, “Chronically Implanted Intracranial Electrodes: Tissue Reaction and Electrical Changes,” *Micromachines* , vol. 9, no. 9. 2018.

[100] S. Kassegne *et al.*, “Electrical impedance, electrochemistry, mechanical stiffness, and hardness tunability in glassy carbon MEMS µECoG electrodes,” *Microelectron. Eng.*, vol. 133, pp. 36–44, 2015.

[101] M. Vomero *et al.*, “A novel pattern transfer technique for mounting glassy carbon microelectrodes on polymeric flexible substrates,” *J. Micromechanics Microengineering*, vol. 26, no. 2, p. 25018, 2016.

[102] N. Goshi *et al.*, “Glassy carbon MEMS for novel origami-styled 3D integrated intracortical and epicortical neural probes,” *J. Micromechanics Microengineering*, vol. 28, no. 6, p. 65009, 2018.

[103] W. E. Van der Linden and J. W. Dieker, “Glassy carbon as electrode material in electro- analytical chemistry,” *Anal. Chim. Acta*, vol. 119, no. 1, pp. 1–24, 1980.

[104] S. Nimbalkar *et al.*, “Ultra-Capacitive Carbon Neural Probe Allows Simultaneous Long-Term Electrical Stimulations and High-Resolution Neurotransmitter Detection,” *Sci. Rep.*, vol. 8, no. 1, p. 6958, 2018.

[105] R. Natu, M. Islam, J. Gilmore, and R. Martinez-Duarte, “Shrinkage of SU-8 microstructures during carbonization,” *J. Anal. Appl. Pyrolysis*, vol. 131, pp. 17–27, 2018.

[106] M. E. Diamond, M. von Heimendahl, P. M. Knutsen, D. Kleinfeld, and E. Ahissar, “‘Where’ and ‘what’ in the whisker sensorimotor system,” *Nat. Rev. Neurosci.*, vol. 9, p. 601, Aug. 2008.

[107] C. C. H. Petersen, “The Functional Organization of the Barrel Cortex,” *Neuron*, vol. 56, no. 2, pp. 339–355, 2007.

[108] K. A. Ludwig, J. D. Uram, J. Yang, D. C. Martin, and D. R. Kipke, “Chronic neural recordings using silicon microelectrode arrays electrochemically deposited with a poly(3,4-ethylenedioxythiophene) (PEDOT) film,” *J. Neural Eng.*, vol. 3, no. 1, pp. 59–70, 2006.

[109] A. R. Harris, S. J. Morgan, J. Chen, R. M. I. Kapsa, G. G. Wallace, and A. G. Paolini, “Conducting polymer coated neural recording electrodes,” *J. Neural Eng.*, vol. 10, no. 1, p. 16004, 2012.

[110] S. Venkatraman *et al.*, “In Vitro and In Vivo Evaluation of PEDOT Microelectrodes for Neural Stimulation and Recording,” *IEEE Trans. Neural Syst. Rehabil. Eng.*, vol. 19, no. 3, pp. 307–316, 2011.

[111] P. A. Laplante, *Comprehensive Dictionary of Electrical Engineering*. Boca Raton, FL: Taylor & Francis, 2005.

[112] W. Y. Du, *Resistive, Capacitive, Inductive, and Magnetic Sensor Technologies*. Boca Ranton, FL: CRC Press, 2014.

[113] S. A. Nikles, D. S. Pellinen, J. Kitagawa, R. M. Bradley, D. R. Kipke, and K. Najafi, “Long term in vitro monitoring of polyimide microprobe electrical properties,” in *Proceedings of the 25th Annual International Conference of the IEEE Engineering in Medicine and Biology Society (IEEE Cat. No.03CH37439)*, 2003, vol. 4, pp. 3340-3343 Vol.4.

[114] B. Rubehn and T. Stieglitz, “In vitro evaluation of the long-term stability of polyimide as a material for neural implants,” *Biomaterials*, vol. 31, no. 13, pp. 3449–3458, 2010.

[115] C. C. Wood, D. D. Spencer, T. Allison, G. McCarthy, P. D. Williamson, and W. R. Goff, “Localization of human sensorimotor cortex during surgery by cortical surface recording of somatosensory evoked potentials,” *J. Neurosurg.*, vol. 68, no. 1, pp. 99–111, 1988.

[116] C. Cedzich, M. Taniguchi, S. Schäfer, and J. Schramm, “Somatosensory Evoked Potential Phase Reversal and Direct Motor Cortex Stimulation during Surgery in and around the Central Region,” *Neurosurgery*, vol. 38, no. 5, pp. 962–970, May 1996.

[117] A. Kuruvilla and R. Flink, “Intraoperative electrocorticography in epilepsy surgery: useful or not?,” *Seizure - Eur. J. Epilepsy*, vol. 12, no. 8, pp. 577–584, Dec. 2003.

[118] P.-S. Yao, S.-F. Zheng, F. Wang, D.-Z. Kang, and Y.-X. Lin, “Surgery guided with intraoperative electrocorticography in patients with low-grade glioma and refractory seizures,” *J. Neurosurg. JNS*, vol. 128, no. 3, pp. 840–845, 2017.

[119] N. Sanai and M. S. Berger, “Glioma extent of resection and its impact on patient outcome,” *Neurosurgery*, vol. 62, no. 4, pp. 753–766, Apr. 2008.

[120] A. De Benedictis, S. Moritz-Gasser, and H. Duffau, “Awake Mapping Optimizes the Extent of Resection for Low-Grade Gliomas in Eloquent Areas,” *Neurosurgery*, vol. 66, no. 6, pp. 1074–1084, Jun. 2010.

[121] P. T. Wang *et al.*, “Comparison of decoding resolution of standard and high-

density electrocorticogram electrodes," *J. Neural Eng.*, vol. 13, no. 2, p. 26016, 2016.

[122] L. Muller, L. S. Hamilton, E. Edwards, K. E. Bouchard, and E. F. Chang, "Spatial resolution dependence on spectral frequency in human speech cortex electrocorticography," *J. Neural Eng.*, vol. 13, no. 5, p. 56013, 2016.

[123] W. Penfield and T. Rasmussen, "Vocalization and arrest of speech," *Arch. Neurol. Psychiatry*, vol. 61, no. 1, pp. 21–27, 1949.

[124] E. F. Chang, J. D. Breshears, K. P. Raygor, D. Lau, A. M. Molinaro, and M. S. Berger, "Stereotactic probability and variability of speech arrest and anomia sites during stimulation mapping of the language dominant hemisphere," *J. Neurosurg.*, vol. 126, no. 1, pp. 114–121, 2017.

[125] E. Castagnola *et al.*, "Smaller, softer, lower-impedance electrodes for human neuroprosthesis: a pragmatic approach ," *Frontiers in Neuroengineering* , vol. 7. p. 8, 2014.

[126] E. Castagnola *et al.*, "Biologically Compatible Neural Interface To Safely Couple Nanocoated Electrodes to the Surface of the Brain," *ACS Nano*, vol. 7, no. 5, pp. 3887–3895, May 2013.

[127] C. Boehler, F. Oberueber, S. Schlabach, T. Stieglitz, and M. Asplund, "Long-Term Stable Adhesion for Conducting Polymers in Biomedical Applications: IrOx and Nanostructured Platinum Solve the Chronic Challenge," *ACS Appl. Mater. Interfaces*, vol. 9, no. 1, pp. 189–197, Jan. 2017.

[128] S. Carli, L. Casarin, G. Bergamini, S. Caramori, and C. A. Bignozzi, "Conductive PEDOT Covalently Bound to Transparent FTO Electrodes," *J. Phys. Chem. C*, vol. 118, no. 30, pp. 16782–16790, Jul. 2014.